1KW CONTACTLESS SLIP RING DESIGN USING SERIES-SERIES RESONANT CONVERTER TOPOLOGY

A THESIS SUBMITTED TO
THE GRADUATE SCHOOL OF NATURAL AND APPLIED SCIENCES
OF
MIDDLE EAST TECHNICAL UNIVERSITY

BY

HAKAN POLAT

IN PARTIAL FULFILLMENT OF THE REQUIREMENTS
FOR
THE DEGREE OF MASTER OF SCIENCE
IN
ELECTRICAL AND ELECTRONICS ENGINEERING

JUNE 2021

Approval of the thesis:

1KW CONTACTLESS SLIP RING DESIGN USING SERIES-SERIES RESONANT CONVERTER TOPOLOGY

submitted by **HAKAN POLAT** in partial fulfillment of the requirements for the degree of **Master of Science in Electrical and Electronics Engineering Department, Middle East Technical University** by,

Prof. Dr. Halil Kalıpçılar
Dean, Graduate School of **Natural and Applied Sciences** _____

Prof. Dr. İlkay Ulusoy
Head of Department, **Electrical and Electronics Engineering** _____

Assoc. Prof. Dr. Ozan Keysan
Supervisor, **Electrical and Electronics Engineering** _____

Examining Committee Members:

Assist. Prof. Dr. Emine Bostancı
Electrical and Electronics Engineering, METU _____

Assoc. Prof. Dr. Ozan Keysan
Electrical and Electronics Engineering, METU _____

Prof. Dr. Işık Çadırcı
Electrical and Electronics Engineering, Hacettepe University _____

Prof. Dr. Muammer Ermiş
Electrical and Electronics Engineering, METU _____

Prof. Dr. Timur Aydemir
Electrical and Electronic Engineering, Kadir Has University _____

Date: 24.06.2021

I hereby declare that all information in this document has been obtained and presented in accordance with academic rules and ethical conduct. I also declare that, as required by these rules and conduct, I have fully cited and referenced all material and results that are not original to this work.

Name, Surname: Hakan Polat

Signature :

ABSTRACT

1KW CONTACTLESS SLIP RING DESIGN USING SERIES-SERIES RESONANT CONVERTER TOPOLOGY

Polat, Hakan
M.S., Department of Electrical and Electronics Engineering
Supervisor: Assoc. Prof. Dr. Ozan Keysan

June 2021, 134 pages

Slip rings are often used in wound rotor synchronous machines to supply required field excitation during rotation. They mainly consist of carbon brushes and copper rings where the power transmission is achieved by constant friction, which results in mechanical wear over time. To eliminate the contact, brushless exciters are used. However, their low-speed operation is problematic. Therefore, in this thesis, the aim is to design a contactless slip-ring with improved fault tolerance to supply the required field current without physical contact and with a wide speed range limited solely by mechanical limitations. To achieve high reliability, modular design is employed. The power transfer is achieved by two transmitters and four receivers whose outputs are connected in parallel to form a common DC-bus. The system is series-series compensated. The problem of current/power-sharing is solved first analytically with the introduction of cross-coupling and intentional detuning. Then a 1 kW system is designed to experimentally verify the proposed methods. While an increased power-sharing is observed, to further increase the fault tolerance, a middle-stage resonator is added, and an experimental setup is built. Finally, the presented system is mounted

on a rotating shaft, and improved fault tolerance compared to conventional single transmitter single receiver inductive power transfer systems is achieved.

Keywords: Wireless power transfer, Inductive power transfer, Series-series compensation, Resonator system, Modularity, Fault tolerance, Reliability

ÖZ

SERİ-SERİ REZONANT ÇEVİRİCİ İLE 1KW KABLOSUZ BİLEZİK TASARIMI

Polat, Hakan
Yüksek Lisans, Elektrik ve Elektronik Mühendisliği Bölümü
Tez Yöneticisi: Doç. Dr. Ozan Keysan

Haziran 2021 , 134 sayfa

Bilezik sistemleri sargı rotorlu senkron makinelerde dönüş sırasında gerekli rotor uyartısını sağlamakta kullanılır. En temel olarak karbon fırçalara ve bakır bilezik şeklinde halkalara sahiptir. Dönüş sırasında güç aktarımı fırçaların bileziklere sürekli olarak sürtmesi ile sağlanmasına rağmen karbon fırçalar zamanla sürtümeye bağlı olarak zarar görmektedir. Bu durumu engellemek için rotor kısmına ufak bir sabit mıknatıslı motor koyulabilir ancak bu motorlar düşük hızlarda problem ortaya çıkartmaktadır. Bu tezde, hata toleransı yüksek bir kablosuz kontak halkası tasarlanması amaçlanmaktadır. Tasarlanan systemin sargı rotorlu senkron makinelerede kullanılması, fiziksel kontağın elenmesi ve yalnızca mekanik limitlere takılan geniş bir çalışma hız aralığı olması amaçlanmaktadır. Sistem güvenilirliğini arttırmak için modüler yapı kullanılmıştır. Güç aktarımı iki verici ve dört alıcı ile sağlanmaktadır. Alıcı modüllerin çıkışları paralel bağlanmış ve ortak DC bara elde edilmiştir. Sistemde seri-seri kompenzasyon topolojisi kullanılmıştır. Sistem tasarımı sırasında ortaya çıkan akım dağılımı problemi ilk olarak analitik olarak çözülmüş ve alıcılar arasına ortak induktans ve alıcı rezonans frekansını değiştirme metotları ortaya çıkarılmıştır. 1 kW bir

prototip sistem ile bu etkiler deneysel olarak doğrulanmıştır. İlk sistemde akım dağılımı iyileşmesine rağmen, hata toleransını arttırmak için orta kısıma ek bir rezonatör koyulmuştur. Yeni sistemi test etmek için yeni bir prototip kurulmuş ve bu sistem döner şafta takılmıştır. Sistem testleri sonunda hata toleransının arttırıldığı gözlenmiştir.

Anahtar Kelimeler: Kablosuz güç aktarımı, İndüktif güç aktarımı, Seri-seri kompensazyon, Resonatör sistemi, Modülerlik, Hata toleransı, Güvenilirlik

To my lovely family...

ACKNOWLEDGMENTS

Throughout my MSc. I had great support and assistance from many people.

Firstly, I would like to show my sincere thanks to Dr. Ozan Keysan for his outstanding support not only for his technical assistance but also his guidance on being an excellent engineer and team member. If it were not for his motivation, support and guidance, this thesis would be impossible.

Secondly, I would like to thank everyone on METU PowerLab, for their support and help. Everyone, helps each other and accomplishes great research outcomes with hardwork and dedication. Getting personal support from others knowing they have lots of other things to do, shows great friendship bonds and collaboration which I am sure will last a lifetime. I would also like to thank my project partner Enes Ayaz for his effort during this thesis. Citing him at every chapter of this thesis wouldn't be wrong. Moreover, I would like to thank my other co-worker Ogün Altun for his endless support and hard work. I also wish to show my greatest gratitude to my co-authors Nail Tosun and Doğa Ceylan whom I worked previously on a different project.

I am thankful to TÜBİTAK, the Scientific and Technological Research Council of Turkey, for granting me their M.S. studies scholarship, BİDEB 2210. Also, I am grateful to TÜBİTAK for funding me as a researcher student for a year in the project, 1 kW Contactless Slip Ring Design Using Series-Series Resonant Converter Topology, 119E217.

I would like to thank my long friend and roommate Reha Erkan who supported me throughout my MSc. Being able to get my mind off work was often just as important

as concentrating on work where I believe he deserves a PhD.

Finally and most importantly, I would like to thank my family who where always there for me at every part of my life. Without them no thesis is worth finishing.

TABLE OF CONTENTS

ABSTRACT v

ÖZ vii

ACKNOWLEDGMENTS x

TABLE OF CONTENTS xii

LIST OF TABLES xvii

LIST OF FIGURES xix

LIST OF ABBREVIATIONS xxv

LIST OF VARIABLES xxvii

CHAPTERS

1 INTRODUCTION 1

1.1 Electrical Machines 1

1.2 Conventional Field Exciters 2

1.3 Review of Inductive Power Transfer Systems 3

1.4 Research Goals and Objectives 5

2 PRINCIPLES OF IPT SYSTEMS AND INITIAL SYSTEM CONSIDERATIONS 7

2.1 Operation Principles and Topologies of Common Inductive Power Transfer Systems 7

2.1.1 Common Inductive Power Transfer Topologies 8

2.1.1.1 Receiver Side Compensation 9
2.1.2 Zero Voltage Switching in IPT Systems 12
2.1.2.1 Leading Power Factor 13
2.1.2.2 Lagging Power Factor 13
2.1.3 Bifurcation Phenomenon in Doubly Tuned IPT Systems 14
2.1.4 Modular IPT Systems 15
2.2 Initial System Considerations 16
2.2.1 IPT Coil Shape Consideration 19
2.2.2 Module Number Selection 21
3 ANALYTICAL DERIVATIONS FOR BIFURCATION FREE DESIGN AND CURRENT BALANCING METHODS 23
3.1 Bifurcation Free Design 24
3.1.1 Current Balancing Issues in Rx Modules 29
3.1.2 Rectifier Effect and Load Sharing 29
3.2 Current Balancing Methods 31
3.2.1 Effect Of Receiver Cross-Coupling 32
3.2.2 Intentional De-tuning of the Receiver Side Resonant Tank . . 38
3.3 Summary 42
4 IPT COIL AND PCB DESIGN 45
4.1 IPT Coil Design 45
4.1.1 Tx Side IPT Coil Design 46
4.1.2 Rx Side IPT Coil Design 48
4.1.3 Reduction of Ferrite Core Requirement 49

4.1.4 IPT Coil System FEA Results and Setup 51
4.2 Tx Side Full Bridge Converter Design 54
4.2.1 Half Bridge Design 54
4.2.1.1 Gate-Drive Method and Layout Considerations 54
4.2.1.2 Thermal Management 56
4.2.2 Over Voltage Protection (OVP) 59
4.2.3 Reverse Voltage Polarity Protection 60
4.3 Rx Side Full Bridge Diode Rectifier Design 62
4.3.1 Thermal Management 62
4.4 Summary 63
5 2TX-4RX IPT SYSTEM SIMULATION AND EXPERIMENTAL RESULTS 67
5.1 Experimental Results and Discussion for the Proposed Current Balancing Methods 67
5.1.1 Fully-Aligned Case 69
5.1.2 Misaligned Case 69
5.2 Discussion 70
5.3 2Tx-4Rx Rotational System Experimental Results and Discussion . . 73
5.3.1 Operation Under Fault 75
5.4 Summary 76
6 DESIGN AND TESTING OF 2TX-4RX SYSTEM WITH MIDDLE STAGE RESONATOR 81
6.1 Design Methodology 83
6.2 IPT Coil Design Considerations 86
6.3 Experimental Results 89

6.3.1 Normal Operation 91
6.3.2 Single and Double Rx Open Circuit Fault 93
6.3.3 Single Tx Open Circuit Fault 95
6.3.4 Open and Short Circuited Load Fault 96
6.4 Discussion 98
6.4.1 Effect of Modularity on Fault Tolerance 99
6.4.2 Modes of Operation 99
6.4.3 Third Harmonic Component 102
6.5 Three Coil Rotational System 102
6.5.1 Experimental Results 104
6.5.2 250 RPM Rotational Fault Tests 106
6.5.2.1 Single Rx Open Circuit Fault 106
6.5.2.2 Double Rx Open Circuit Fault 107
6.5.2.3 Short Circuited Fault 108
6.5.2.4 Open Circuited Load Fault 109
6.5.2.5 Single Tx Open Circuit Fault 109
6.6 Discussion 110
6.7 Summary 112
7 CONCLUSIONS 115
7.1 2Tx-4Rx IPT System 115
7.2 2Tx-4Rx IPT System With Middle Stage Resonator 116
7.3 Comparison 117
7.4 Summary of Contribution to Literature and Novelties 118

7.5 Practical Application Considerations 119
7.5.1 Field Current Filtering 120
7.6 Possible Improvements 121
7.6.1 Analytical Modeling 121
7.6.2 Power Electronics Converter Improvements 122
7.6.3 IPT Coil Intrinsic Quality Factor Improvements 123
7.6.4 Mechanical Improvements 123
7.6.5 Closed-Loop Control Improvements 123
7.6.6 Reliability 124
7.6.7 Different Topologies 124
7.6.8 System Sizing 124
REFERENCES 127

LIST OF TABLES

TABLES

Table 1.1 Dynamic IPT Systems in the Industry and Literature. [15] 5

Table 1.2 Initial System Parameters 6

Table 2.1 Input side impedance of conventional IPT topologies 11

Table 2.2 Key Features of Different Conventional IPT Topologies 11

Table 3.1 Cross-coupled analytical input parameters and results 37

Table 3.2 Finalized System Parameters for 2Tx-4Rx System 43

Table 4.1 Self and Mutual Inductances of the Proposed System 46

Table 4.2 Comparison of Inductance Values Obtained from Experimental Results and FEA Simulations 53

Table 4.3 Finalized System Parameters for 2Tx-4Rx System 55

Table 4.4 Finalized IPT Coil System Geometric Parameters 65

Table 5.1 Experimental Setup Parameters 69

Table 5.2 Current Sharing for Missaligned Different Balancing Methods and Improvements 72

Table 6.1 System Parameters 85

Table 6.2 Final System Parameters 88

Table 6.3 Parameters of the High Frequency Coupled Inductors 90

Table 6.4 Experimental Setup Parameters 92

Table 6.5 Efficiencies of the System Under Different Fault Conditions 99

Table 7.1 Comparison of the Proposed IPT Systems 118

Table 7.2 Contributions to Literature and Novelties 119

Table 7.3 Wound Rotor Synchronous Machine Parameters [6] 120

LIST OF FIGURES

FIGURES

Figure 1.1 Conventional slip ring and brush failure. 2

Figure 1.2 Tesla historic IPT. 4

Figure 1.3 IPT coils MIT,2007. 4

Figure 2.1 Conventional IPT topology.[20] 7

Figure 2.2 Conventional IPT topologies. 9

Figure 2.3 Series and parallel connected Rx side. 10

Figure 2.4 Half-bridge converter with parasitic C_{ds} capacitance and load. . . 12

Figure 2.5 Leading power factor. The ZVS condition is not achieved. 13

Figure 2.6 Lagging power factor. The ZVS condition is achieved. 14

Figure 2.7 Phase angle between V_{in} and I_{Tx} for different magnetic couplings. 15

Figure 2.8 Phase angle between V_{in} and I_{Tx} for different loadings. 15

Figure 2.9 Illustration of the proposed system. 17

Figure 2.10 1Tx-2Rx circuit representation and realistic rotational system. . . 18

Figure 2.11 Different IPT coil shapes employed in the literature. 19

Figure 2.12 Variation of induced current on the shaft for different coil geometries. 20

Figure 2.13 1Tx-1Rx system with induced voltage components. 21

Figure 3.1 Single and double Rx module magnetic circuit illustration. . . . 24

Figure 3.2 2Tx-4Rx system FHA circuit schematic. 27

Figure 3.3 The change in the receiver currents for equal and different magnetic coupling. 30

Figure 3.4 Rx side induced voltages for equal and unequal magnetic couplings. 31

Figure 3.5 Parallel Rx modules with and without cross-coupling.(Grayports show the cross-coupling components). 32

Figure 3.6 Parallel connected Rx's with common DC bus. 33

Figure 3.7 Phasor diagram for common DC bus parallel connected Rx modules with cross-coupling. The circuit components was given in Fig. 3.6. 34

Figure 3.8 Effect of cross-coupling on the Rx side current sharing. 35

Figure 3.9 Effect of cross-coupling on the current sharing for misaligned case. 38

Figure 3.10 Effect of detuning on the current sharing. 39

Figure 3.11 First harmonic approximation of single transmitter single receiver IPT system. 40

Figure 4.1 Un-bent end-winding Tx side IPT coil geometry and airgap B-field density. 47

Figure 4.2 Bent end-winding Tx side IPT coil geometry and airgap B-field density. 48

Figure 4.3 Tx-Rx couplings of non-bended and bended endwinding for a complete rotation. 49

Figure 4.4 Overall Rx side IPT coil systems. (Ferrite back-cores are omitted for visual clarity.) 50

Figure 4.5 Tx coil with complete ferrite back-core and ferrite spokes. 50

Figure 4.6 Overall IPT coil systems. (Ferrite back-cores are omitted for visual clarity.) 51

Figure 4.7 Tx and Rx coil couplings for a complete rotation. 52

Figure 4.8 Manufacured Tx and Rx side IPT coils.(Rx side ferrites are omitted for visual clarity.) 53

Figure 4.9 Boostrap gate drive method with negative gate turn-off capability. 55

Figure 4.10 Gate turn-on/off loops for a single MOSFET.(red: turn-on, yellow:turn-off) 56

Figure 4.11 Thermal model of the full bridge converter. 58

Figure 4.12 Heatsink and fan connection to the PCB. 59

Figure 4.13 Over-voltage protection circuit. 60

Figure 4.14 Over-voltage protection simulation. 61

Figure 4.15 Reverse voltage polarity circuit. 61

Figure 4.16 Rx side heatsink, thermal-vias and common DC-bus connector. . 63

Figure 4.17 Rx side rectifier diodes and resonant capacitor PCB cards. 64

Figure 5.1 Test setup illustration. 68

Figure 5.2 Rx current waveforms for fully-aligned case and different current balancing methods. 70

Figure 5.3 Effects of cross-coupling and detuning on the Rx side current distribution for the missaligned case. 71

Figure 5.4 $\frac{V_{out}}{V_{in}}$ gain plots for different current balancing methods. 73

Figure 5.5 Tx side current for a complete rotation. 74

Figure 5.6 Comparison of simulated and experimental gain plots of the test setup. The gain plot is taken for normal operation without any faulty condition. Since uniform radial B-field is achieved usign the proposed coil geometry, the gain plot is constant for different Tx-Rx positions. . . 75

Figure 5.7 Rx module current waveforms for a full rotation. 76

Figure 5.8 Efficiency for different power inputs. The experiment was performed for normal operation without faulty condition. 77

Figure 5.9 Thermal images of Tx and Rx PCB's for rated power output. The maximum temperature at the Tx is $61.1°C$ and $51.1°C$ at the receiver. 78

Figure 5.10 Tx current envelope for a complete rotation. The Rx-4 module is open-circuited to investigate faulty mode of operation. 78

Figure 5.11 Rx current envelope for a complete rotation. The Rx-4 module is open-circuited to investigate faulty mode of operation. 79

Figure 6.1 The proposed 2Tx-4Rx system with resonator circuit. 82

Figure 6.2 Reflected impedance from Rx side to resonator side. 83

Figure 6.3 Flowchart of the proposed design. 87

Figure 6.4 Comparison of analytical and simulated critical coupling for different design parameters. 89

Figure 6.5 Resonator IPT coil geometry and FEA solution. The color table indicates the B-field magnitude on the circular surface in $\frac{Wb}{m^2}(T)$. . . . 90

Figure 6.6 Experimental setup for the proposed IPT system. 91

Figure 6.7 Input voltage, Tx side currents, resonator current and Rx currents for no-fault operation. ($I_{Tx1,2} \approx 6.5\ A_{rms}, I_R = 5.4\ A_{rms}$) 93

Figure 6.8 Input voltage, Tx side currents, resonator current and Rx currents for single open circuited Rx fault. 94

Figure 6.9 Input voltage, Tx side currents, resonator current and Rx currents for , double open circuited Rx fault. 94

Figure 6.10 Input voltage, Tx side current, resonator current and Rx currents for single open circuited Tx fault. 95

Figure 6.11 Open and short circuit fault conditions. V_{in}, I_{Tx}, I_R and I_{Rx} are shown for each type of fault. $f_{operation} = 165\ kHz$ 96

Figure 6.12 Open and short circuit fault condition simulation in frequency domain. I_{Tx}, I_R and I_{Rx} are shown for each type of fault. 98

Figure 6.13 Theoretical maximum power transfer for normal and single Tx side open circuit fault condition. Over-design rating of each Tx module to transfer the rated power under fault condition is also given. 100

Figure 6.14 Voltage and current gain plot for the experimental setup under different loading conditions. The CV and CC operation points are also presented. 101

Figure 6.15 IPT system with middle stage resonator mounted on a rotating shaft. (The Tx side IPT coil is placed with an angle for visual clarity.) . 103

Figure 6.16 Tx and resonator IPT coils in epoxy resin for the rotational system. Instead of using a complete back-core, ferrite sticks are placed. . . 104

Figure 6.17 The measured AC Tx module current envelope at 150 rpm. . . . 105

Figure 6.18 The measured input DC current at 150 rpm. 105

Figure 6.19 The measured output voltage at 150 rpm. 106

Figure 6.20 Single Rx coil open circuit fault for 250 rpm rotational speed. . . 107

Figure 6.21 Double Rx coil open circuit fault for 250 rpm rotational speed. . 108

Figure 6.22 Short circuited load fault for 250 rpm rotational speed. 109

Figure 6.23 Open circuited load fault for 250 rpm rotational speed. 110

Figure 6.24 Short circuited load fault for 250 rpm rotational speed. 111

Figure 6.25 Experimental gain plots of double and single Tx operation for $M_{Tx1,Tx2} = -10\mu H$. The ZVS region is given for normal operation(i.e. double Tx operation.) 112

Figure 7.1 2Tx-4Rx system with middle stage resonator connected to field winding of an wound rotor synchronous generator presented in [6]. . . . 121

LIST OF ABBREVIATIONS

AC	Alternating current
AWG	American wire gauge
CBR	Current balancing ratio
DIPT	Dynamic inductive power transfer
EMF	Electromotive force
EMI	Electromagnetic interference
EV	Electric vehicle
FE	Finite element
FEA	Finite element analysis
FEM	Finite element method
FHA	First harmonic approximation
GND	Ground
HFCI	High frequency coupled inductor
IPT	Inductive power transfer
MOSFET	Metal oxide semiconductor field effect transistor
NMOS	N type MOSFET
OVP	Over voltage protection
PCB	Printed circuit board
PGND	Power ground
PM	Permanent magnet
PP	Parallel-parallel
PS	Parallel-series
RVP	Reverse voltage polarity
Rx	Receiver

SP	Series-parallel
SS	Series-series
Tx	Transmitter
WPT	Wireless power transfer
ZVS	Zero voltage switching

LIST OF VARIABLES

α	2nd Rx current phase
β	1st Rx current phase
δ	Angle between Rx currents
δ	Skin depth
μ	Permability
ω	Operating angular frequency
ω_0	Resonant angular frequency
ω_{Rx}	Resonant angular frequency of Rx side resonant tank
ω_{Tx}	Resonant angular frequency of Tx side resonant tank
ρ	Resistivity
θ	Tx current phase
A_L	Inductance factor of a magnetic core
C_{ds}	Parasitic drain to source capacitance of MOSFET
C_{gs}	Parasitic gate to source capacitance of MOSFET
C_R	Resonator side resonant capacitor
C_{Rx}	Rx side resonant capacitor
C_{Tx}	Tx side resonant capacitor
D_{in}	Inner diameter of an IPT coil
D_{out}	Outer diameter of an IPT coil
f_0	Resonant frequency
I_{ds}	Drain to source current of the MOSFET
$I_{Rx,n}$	n^{th} Rx side AC input current
I_{Tx}	Tx side AC input current

J	Current density
k	Magnetic coupling
k_c	critical magnetic coupling
L_R	Resonator inductance
$L_{Rx,n}$	n^{th} Rx inductance
$L_{Tx,n}$	n^{th} Tx inductance
M	Mutual inductance
M_1	Mutual inductance between Tx and the first Rx
M_2	Mutual inductance between Tx and the second Rx
M_s	Mutual inductance between Rx coils
$P_{conduction}$	Conduction loss of semiconductor
$P_{switching}$	Switching loss of semiconductor
$P_{turn-off}$	Turn off switching loss of semiconductor
Q_{Rx}	Rx side quality factor
$R_{ds,on}$	Drain to source on resistance
$R_{equ,n}$	Reflected load resistance seen by the nth Rx
$R_{heatsink}$	Thermal resistance of the heatsink
R_{j-c}	Junction to case thermal resistance
R_R	Intrinsic resistance of resonator IPT coil
R_{Rx}	Intrinsic resistance of Rx IPT coil
R_{Tx}	Intrinsic resistance of Tx IPT coil
R_L	Load resistance
t_{fall}	Fall time of the MOSFET
$t_{off,delay}$	Turn-off delay time of the MOSFET
t_{rise}	Rise time of the MOSFET
V_c	Voltage across capacitor
V_{ds}	Drain to source voltage of MOSFET

V_{gs}	Gate to source voltage of MOSFET
$V_{in,DC}$	DC input voltage
V_{in}	Fundamental component of square input voltage
$V_{out,DC}$	DC output voltage
V_{out}	Voltage seen across reflected load resistance
$V_{Rx,n}$	Induced voltage on the nth Rx coil
V_z	Zener voltage of zener diode
Z_r	Reflected impedance seen across the Tx side inductor
Z_{Tx}	Reflected impedance seen across the Tx side

CHAPTER 1

INTRODUCTION

1.1 Electrical Machines

According to [1], nearly 60% of all electricity is consumed by electrical machines. With the introduction of wind energy and electric cars, the interest in reliable, cheaper, and more efficient machine design has significantly increased both in the industry and literature. While the fundamental idea behind all AC electrical machines can be traced back to the law of electromagnetic induction, it can be divided into two groups which are synchronous(SM), and asynchronous machines [2]. Generation of field MMF is required for all-electric machines. While no external field current excitation is required for permanent magnet (PM) machines or squirrel cage induction machines, wound rotor synchronous machines or induction machines require field current that are fed by an external slip-ring or brushless exciters.

With the development in permanent magnet materials, a higher field flux density can be achieved, which results in higher efficiency, increased power density, high operation speed range, ext. Moreover, permanent field excitation eliminates the need to use slip-rings or brushless exciters for external field excitation. However, due to the high demand for the rare earth material used in PM [3], the cost of PMSM machines is concerning, especially in the electric vehicle industry and wind turbines. Therefore, there is an increasing trend for using copper windings to the generate field MMF of the machine.

1.2 Conventional Field Exciters

In many electrical machines, field excitation is necessary. In conventional wound rotor synchronous motors, these are achieved using slip rings. Slip rings are attached directly to the shaft, and it consists of conductive rings and brushes. While the rings rotate with the shaft, the carbon brushes contacts these rings, and current may flow in either direction depending on the application. A conventional slip ring is given in Fig. 1.1-a.



(a) Slip ring.



(b) Slip ring brush failure[4].

Figure 1.1: Conventional slip ring and brush failure.

During the whole operation, constant friction on the constant surface of the brushes wears the system down in time, as given in Fig. 1.1-b. Therefore, a major disadvantage of such a mechanical system is the requirement of regular maintenance. While it may be possible, in wind power applications like off-shore wind turbines, regular maintenance is costly and time consuming. Moreover, failure of the slip rings often results in complete system stop, which is undesired.

Another possible solution to field excitation is the brushless exciter. For large synchronous machines, control of field current is achieved by connecting a smaller generator on the same shaft where the generated electrical power on the rotor side is rectified and applied to the field of the larger machine [5]. Brushless exciters are

often PM machines where the rotating magnetic field is achieved using permanent magnets. Since the power is generated with magnetic induction, galvanic isolation is present. However, a major disadvantage of these systems is the lack of control at low rotational speed operation or while the rotor is stationary. This is especially problematic for variable speed machines. When the rotational speed is slow, the induced emf magnitude decreases and required field current excitation may not be achieved.

The field excitation techniques used are limited either by constant friction or lack of low-speed operation. To solve both of these problems, in this thesis, an inductive power transfer(IPT) system is proposed for wound rotor synchronous machines [6, 7, 8, 9]. While the system can operate without any physical contact, hence solving the wear down, it can also transfer power regardless of rotational speed since the switching frequencies of IPT systems are much larger than rotational speed. The maximum operating speed of such a system is limited solely by the limit of the mechanical structure.

1.3 Review of Inductive Power Transfer Systems

Inductive power transfer (IPT) is not a new subject where many realization experiments were performed as early as late 1800s. The very first IPT system was built by Prof. Heinrich Hertz, in which free space propagation of electromagnetic waves is shown. A high frequency signal was generated using a spark gap power supply, and the signal was received on the other coil. Later, Nicola Tesla, inspired by Hertz's work, built a large coil and a very large tower in his laboratory in Colorado Springs, US [10]. Similarly, since the semiconductors were not invented at his time, a 150 kHz AC current was generated using a spark gap. The system structure used in the experiment is given in Fig. 1.2. Although there has been a significant improvement in electronics and technology since then, the working principles and methods presented by Tesla are still the foundation of nearly all IPT systems. In Fig. 1.2, there exists a spark-gap where the AC current is generated. This AC current is filtered by a series connected LC filter where the inductance is also used to generate a magnetic field. The generated magnetic field is then coupled to the receiver obeying Faraday's law of

electromagnetic induction.

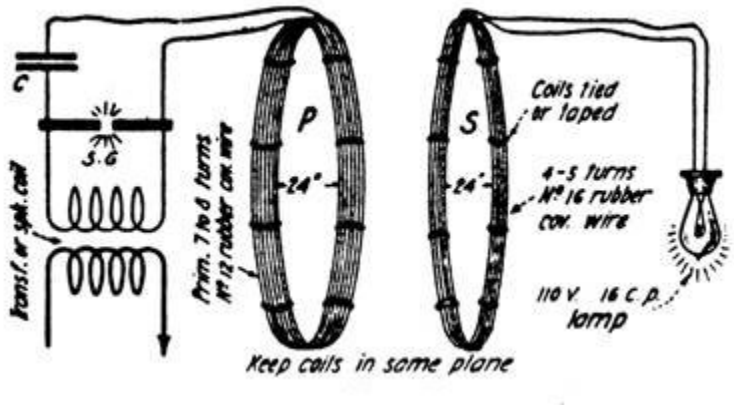


Figure 1.2: Tesla historic IPT.

With the increase in computational power and semiconductor technology, IPT systems again gained popularity. Perhaps the achievement that attracted the researchers is the transfer of power with an air gap of 2 m, using resonator coils with 30 cm radius (MIT,2007) given in Fig 1.3. [11]



Figure 1.3: IPT coils MIT,2007.

IPT systems are also commercialized in areas such as biomedical device charging, consumer electronics, static and dynamic EV charging. In 2009 KAIST (Korea's Advanced Institute for Science and Technology) built a 3 kW ONLINE EV charger, which is capable of transferring power at 10 mm airgap with an 82% efficiency [12].

In 2011, Samsung announced the first commercially available IPT phone charger [13], while in the same year, Nissan also demonstrated its stationary EV IPT charger [14]. Moreover, some have tried and accomplished to transfer power whilst the EV is moving on the road, which are called dynamic IPT systems. In Table 1.1, a few DIPT systems are presented.

Table 1.1: Dynamic IPT Systems in the Industry and Literature. [15]

Parameters	Application	Airgap	Efficiency	Power Level	Misalignment	Frequency
KAIST	Car(2009)	10mm	88%	3kW	3mm	20kHz
	Bus(2009)	170mm	72%	6kW	230mm	20kHz
	Train(2010)	120mm	74%	15kW	-	60kHz
	Bus(2016)	200mm	80%	27kW	240mm	-
ORNL[16, 17]	Car(2016)	162mm	93%	20kW	150mm	22kHz
Bombardier	Trams(2010)	60mm	90%	200kW	very low	20kHz
Conductix-Wamplet AG	Bus(2002)	40mm	90%	120kW	-	15-20kHz
WAVE [18]	Bus(2011)	150-254mm	90%	50kW	245mm	20kHz
Utah State University[19]	Bus(2016)	-	86%	25kW	150mm	20kHz

1.4 Research Goals and Objectives

The aim of this thesis, is to design a 1 kW contactless slip ring with improved reliability. The proposed system aims to replace the slip rings in large variable speed field excited synchronous generators. Moreover, with power downscaling, this same system structure can also be used in rotary parts in robotics. Modular structure is employed to increase the fault tolerance of the system. The initial system parameters are presented in Table 1.2.

In parallel connected common DC-bus, series-series compensated IPT systems, the Rx side current/power-sharing is challenging. This unbalance results from unequal magnetic coupling between the Tx and Rx IPT coil pair. Unbalance problems may result in extreme stress on a single Rx module that will decrease the lifetime of the module. Therefore, in this thesis, special attention will be given to current balancing methods. In Chapter 3, the proposed 2Tx-4Rx IPT system will be designed analyti-

Table 1.2: Initial System Parameters

Power Rating	1000 W
Input Voltage (V_{in})	100 V_{DC}
Output Voltage (V_{out})	100 V_{DC}
Resonant Frequency	150 kHz

cally where a bifurcation-free design methodology will be presented. Then, two novel current balancing methods, cross-coupling and intentional Rx side resonant frequency detuning will be presented in an analytical manner. The required cross-coupling and detuned frequency will be determined for a given current balancing ratio between the Rx modules. After all system parameters are determined, the practical system design will be explained in Chapter 4. First, the key features in the PCB design will be presented. Then, the IPT coil design will be shared. Since the aim is to test the presented current-balancing methods no special attention was given to the IPT coil design. Finally, in Chapter 5, both the current balancing methods and the overall system will be experimentally verified.

The next required feature is to increase the fault tolerance and reliability of the proposed system. Since the system aims to replace slip rings where regular maintenance is problematic and costly, fault tolerance and reliable operation of the system is a key feature. Although current balancing is achieved for the 2Tx-4Rx system under normal operation, unbalance is observed during fault. To solve the problem, 2Tx-4Rx system with a middle stage resonator is introduced in Chapter 6. First, a conventional series-series IPT system design is improved such that it became applicable to systems with middle stage resonator. The system is later tested for different fault conditions.

CHAPTER 2

PRINCIPLES OF IPT SYSTEMS AND INITIAL SYSTEM CONSIDERATIONS

2.1 Operation Principles and Topologies of Common Inductive Power Transfer Systems

As the name also implies, IPT systems use magnetic induction to transfer power. Regardless of frequency and power, the basic operation principles of conventional power transformers, inductors, and IPT coils are the same. The electrical power is converted to magnetic energy, and this magnetic power is later converted back to electrical energy. In Fig. 2.1 two magnetically coupled coils are presented.

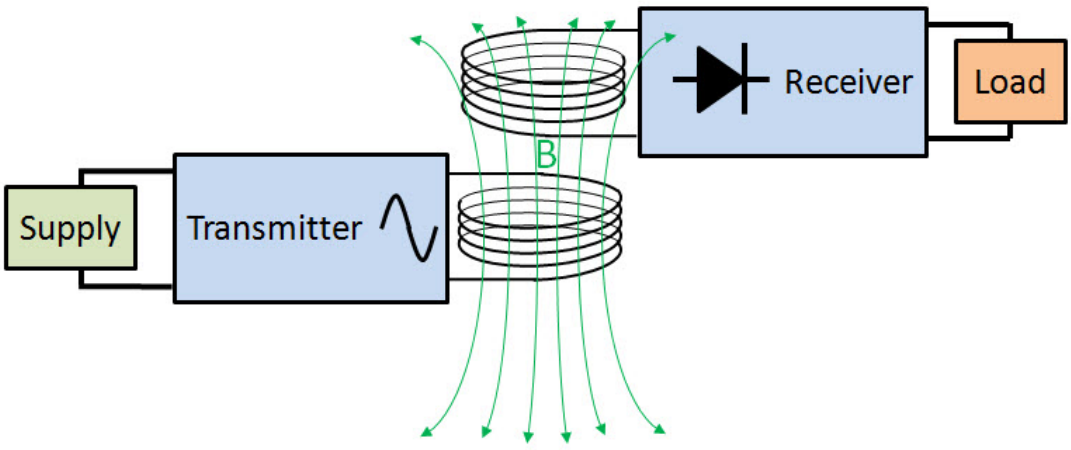


Figure 2.1: Conventional IPT topology.[20]

The alternating current passing through the first coil generates a magnetic field obeying Ampere's law given in (2.1).

$$\oint_C B d\ell = \mu_0 I_C \tag{2.1}$$

The magnetic field passing through the other coil generates an induced voltage obeying Faraday's law of induction in (2.2).

$$\varepsilon = -N\frac{\Delta\Phi}{\Delta t} \tag{2.2}$$

For conventional transformers, the equation in (2.2) is used where Φ is the flux generated by the primary windings. However, this approximation is only valid when the coupling "k" between the coils is high.

Assuming the system is linear (saturation is neglected), the equation in (2.2), can further modified as in (2.3).

$$\varepsilon = -N\frac{kd\Phi_{Tx}}{dt} \tag{2.3}$$

And finally, a fundamental equation which will later be used can be written as in (2.4).

$$\varepsilon = \frac{d(MI_{Tx})}{dt} = j\omega M I_{Tx} \tag{2.4}$$

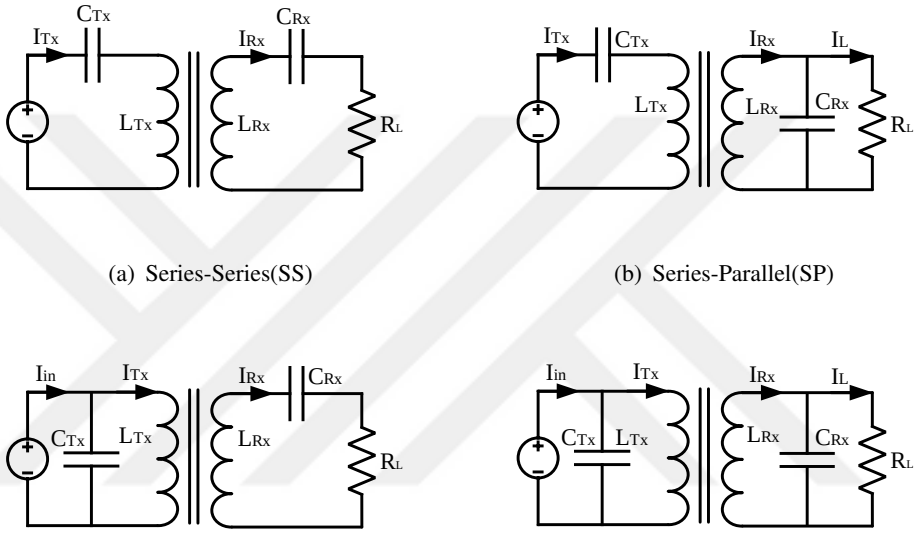
The equation in (2.4) shows that the induced voltage on the secondary coil is proportional to operation frequency ω, mutual inductance M, and primary side current magnitude I_{Tx}.

These formulations are valid for all power converters with galvanic isolation. However, a major difference between the IPT systems and a power converter is the power factor. Since the coupling in IPT systems are much lower due to high leakage inductance, a highly inductive reactive power will be drawn. Therefore, the IPT topologies often employ capacitors to bring the power factor close to unity.

2.1.1 Common Inductive Power Transfer Topologies

The main idea behind all IPT topologies is to bring the power factor to unity under certain conditions. Since the current is highly inductive, the compensation is often

done by connecting capacitors to both sides. The capacitor can either be connected in series or parallel to the IPT inductor. Series-series(SS), series-parallel(SP) [21], parallel-parallel(PP) [22] and parallel-series(PS) are the main IPT topologies. The first letter indicates the connection type of the capacitor on the Tx side. Similarly, the second letter indicates the connection type to the Rx side. Although there are higher-order compensations like LCC-LCC [23], LCL-LCL [24], they are somewhat a combination of the fundamental topologies. The circuit presentations are presented in Fig. 2.2



(a) Series-Series(SS)

(b) Series-Parallel(SP)

(c) Parallel-Series(PS)

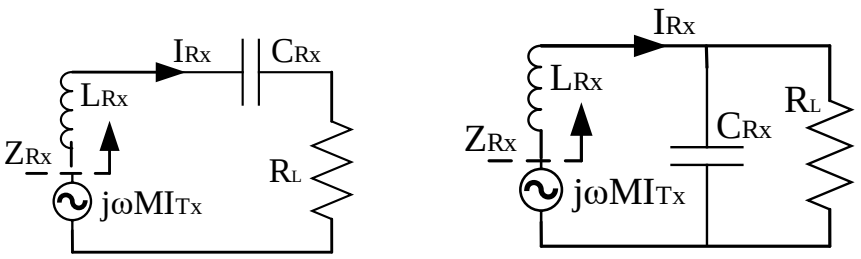
(d) Parallel-Parallel(PP)

Figure 2.2: Conventional IPT topologies.

Although the connection type of the resonant capacitor changes the IPT systems dynamics, all four topologies can be investigated separately for the Tx and Rx side. Regardless of the Tx side connection type, the sinusoidal current passing through the Tx side IPT coil induces an AC voltage source at the Rx side.

2.1.1.1 Receiver Side Compensation

Consider the Rx side compensation topologies given in Fig. 2.3. When the operating frequency is close to the resonant frequency, the impedance of the LC circuit



(a) Series-Series(SS) (b) Series-Parallel(SP)

Figure 2.3: Series and parallel connected Rx side.

converges to zero, which results in a single voltage source connected to a resistor. Therefore, series connected Rx side acts as a voltage source. When parallel connected, the system acts as a current source. A major advantage of parallel connection is the resonant capacitor sizing. In the parallel connected systems, only the ripple current passes through the capacitor. However, in the series connected Rx side, all current passes through the resonant capacitor. Hence, current carrying capability and sizing require special attention.

The advantages of series connection become clear when the Thevenin impedances are driven. The impedances seen by the EMF source for series and parallel connected Rx side are given in (2.5).

$$Z_{Rx-S} = j\omega L_{Rx} + \frac{1}{j\omega C_{Rx}} + R_L \qquad Z_{Rx-P} = j\omega L_{Rx} + \frac{R_L}{j\omega C_{Rx} R_L + 1} \tag{2.5}$$

For parallel connection, the resonant frequency depends on the load resistance. Although the reflected impedance on the Tx side is not yet discussed, the parallel connection results in

The input side impedance of all conventional topologies can be given as in Table 2.1.

Table 2.1: Input side impedance of conventional IPT topologies

Topology Type	**Reflected Impedance**
Series-Series	$Z_{in} = j\omega L_{Tx} + \frac{1}{j\omega C_{Tx}} + \frac{M^2\omega^2}{j\omega L_{Rx} + \frac{1}{j\omega C_{Rx}} + R_L}$
Series-Parallel	$Z_{in} = j\omega L_{Tx} + \frac{1}{j\omega C_{Tx}} + \frac{M^2\omega^2}{j\omega L_{Rx} + \frac{R_L}{j\omega C_{Rx} R_L + 1}}$
Parallel-Parallel	$Z_{in} = \frac{1}{j\omega C_{Tx}} \| (j\omega L_{Tx} + \frac{M^2\omega^2}{j\omega L_{Rx} + \frac{R_L}{j\omega C_{Rx} R_L + 1}})$
Parallel-Series	$Z_{in} = \frac{1}{j\omega C_{Tx}} \| (j\omega L_{Tx} + \frac{M^2\omega^2}{j\omega L_{Rx} + R_L + \frac{1}{j\omega C_{Rx}}})$

Although equations in Table 2.1 are rather long, a major advantage of series-series topology compared to topologies is the independence of resonant frequency from load resistance and magnetic coupling. Since there is no mutual inductance term for both resonator tanks, the phase of the input current is always zero at the resonant frequency. For the rest of the topologies, the resonance is dependent on M and the magnitude of R_L. A major disadvantage of series-series topology is the extremely high input currents for low loading of very small magnetic coupling. In SS IPT systems, the operation frequency is often kept very close to the resonant frequency to achieve a high power factor at the input side. Therefore, the impedance of both resonant tanks are very close to zero. When there is very low to no loading, the reflected impedance to the Tx side becomes very close to zero. Therefore, dangerously high input currents may flow limited by only the intrinsic impedance of the input IPT coil. Similarly, the reflected impedance converges to zero as the magnetic coupling decreases. The key features of all topologies can be summarized as in Table 2.2.

Table 2.2: Key Features of Different Conventional IPT Topologies

	S-S	S-P	P-P	P-S
Tx side Capacitor Sizing	Large	Large	Small	Small
Rx side Capacitor Sizing	Large	Small	Small	Large
No-load Operation	No	Yes	Yes	Yes
Load Change Independence	Yes	No	No	No
Coupling Change Independence	Yes	No	No	No
Source Type	VS	CS	CS	VS

2.1.2 Zero Voltage Switching in IPT Systems

Depending on the power levels, half and full-bridge converter topologies are often used at the Tx side. The power loss on power semiconductors can be divided into two parts: Conduction loss and switching loss. The conduction loss is the power generated as heat on the semiconductor due to internal resistance called $\mathrm{R_{ds,on}}$. The value of $\mathrm{R_{ds,on}}$ varies for each semiconductor and junction temperature. Therefore, for a chosen power MOSFET the only way is to include heatsinks to reduce the junction temperature. The switching loss occurs between small time intervals (ranging from a few ns to μs). The switching loss on a power MOSFET has the analytical formula given in (2.6).

$$P_{switching} = 0.5 V_{DS} I_{DS} (t_{rise} + t_{fall}) f_{switching}(W) \tag{2.6}$$

Switching loss given in (2.6), becomes the dominant power loss element at high frequencies. Therefore, there exist many topologies employing resonators to achieve zero voltage switching (ZVS) of zero current switching (ZCS). Regardless of the IPT topology, the aim is ZVS at MOSFET turn-on. Consider the half-bridge converter given in Fig. 2.4. The Tx side AC current is denoted by a sinusoidal current source.

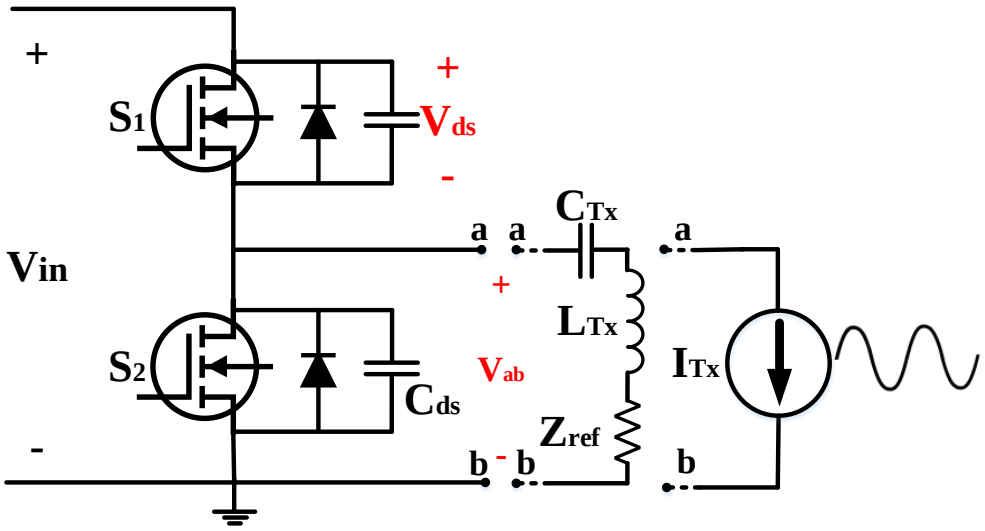


Figure 2.4: Half-bridge converter with parasitic C_{ds} capacitance and load.

2.1.2.1 Leading Power Factor

First, let us consider the leading power factor, meaning the I_{Tx} current leads the fundamental component of the square voltage input between V_{ab}. The experimental results for V_{ds}, I_{Tx} and V_{gs} are given in Fig. 2.5. When S1 is not conducting, the V_{ds} voltage is equal to 85 V. When V_{gs} is equal to 12 V, the gate turns on while the current flows in the opposite direction. Moreover, the V_{ds} voltage is non-zero. Therefore, hard-switching is made during gate turn-on.

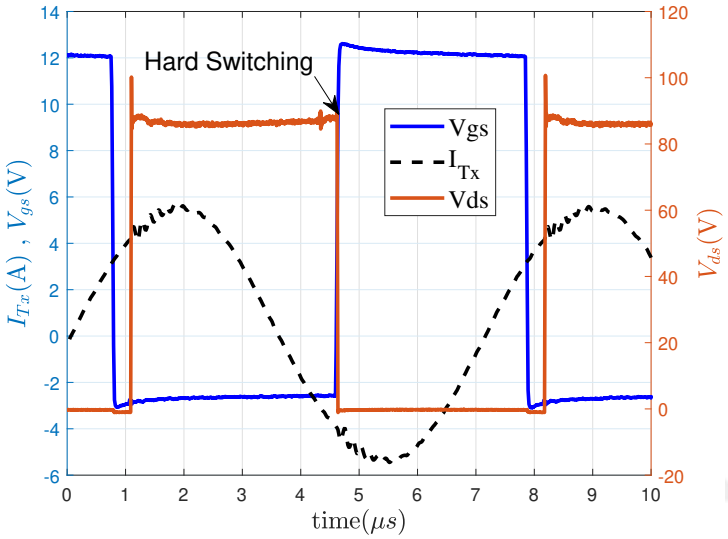


Figure 2.5: Leading power factor. The ZVS condition is not achieved.

2.1.2.2 Lagging Power Factor

Now, let us consider the lagging power factor, meaning the I_{Tx} current lags the fundamental component of the square voltage input between V_{ab}. The experimental results for V_{ds}, I_{Tx} and V_{gs} are given in Fig. 2.6. Initially, S1 is non-conducting, and hence the V_{ds} voltage is equal to 85 V. When S2 switch is turned off (both switches are non-conducting.) the positive current starts to discharge the C_{ds} capacitance, then V_{ds} is equal to -0.7 V, the body diode goes into conduction. Therefore, when gate turn-on signal is applied to V_{gs}, the voltage across V_{ds} is practically zero. Hence zero voltage switching is achieved.

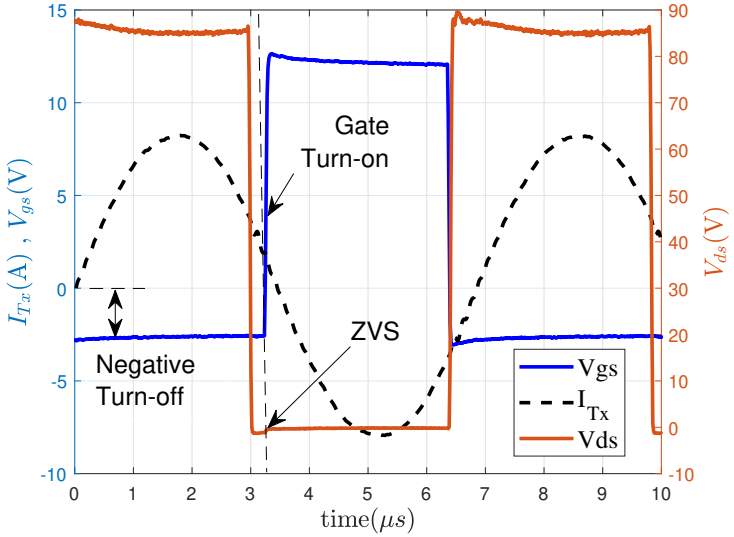


Figure 2.6: Lagging power factor. The ZVS condition is achieved.

2.1.3 Bifurcation Phenomenon in Doubly Tuned IPT Systems

In section 2.1.2, the importance of slightly inductive operation was discussed. In order to achieve ZVS during semiconductor turn-on, operation above resonant frequency. "Bifurcation", is the pole splitting phenomenon that may occur in doubly tuned systems such as conventional IPT topologies. While for most conditions operation above resonance ensures ZVS operation, in the presence of bifurcation there exists three distinct zero phase angle (ZPA) frequencies. This means even the operation above resonance is satisfied, inductive operation is not guaranteed. Consider the lumped circuit of an SS topology given in Fig 2.2. Using AC analysis, the input current I_{Tx} is swept for different magnetic coupling between the IPT coils. The phase angle between the fundamental component of the input voltage (V_{in}) and I_{Tx} is presented in Fig. 2.7.

For high coupling conditions there exists three ZPA points. Therefore, for SS topology under high magnetic coupling operation there exists a critical coupling value (k_c) where a higher coupling will surely introduce bifurcation to the system and ZVS operation is not guaranteed. A similar analysis can be made for constant coupling and variable loading as presented in Fig. 2.8.

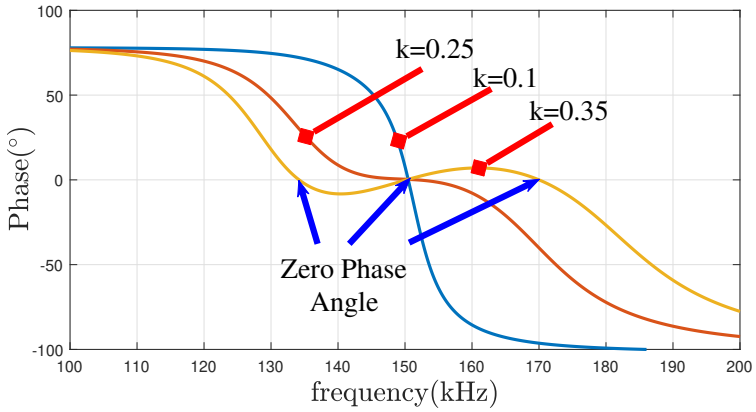


Figure 2.7: Phase angle between V_{in} and I_{Tx} for different magnetic couplings.

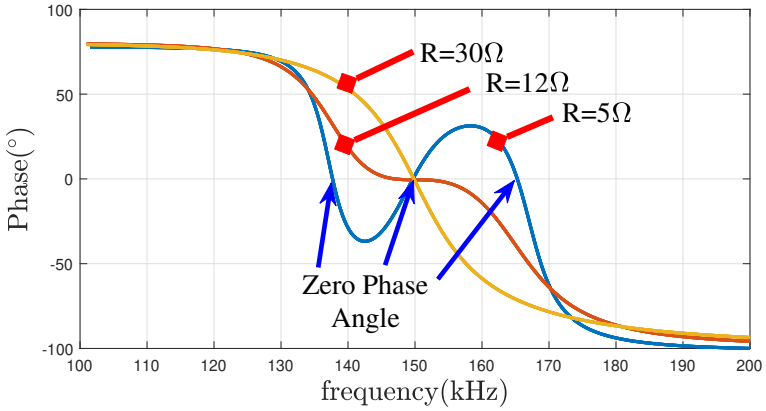


Figure 2.8: Phase angle between V_{in} and I_{Tx} for different loadings.

2.1.4 Modular IPT Systems

IPT systems use magnetic coupling to transfer power to the load side. While, in conventional systems a single load is present, multiple modules may be used for a variety of applications.

A possible system can be categorized as selective power transfer. The aim is to transfer power to a specific load by changing the operation frequency of the Tx module. While, all Rx coils are magnetically coupled with the Tx coil, the resonant frequencies of the Rx modules are adjusted to be distinct such that, induced voltage on the remaining Rx coil is highly suppressed by the LC filter [25, 26, 27].

Another possible system can be categorized as high order phase IPT system. This method is often employed as three phase unit where the transfered power is relatively high. Compared to conventional single phase IPT systems, the AC Tx current is generated by a three leg inverter and it consists of three Tx and Rx coils. The outputs are later connected into a common DC-bus. [28, 29].

Besides separate receivers, Rx modules are connected to a common DC-bus to increase the misalignment tolerance of the IPT system. Ke *et. al* investigate a multi-coil design with a common DC-bus, and propose receiver parallel compensated parallel DC-bus to avoid misalignment [30]. In [31], LCC-LCC compensation is used. The outputs of Rx modules are connected in parallel. Multi Tx modules are placed at a certain angle, and rotational misalignment tolerance is achieved. Another LCC-LCC compensation WPT system is designed in [32]. Two Tx module and two Rx modules are employed in the system for compact design and outputs of the Rx modules are parallel connected to achieve high power output. A 10 kW four receiver wireless power transfer system is designed in [33] for dynamic EV charging. Series-series compensation is used in the system and outputs of the modules are grouped in pairs and connected in parallel. Resultant two group is connected in series and output fluctuation is reduced. In [34], transmitter series receiver parallel compensation is used with 7 kW design and input parallel output series IPT system is analyzed to obtain high output voltage. In [35], a 6kW prototype was built using three 2kW modules where LCL-T topology is used. The outputs are connected in parallel, and the aim is to achieve redundancy and hence to increase fault tolerance and overall system reliability. A WPT system based on dual transmitters and dual receivers presented in [36] aims increase the power transfer capability with four transmission paths. Modular design provides lower cost and lower semiconductor ratings and improves the system reliability.

2.2 Initial System Considerations

In section 1.2, slip rings and brushless exciters were introduced. While they are suited to transfer power from a stationary frame to a rotating frame, constant friction and problematic low speed operation are major downsides of such systems. An IPT

system can operate at any given mechanical speed without the need of physical contact. Therefore, in this thesis, the aim is to design a rotating dynamic IPT system where 1 kW power can be transferred for a wide speed range. Since slip-rings and brushless exciters are used to supply power to electrical machines whose operations are critical, therefore reliability and fault tolerance is key during IPT system design. An illustrative system is given in Fig. 2.9

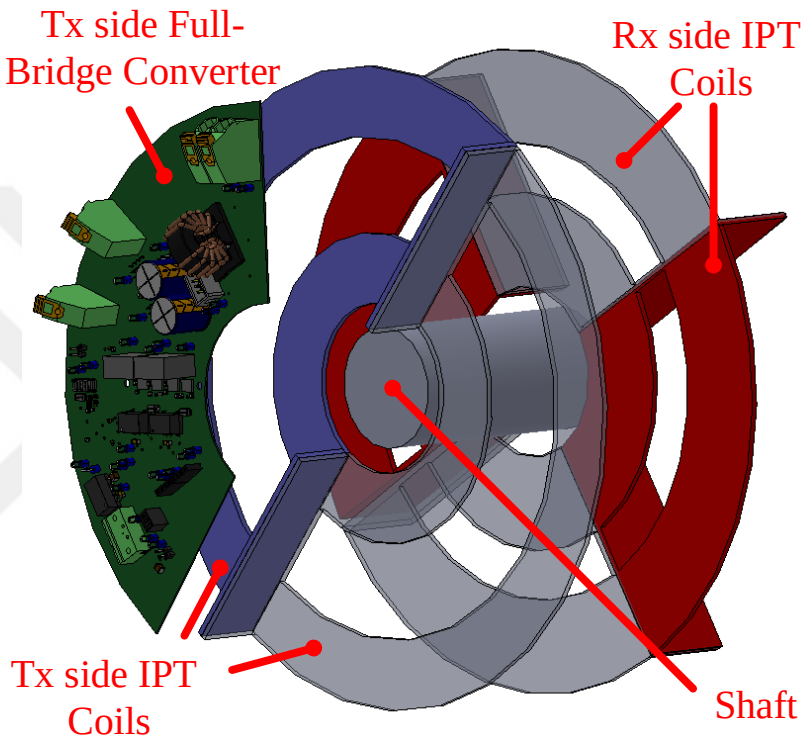
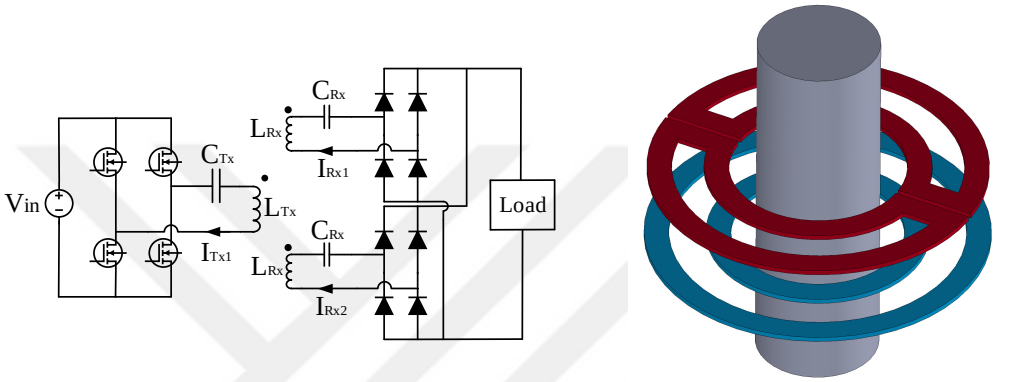


Figure 2.9: Illustration of the proposed system.

The system should be mounted around a rotating shaft where the Tx side is stationary, and the Rx side rotates with the shaft. The power transfer is achieved by magnetic coupling between the Tx and Rx coils. The air gap of the system is constant throughout the rotation. However, radial misalignment exists in such a system. Moreover, the loading can also be changed. In Table 2.2, key features of IPT topologies are given. Since load and coupling independent operation is required, series-series topology is selected.

A major downside of SS topology is the extremely high Tx currents for light to no-

load cases. Since the aim of the system is to achieve a reliable system, safe operation at open-circuited Rx fault conditions should be satisfied. As previously given in Table 2.2, no impedance is reflected to the Tx side if the coupling is zero. Therefore, guaranteeing reflected impedance under all conditions is necessary if this problem is to be addressed during the design procedure. A possible solution is to increase the number of Rx modules such that magnetic coupling is present even under a single Rx side open-circuited fault condition. Consider 1Tx-2Rx structure given in Fig. 2.10.



(a) 1Tx2Rx system circuit representation.

(b) 1Tx-2Rx rotational system (blue: Tx coil, red: Rx coils)

Figure 2.10: 1Tx-2Rx circuit representation and realistic rotational system.

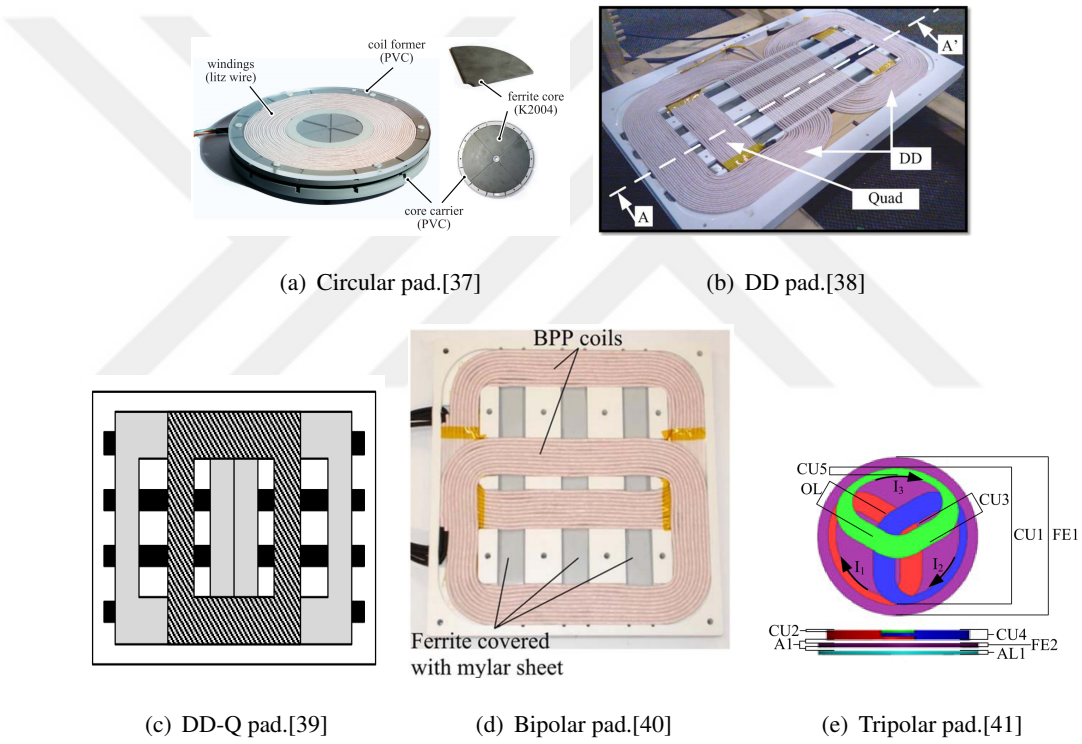
From an analytical perspective the reflected impedance to the Tx side can be given as in (2.7). Therefore, in the absence of a single Rx module, the power flow may be achieved using the other Rx module.

$$Z_{in} = j\omega L_{Tx} + \frac{1}{j\omega C_{Tx}} + \frac{M_1^2\omega^2}{j\omega L_{Rx1} + \frac{1}{j\omega C_{Rx1}} + R_{eq,1}} + \frac{M_2^2\omega^2}{j\omega L_{Rx2} + \frac{1}{j\omega C_{Rx2}} + R_{eq,2}} \tag{2.7}$$

While, using an extra Rx module is beneficial for continuous operation, effect of modular structure and module number on the fault tolerance is yet to be discussed in the upcoming sections.

2.2.1 IPT Coil Shape Consideration

Until now, the operation principles and the common power electronic topologies for IPT systems are discussed. Another major topic is the IPT coil design. While operation principles involve Faraday and Lenz Law, the shape of the IPT coil directly affects the overall system efficiency, airgap distance, and misalignment tolerance. Therefore, in the literature, different coil shapes are often investigated, such as circular pad, DD pad, DD-Q pad, bipolar pad, and tripolar pad, which are given in Fig. 2.11.



(a) Circular pad.[37] (b) DD pad.[38]

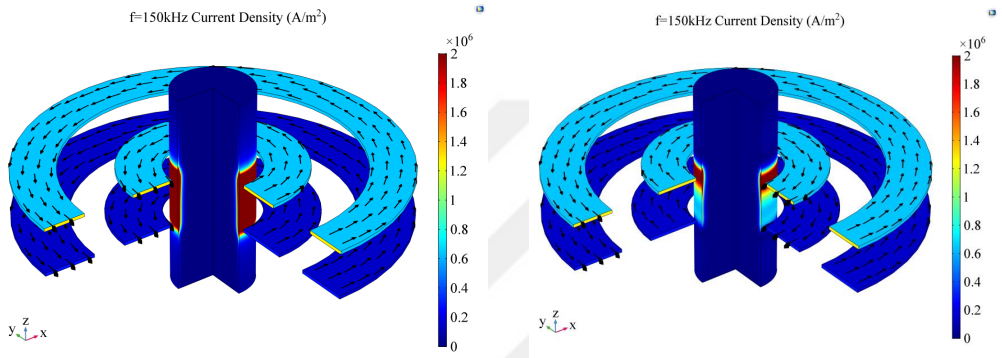
(c) DD-Q pad.[39] (d) Bipolar pad.[40] (e) Tripolar pad.[41]

Figure 2.11: Different IPT coil shapes employed in the literature.

In section 2.1, the effect of coupling and load variation on the overall system design was discussed. In stationary IPT systems, having high misalignment tolerance is beneficial to increase the overall DC-DC system efficiency for a wide range of operation. Conventional circular pads have the same misalignment tolerance for both directions. A method employed in the literature is polarization, where the flux lines are directed

in the same direction such that misalignment tolerance is significantly increased in a certain direction. DD and DD-Q pads are such examples.

Unlike common stationary IPT coils, the proposed system is planned to be mounted around a rotating shaft. Therefore, to eliminate any axial misalignment for different rotational angles, circular pad structure is found to be beneficial. Another required feature is the reduction of magnetic flux density on the shaft. Since operation frequencies of modern IPT systems are high, the eddy and core loss on the magnetic shaft may result in significantly reduced system efficiency.



(a) Windings with same current direction.

(b) Windings with opposite current direction.

Figure 2.12: Variation of induced current on the shaft for different coil geometries.

In Fig. 2.12, finite element(FE) simulations of two different circular coils are given. Compared to the opposite current flow case, when the current flows in the same direction both in the inner and outer loop (conventional circular spiral IPT coil shape), the flux passing through the shaft induces higher currents on the shaft. This is expected since the enclosed current is theoretically zero due to the Ampere law given in (2.1). Another benefit of such a coil shape is that the coils can be mounted or dismounted compared to a spiral coil since it can be mounted directly from the side instead of the end of the shaft. Also, by changing the radial angle Φ of each coil, the module number on both Tx and Rx sides can be increased.

A downside of such a coil shape is the reduced coil area. Compared to the circular spiral coil case, the inductance factor (A_L) will be lower. Therefore, for the same

inductance, more turns are necessary, which will increase the intrinsic resistance of the coil. While having a low intrinsic quality factor is undesired due to increased ohmic loss, the reduction of shaft loss and increased flexibility in mechanical and modular aspects outweigh this downside.

2.2.2 Module Number Selection

As discussed in section 2.1.1, series-series topology is prone to open-circuit faults. Moreover, in section 2.2, the effect of having two Rx modules was discussed where power flow can continue in case of a single Rx side open circuit fault. However, an exact number of modules is yet to be discussed.

During module number selection, the criteria are increased fault tolerance to single open circuit Rx side faults and equal power-sharing both in Rx and Tx sides.
Firstly, in Fig. 2.13, a single Tx and single Rx system is presented in its FHA form. The reflected impedance from the Rx to Tx is given in (2.8).

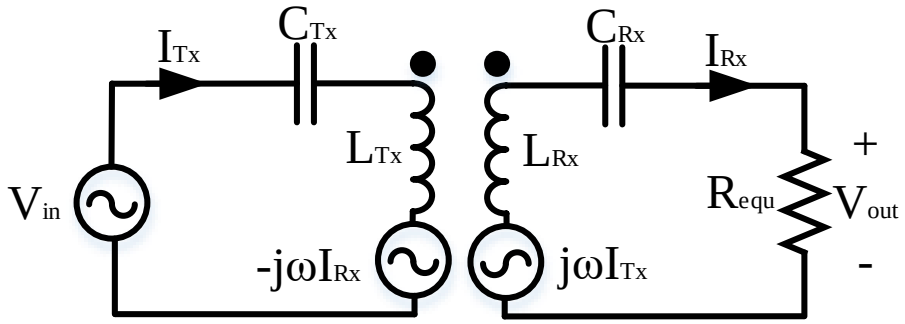


Figure 2.13: 1Tx-1Rx system with induced voltage components.

$$Z_r = \frac{\omega^2 M_1^2}{R_{equ1} + j\omega L_{Rx} + \frac{1}{j\omega C_{Rx}}} \tag{2.8}$$

For multiple Rx modules coupled with a single Tx side (2.8) can be improved as in.

$$Z_r = \sum_{n=1}^{k} \frac{\omega^2 M_{1,n}^2}{R_n + j\omega L_{Rx,n} + \frac{1}{j\omega C_{Rx,n}}} \tag{2.9}$$

The total impedance seen from the Tx side voltage source is given in 2.10.

$$Z_r = j\omega L_{Tx} + \frac{1}{j\omega C_{Tx}} + \sum_{n=1}^{k} \frac{\omega^2 M_{1,n}^2}{R_n + j\omega L_{Rx,n} + \frac{1}{j\omega C_{Rx,n}}} \tag{2.10}$$

Under the assumption that the Tx and Rx inductances and capacitances are equal, from 2.10 it can be stated that the Tx currents are equal if reflected impedance from the Rx side to the Tx sides are equal. Therefore, for equal power/current sharing in the Tx modules, the magnetic couplings should be the same. This statement can also be interpreted as, if the system is magnetically symmetrical equal power/current sharing is satisfied.

For better understanding, it is feasible to start from the simplest case where there is a single Tx and two Rx modules. The power-sharing between Tx modules are the same since there is only a single Tx module, and if a single Rx side is open-circuited, the operation can still continue since there is still a single Rx module coupled with the Tx module. However, in the case of Tx failure, operation under fault condition cannot be satisfied.

Another possible combination is two Tx and two Rx configuration. Although fault tolerance to the Tx side is increased, during an open circuit Rx fault, during constant rotation, there will definitely be an angle where no impedance is reflected to the Tx side. Therefore, a short circuit current will definitely flow.

In conclusion, having multi-Tx modules allow power-sharing and increase fault tolerance to Tx module faults. Similarly, having magnetic symmetry allows fault tolerance to open-circuited Rx faults. Therefore, the smallest number of modules satisfying the criteria is choosing two Tx and four Rx structure. Likewise, as long as the number of Tx side is greater than one and Rx module number is integer multiple of the number of Tx modules (except zero and one), both conditions are satisfied.

CHAPTER 3

ANALYTICAL DERIVATIONS FOR BIFURCATION FREE DESIGN AND CURRENT BALANCING METHODS

In Chapter 2, a general overview on the system proposal is given. In order to design a contactless slip ring, series-series topology is selected. An industrial slip ring requires improved fault tolerance and should be highly reliable, therefore a modular structure is proposed. The outputs of the Rx modules are connected in parallel to a common DC-bus where the system may continue its operation without interruption in the presence of an open-circuit fault.

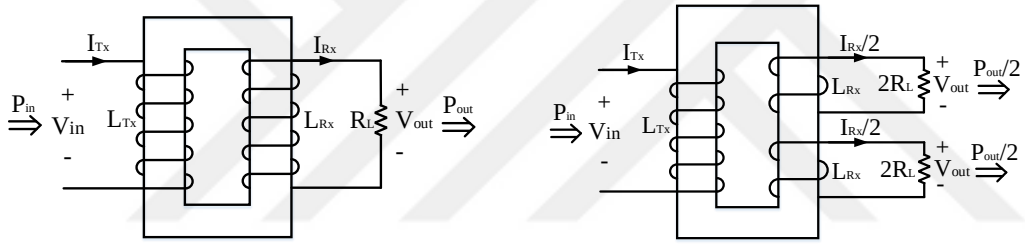
A major issue in doubly tuned IPT systems is the bifurcation phenomenon. To eliminate this effect during the design procedure, an analytical design methodology is necessary. Moreover, like most modular common DC-bus systems, current/power balancing is a major challenge. While, the proposed modular IPT system operation is speed independent and fault tolerant without any power balancing, high current may wear a single Rx module overtime which not only reduces the lifetime of the system but also introduces fault tolerance and reliability issues. Therefore, a current balancing method should be implemented in this study.

In this Chapter, first a bifurcation free design for a generalized modular IPT systems will be presented. Then, two current balancing methods will be introduced, which are addition of cross-coupling between the Rx modules and intentional detuning of the Rx side resonant frequency. This Chapter will include only the analytical derivations and simulation results, where the experimental verification of the overall system will be given in the upcoming Chapters.

3.1 Bifurcation Free Design

In this section, analytical modeling of the proposed system will be delivered. The generalization of single Tx-Rx to our system will be presented. Then bifurcation free operation limitations will be discussed analytically following similar but much more generalized approach presented by Aditya *et al.* in [42].

Let us start our modeling from the primary side of an ideal transformer which is presented in Fig.3.1(a). In case we double the resistance in the secondary windings, the output voltage stays the same, however, the current in each secondary coil is halved. This also results reduction in the secondary quality factor, denoted as $\mathrm{Q_{Rx}}$. The secondary quality factor is give in Eq. 3.1. The ω is the angular frequency, $\mathrm{L_{Rx}}$ is the secondary winding inductance and $\mathrm{R_L}$ is the secondary load resistance seen by the secondary side.



(a) Single Tx single Rx magnetic illustration.

(b) Single Tx double Rx magnetic illustration.

Figure 3.1: Single and double Rx module magnetic circuit illustration.

$$\mathrm{Q_{Rx}} = \frac{\mathrm{L_{Rx}}\omega}{\mathrm{R_L}} \tag{3.1}$$

Bifurcation occurs often in doubly tuned circuits, in our case it is the series-series compansation. During normal operation above resonant angular frequency, denoted as ω_0, zero voltage switching(ZVS) is guaranteed on the Tx side switches. However, when bifuration occurs there exits three zero phase angle (ZPA), where the Tx current may lead the Tx-voltage even if the operating angular frequency ω is above the resonant frequency ω_0. This is undesirable and should be eliminated in the design process if possible.

In our proposed model, it is important to determine which Tx-Rx alignment gives the critical coupling condition. Bifurcation is strictly related to the primary reflected secondary impedance. Hence, it is important to determine the maximum reflected resistance case for further derivation. The Tx side reflected impedance from a single Rx module is given in Eq.3.2 .

$$Z_r = \frac{\omega^2 M^2}{R_{Rx} + R_L + j\omega L_{Rx} + \frac{1}{j\omega C_{Rx}}} \tag{3.2}$$

The overall inductance matrix is given in Eq. .

$$L = \begin{bmatrix} L_{Tx1,Tx1} & M_{Tx1,Tx2} & M_{Tx1,Rx1} & M_{Tx1,Rx2} & M_{Tx1,Rx3} & M_{Tx1,Rx4} \\ M_{Tx2,Tx1} & L_{Tx2,Tx2} & M_{Tx2,Rx1} & M_{Tx2,Rx2} & M_{Tx2,Rx3} & M_{Tx2,Rx4} \\ M_{Rx1,Tx1} & M_{Rx1,Tx2} & L_{Rx1,Rx1} & M_{Rx1,Rx2} & M_{Rx1,Rx3} & M_{Rx1,Rx4} \\ M_{Rx2,Tx1} & M_{Rx2,Tx2} & M_{Rx2,Rx1} & L_{Rx2,Rx2} & M_{Rx2,Rx3} & M_{Rx2,Rx4} \\ M_{Rx3,Tx1} & M_{Rx3,Tx2} & M_{Rx3,Rx1} & M_{Rx3,Rx2} & L_{Rx3,Rx3} & M_{Rx3,Rx4} \\ M_{Rx4,Tx1} & M_{Rx4,Tx2} & M_{Rx4,Rx1} & M_{Rx4,Rx2} & M_{Rx4,Rx3} & L_{Rx4,Rx4} \end{bmatrix} \tag{3.3}$$

If all the modules are equal, the maximum reflected impedance occurs on the fully aligned case, where $\mathrm{M_{Tx1,Rx1}} = \mathrm{M_{Tx1,Rx2}}$. The coupling $\mathrm{M_{Tx1,Rx3}}$ and $\mathrm{M_{Tx1,Rx4}}$ are nearly zero hence they can be neglected. Moreover the inductance between the Tx coils, i.e. $\mathrm{M_{Tx1,Tx2}}$, is also nearly zero which will be discussed in next section, and hence it is neglected.

A critical coupling k_c for bifurcation free design was previously derived in [42]. In this paper, the derivation steps are the similar and hence some steps are omitted.
The VA rating of a single Tx coil is given in Eq. (3.4).

$$\mathrm{S_{in}} = \frac{\mathrm{V_{Tx,rms}^2}}{\mathrm{Z_{in}}} \tag{3.4}$$

Unlike single Tx-Rx case, the proposed system has two identical Rx coils coupled with a single Tx. Hence, the impedance at the Tx side can be written as in (3.5).

$$\mathrm{Z_{in}} = \frac{1}{\mathrm{j\omega C_{Tx}}} + \mathrm{j\omega L_{Tx}} + \mathrm{R_{Tx}} + 2\mathrm{Z_r} \tag{3.5}$$

Z_r is the Tx side reflected Rx impedance and can be expressed as in Eq. (3.6) .

$$Z_r = \frac{\omega^2 M^2}{R_L + R_{Rx} + j\omega L_{Rx} + \frac{1}{j\omega C_{Rx}}} \tag{3.6}$$

Putting (3.5) and (3.6) into (3.4) the equation becomes as in (3.7).

$$S_{in} = \frac{|V_{Tx,rms}|^2 R_{in}}{R_{in}^2 + X_{in}^2} + j\frac{|V_{Tx,rms}|^2 X_{in}}{R_{in}^2 + X_{in}^2} \tag{3.7}$$

The aim is to operate at unity power factor and hence X_{in} should be equal to zero. X_{in} is given in (3.8).

$$X_{in} = \omega L_{Tx} - \frac{1}{C_{Tx}\omega} - \mathbf{2}\frac{(\omega L_{Rx} - \frac{1}{\omega C_{Rx}})\omega^2 M^2}{(R_{Rx} + R_L)^2 + (\omega L_{Rx} - \frac{1}{\omega C_{Rx}})^2} \tag{3.8}$$

Following a similar derivation as stated in [42], the critical coupling for bifurcation free operation for two Rx coils coupled with a single Tx is given in (3.9).

$$k_c = \frac{1}{\sqrt{2}Q_{Rx}}\sqrt{1 - \frac{1}{4Q_{Rx}}} \tag{3.9}$$

Then the ZPA angular frequency at critical coupling can be stated as in (3.10).

$$\omega_{kc} = \omega_0\sqrt{\frac{4Q_{Rx}^2 - 2}{4Q_{Rx}^2 - 3}} \tag{3.10}$$

Although the derivation is made for two Rx coils coupled with a single Tx coil, the proposed modification to a single Tx-Rx critical coupling derivation can be generalized for n-many Rx modules coupled with a single Tx coil. The proposed series-series topology is given in Fig. 3.2.

The initial design parameters were given in Table 1.2. Throughout the design first harmonic approximation is made. First it is important to determine the fundamental component of the input voltage. In (3.11) the rms value is calculated. The $4/\pi$ term

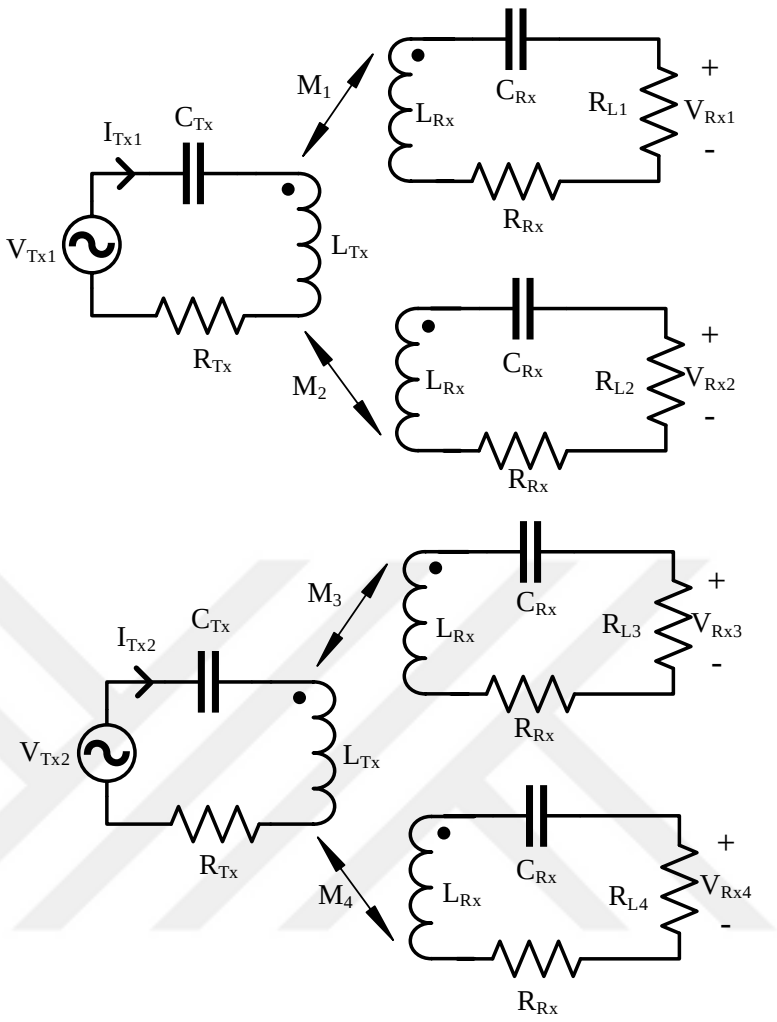


Figure 3.2: 2Tx-4Rx system FHA circuit schematic.

is used to calculate the peak of the fundamental sine component of the square voltage input waveform having 50% of duty cycle.

$$V_{fund,rms} = \frac{4V_{in}}{\pi\sqrt{2}} = 90\ V_{rms} \tag{3.11}$$

The DC output voltage is taken as 100 $\mathrm{V_{dc}}$. Since there is half symmetry in the two 1Tx-2Rx component can be connected in parallel and hence 500 W can be taken as the output power. Moreover, 150 kHz is selected as the resonant frequency, $\mathrm{f_0}$.

The next selection is the quality factor of the receiver side, $\mathrm{Q_{Rx}}$ which is given in (3.12). ω_0 is the resonant angular frequency.

$$Q_{Rx} = \frac{L_{Rx}\omega_0}{R_{equ}} \tag{3.12}$$

A common value of $\mathrm{Q_{Rx}}$ is between 1-10. Selecting a high quality factor significantly increases the capacitor voltage ratings and hence it directly effects the resonant capacitor sizing whereas selecting a low quality factor may effect the sinusoidal current input and may result in a very large frequency control range. However, as discussed in Fig. 3.1, the selected quality factor is divided by n during the generalization from a single Rx to n-many Rx modules. In the proposed design, the $\mathrm{Q_{Rx}}$ is selected as 4. Therefore, the critical coupling value is given in (3.13).

$$k_c = \frac{1}{Q_{Rx}\sqrt{2}}\sqrt{1 - \frac{1}{4Q_{Rx}^2}} = 0.33 \tag{3.13}$$

Since the output power $\mathrm{P_o}$ and the output DC voltage $\mathrm{V_{out,dc}}$ is known, the load can be determined as given in (3.14).

$$R_L = \frac{V_{out,dc}^2}{P_o} = \frac{100^2}{1000} = 10\ \Omega \tag{3.14}$$

At this point the model, Thevenin resistance seen by the combination of 2 Rx coils (500W case) can be calculated as given in (3.15). The term $8/\pi^2$ comes from the Thevenin resistance reflection of a full-bridge diode rectifier unit.

$$R_{equ} = 2R_L\frac{8}{\pi^2} = 16.21\Omega \tag{3.15}$$

Then the secondary inductance $\mathrm{L_{Rx}}$ can be calculated as in (3.16).

$$L_{Rx} = Q_{Rx}\frac{R_{equ}}{\omega_0} = 68.8\mu H \tag{3.16}$$

The secondary rms current $\mathrm{I_{s,rms}}$ can be calculated as in (3.17).

$$I_{Rx,rms} = \sqrt{\frac{P_o}{R_{equ}}} = 5.53A_{rms} \tag{3.17}$$

Assuming 100% efficiency the primary rms current $\mathrm{I_{Tx,rms}}$ and the mutual inductance are given in (3.18) and (3.19) respectively.

$$I_{Tx,rms} = \frac{P_o}{V_{in}} = 5.53A_{rms} \tag{3.18}$$

$$M = \frac{I_{Rx,rms} R_{equ}}{I_{Tx,rms} \omega_0} = 15\mu H \tag{3.19}$$

Since the $\mathrm{k_c} = 0.33$ selecting k=0.2 is a safe choice. Then the primary inductance $\mathrm{L_{Tx}}$ can be calculated as in (3.20).

$$L_{Tx} = \frac{M^2}{k^2 L_{Rx}} = 82\mu H \tag{3.20}$$

Finally the design parameter estimation can be concluded with the calculation of the primary capacitance $\mathrm{C_{Tx}}$ and secondary capacitance $\mathrm{C_{Rx}}$ whose values are given in (3.21) and (3.22) respectively.

$$C_{Tx} = \frac{1}{L_{Tx} \omega_0^2} = 13.8nF \tag{3.21}$$

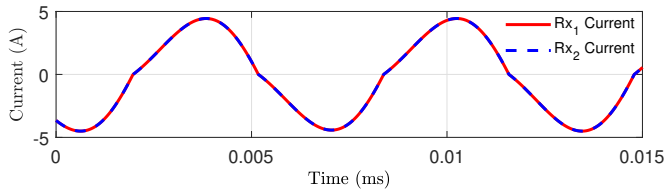
$$C_{Rx} = \frac{1}{L_{Tx} \omega_0^2} = 16.3nF \tag{3.22}$$

3.1.1 Current Balancing Issues in Rx Modules

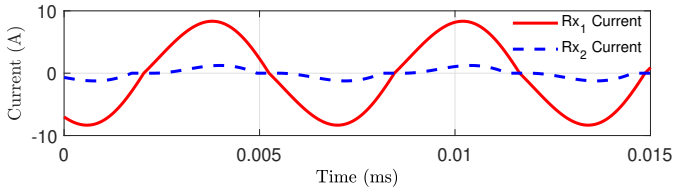
In parallel-connected Rx modules, maintaining equal current sharing between the modules is challenging as the module with the higher magnetic coupling becomes the main power delivery path. The output voltage is set by the module with higher coupling, and the rectifier diodes on the other module are blocked, which results in unbalanced current distribution as shown in Fig. 3.3. At this stage, no current balancing methods are introduced. The operating frequency is set to a frequency slightly higher than the resonant frequency to ensure an operation at the inductive region, which guarantees zero voltage switching at Tx side switches. Although the proposed system consists of 2Tx-4Rx modules, 1Tx-2Rx structure is employed for simplicity.

3.1.2 Rectifier Effect and Load Sharing

While the fundamental idea behind unequal current sharing is described previously, parallel-connected Rx modules with a common DC bus (see Fig. 2.10-a) requires



(a) 150kHz Decoupled Receivers Fully-Aligned Condition



(b) 150kHz Decoupled Receivers Misaligned Condition

Figure 3.3: The change in the receiver currents for equal and different magnetic coupling.

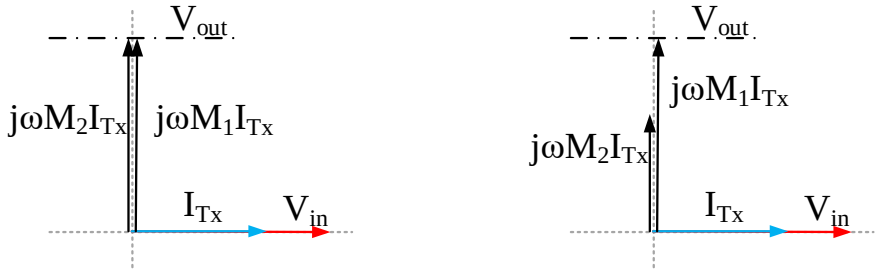
further analytical analysis. Although common DC voltage bus equalizes the voltage output of each Rx module, it doesn't mean equal power sharing. Actually, the reflected load resistance varies due to coupling unbalance between Tx and Rx modules. Since the system operates close to the design resonant frequency, the impedance of series connected LC resonant tank can be assumed to be zero. Then, it is possible to say that induced voltages at Rx modules can be conceivable as output voltage as shown in (3.23) and (3.24). This is also valid for Tx, and the equality is shown in (3.25).

$$V_{Rx,1} = j\omega M_1 I_{Tx} \tag{3.23}$$

$$V_{Rx,2} = j\omega M_2 I_{Tx} \tag{3.24}$$

$$V_{in} = -j\omega M_1 I_{Rx,1} - j\omega M_2 I_{Rx,2} \tag{3.25}$$

First, let us consider the equal coupling case without any cross-coupling. The phasor diagram of the input and induced voltages at Rx's are shown Fig. 3.4. In this case, the induced voltage of both Rx coils is equal to the output voltage. Thus, the designed circuit operates as desired, and Rx's share the power in equal. In the case of coupling mismatch, the Rx module with higher coupling has a higher induced voltage on its



(a) $M_1 = M_2$ (b) $M_1 \neq M_2$

Figure 3.4: Rx side induced voltages for equal and unequal magnetic couplings.

Rx side IPT coil, which is later rectified using the diode rectifier. The passive rectifier diodes on the less coupled module are reverse-biased, and hence most of the power is transferred by a single module. Due to the current unbalance, the reflected load resistance R_{eq} is lower for the higher coupled module. For parallel connected common DC-bus systems, the voltage at the input of the diode rectifier at the Rx side is equal. Therefore, a lower module current indicates a higher R_{eq}. For each parallel-connected Rx module, there exists another R_{eq} value that satisfies (3.26), where n is the total number of parallel-connected modules.

$$R_{eq,1}||R_{eq,2}||\ (...)\ ||R_{eq,n} = \frac{8}{\pi^2}R_L = R_{ref} \tag{3.26}$$

However, R_{eq} equals to R_{ref}/n when the module currents are balanced. For unbalanced current distribution, this value depends on operation frequency, difference in the mutual inductances ΔM, Tx side currents $I_{Tx,n}$.

3.2 Current Balancing Methods

The current balancing in parallel connected common DC-bus systems is necessary to achieve uniform power sharing. The current balancing effect of addition of cross-coupling between Rx coils and detuning the Rx resonant frequency will be investigated. Although the design consists of 2Tx-4Rx modules, the analysis are performed for 1Tx-2Rx system for a 500 W system. Then using magnetic symmetry, extra mod-

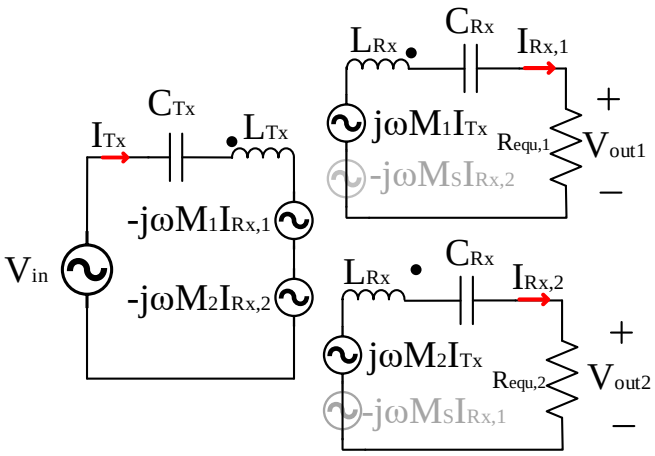


Figure 3.5: Parallel Rx modules with and without cross-coupling.(Grayports show the cross-coupling components).

ules are added to complete the system to 2Tx-4Rx without any extra analysis. The circuit representation of 1Tx-2Rx system given in Fig. 3.6.

3.2.1 Effect Of Receiver Cross-Coupling

The first proposed method for current balancing is to introduce cross-coupling between the Rx modules. Then the first harmonic approximation (FHA) circuit representation of the system can be represented as in Fig. 3.5. Compared to the case with no cross-coupling, there exist additional induced voltage components in the FHA circuit. The receiver with the larger coupling is named as the dominant Rx module, and the other is named as recessive Rx module. It is possible to observe the effect of cross-coupling using a phasor diagram, as shown in Fig. 3.7. In case of an unbalance between the module currents, the dominant module induces EMF on the recessive Rx coil, which lags the dominant module current by $90°$ as seen in Fig. 3.4. The vectorial sum of the induced EMF components on the recessive module due to Tx and dominant Rx module becomes higher. Thus, the output voltages of Rx modules are equalized, and power unbalance between receivers is avoided by this cross-coupling component.

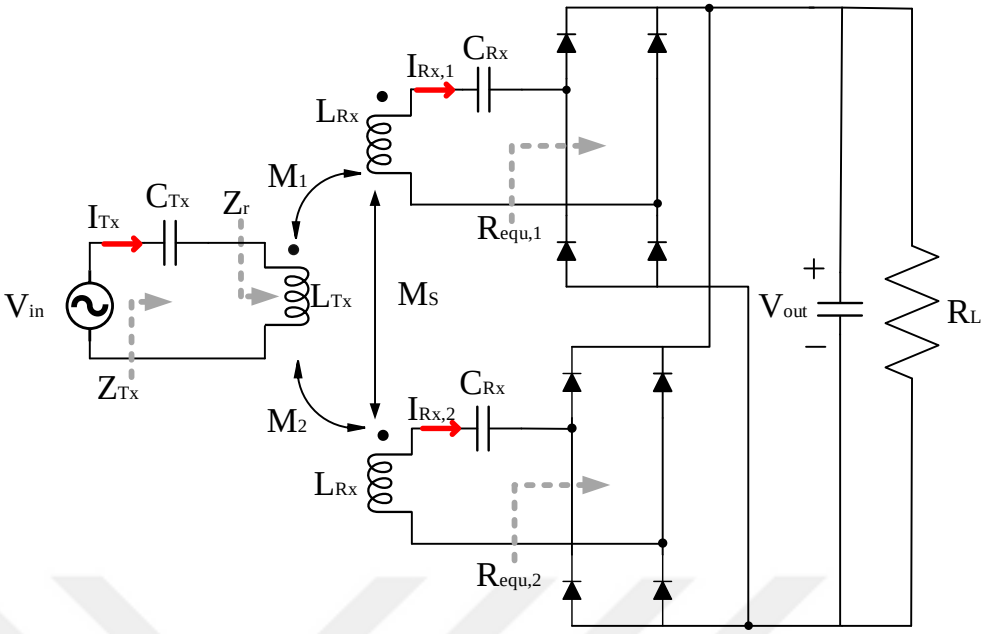


Figure 3.6: Parallel connected Rx's with common DC bus.

In Fig. 3.8, the effect of cross-coupling on the receiver currents is given. The improvement was given in Fig. 3.3. Receiver currents are equal in the ideal case with cross-coupled, as shown in Fig. 3.8-a. However, if the mutual inductance's between Tx and Rx modules are not identical but comparable, the majority of the power flows from a single module. In Fig. 3.8-b, one of the receiver mutual inductance between the transmitter is 10% smaller than the other and the cross-coupling is introduced as 70% of mutual inductance between receiver and transmitter. It can be observed that the current/power distribution is significantly improved by this cross-coupling component.

An analytical model is developed to determine the required optimum value of the cross-coupling. Although it may seem beneficial to increase the cross-coupling as much as possible, it is not feasible as increasing the coil winding length increases the resistive losses. In accordance with Fig. 3.5, the input and output voltages are defined as phasors as in Fig. 3.7 for the 1Tx-2Rx system with a resonant frequency of f_0.

$$V_{out,1} = j\omega M_1 I_{Tx} + j\omega M_s I_{Rx,2} \tag{3.27}$$

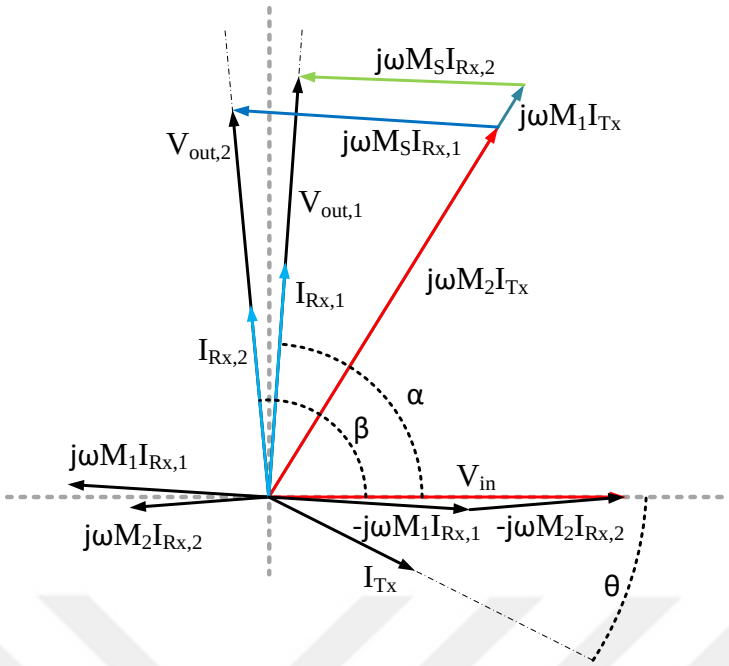


Figure 3.7: Phasor diagram for common DC bus parallel connected Rx modules with cross-coupling. The circuit components was given in Fig. 3.6.

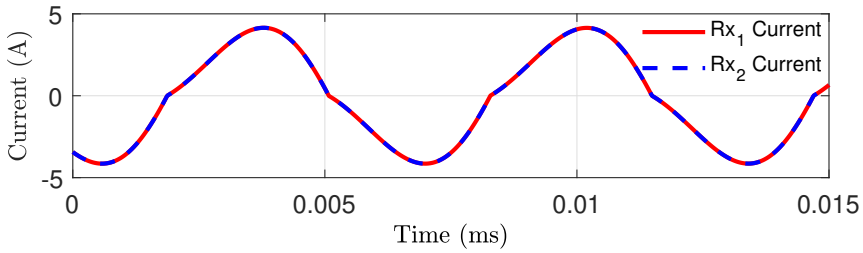
$$V_{out,2} = j\omega M_2 I_{Tx} + j\omega M_s I_{Rx,1} \tag{3.28}$$

$$V_{in} = -j\omega M_1 I_{Rx,1} - j\omega M_2 I_{Rx,2} \tag{3.29}$$

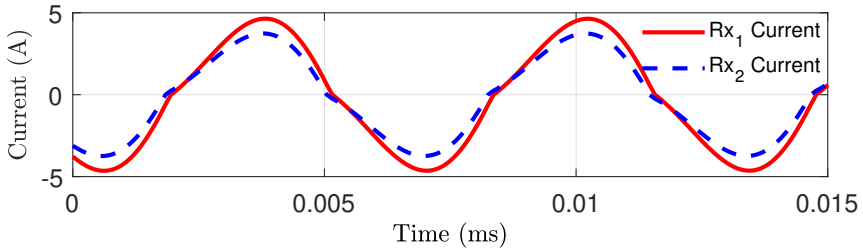
The magnitudes of the output voltages are equal but the phases depend on current of each Rx modules. The equations (3.27, 3.28, 3.29) in the phasor domain are transferred to time-domain equations (3.30, 3.31, 3.32) by considering the parameters shown in Fig. 3.7.

$$\begin{aligned} V_{out} \sin(\omega t - \alpha) &= \omega M_1 I_{Tx} \cos(\omega t - \theta) \\ &+ \omega M_s I_{Rx,2} \cos(\omega t - \beta) \end{aligned} \tag{3.30}$$

$$\begin{aligned} V_{out} \sin(\omega t - \beta) &= \omega M_2 I_{Tx} \cos(\omega t - \theta) \\ &+ \omega M_s I_{Rx,1} \cos(\omega t - \alpha) \end{aligned} \tag{3.31}$$



(a) 150 kHz Cross-coupled Fully-Aligned Condition



(b) 150 kHz Cross-coupled Misaligned Condition

Figure 3.8: Effect of cross-coupling on the Rx side current sharing.

$$\begin{aligned} V_{in}\sin(\omega t) = &-\omega M_1 I_{Rx,1}\sin(\omega t-\alpha) \\ &-\omega M_2 I_{Rx,2}\sin(\omega t-\beta) \end{aligned} \tag{3.32}$$

After the conversion, the orthogonal set can be divided into two parts as follows:

$$V_{out}\sin(\alpha) = -\omega M_1 I_{Tx}\cos(\theta) - \omega M_s I_{Rx,2}\cos(\beta) \tag{3.33}$$

$$V_{out}\cos(\alpha) = \omega M_1 I_{Tx}\sin(\theta) - \omega M_s I_{Rx,2}\sin(\beta) \tag{3.34}$$

$$V_{out}\sin(\beta) = -\omega M_2 I_{Tx}\cos(\theta) - \omega M_s I_{Rx,1}\cos(\alpha) \tag{3.35}$$

$$V_{out}\cos(\beta) = \omega M_2 I_{Tx}\sin(\theta) - \omega M_s I_{Rx,1}\sin(\alpha) \tag{3.36}$$

$$0 = -\omega M_1 I_{Rx,1}\cos(\alpha) - \omega M_2 I_{Rx,2}\cos(\beta) \tag{3.37}$$

$$V_{in} = -\omega M_1 I_{Rx,1}\sin(\alpha) - \omega M_2 I_{Rx,2}\sin(\beta) \tag{3.38}$$

The system parameters are shown in Table 3.1 for a 1Tx-2Rx system. By considering the input parameters, the output voltage is calculated in (3.39) and the projection of the Tx current on the Tx voltages is calculated (3.40) by neglecting the losses for now.

$$V_{out} = (I_{Rx,1} + I_{Rx,2})R_L \tag{3.39}$$

$$I_{pf} = I_p(\theta) = \frac{V_{out}(I_{Rx,1} + I_{Rx,2})}{V_{in}} \tag{3.40}$$

For negative cross-coupling, it is known that the dominant Rx current leads the input voltage in the range of 0 and 90 degrees. Also, it is known that the recessive Rx current leads the input voltage in the range of 90 and 180 degrees. The angles of Rx currents with respect to the input voltage can be found by using (3.37) and (3.38).

$$\delta = 180 - \arccos\left(\frac{V_{in}^2 - \omega^2 M_1^2 I_{Rx,1}^2 - \omega^2 M_2^2 I_{Rx,1}^2}{-2\omega^2 M_1 M_2 I_{Rx,1}^2}\right) \tag{3.41}$$

$$\alpha = -\arctan\left(\frac{\omega M_1 I_{s1} + \omega M_2 I_{Rx,1}\cos(\delta)}{\omega M_2 I_{Rx,1}\sin(\delta)}\right) \tag{3.42}$$

$$\beta = \alpha - \delta \tag{3.43}$$

It is possible to find the required cross-coupling ($\mathrm{M_s}$) by using (3.33) and (3.34) or (3.35) and (3.36). In these equations, θ and $\mathrm{M_s}$ are unknown parameters. These equations can be reshaped in the linear form by changing the parameters as $\tan(\theta)$ and M_s. The equations are brought $y = A^{-1}B$ form where A, B and y are shown in (3.44), (3.45) and (3.46).

$$A = \begin{bmatrix} \omega M_2 I_{pf} & \omega I_{Rx,1}\cos(90+\alpha) \\ 0 & \omega I_{Rx,1}\sin(90+\alpha) \end{bmatrix} \tag{3.44}$$

$$B = \begin{bmatrix} V_{out}\sin(\beta) \\ V_{out}\sin(\beta) - \omega M_2 I_{pf} \end{bmatrix} \tag{3.45}$$

$$y = \begin{bmatrix} \tan\theta \\ M_s \end{bmatrix} \tag{3.46}$$

The required cross coupling between Rx modules for a desired unbalance constraint can be calculated as shown in (3.47) which depends on the input parameters given in

Table 3.1. Although, the analitically deriven $\mathrm{M_s}$ seems to depend on $\mathrm{M_2}$ only, $\mathrm{I_{pf}}$ and $\mathrm{I_{Rx,1}}$ depend on the difference in the mutual inductances.

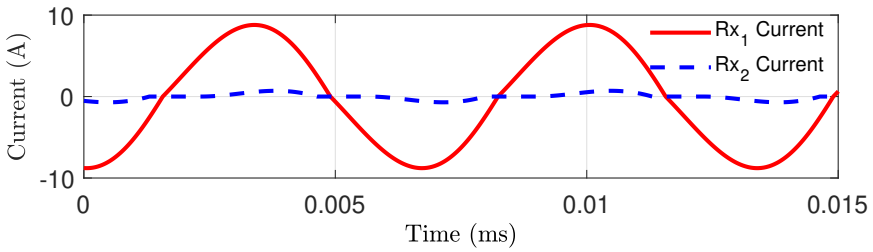
$$M_s = \frac{V_{out} \sin(\beta) - \omega M_2 I_{pf}}{\omega I_{Rx,1} \cos(90 + \alpha)} \tag{3.47}$$

The scenario of a 5% difference between mutual inductances is presented in Table 3.1. Here it is important to note that the choice of 5% is not arbitrary and reasoning will be clearer in the IPT coil design presented in the next Chapter. For this scenario, the desired current balancing ratio (CBR) is chosen as 82% (defined in (3.48)), and the required cross-coupling is calculated as 0.167 ($\mathrm{M_s} = 11.02\ \mu\mathrm{H}$). Here it is important to note that the choice of 82% is arbitrary and it is at the designers control. However, a high CBR will surely result in a higher Rx side mutual inductance. The simulation results for the derived values are given in Fig. 3.9.

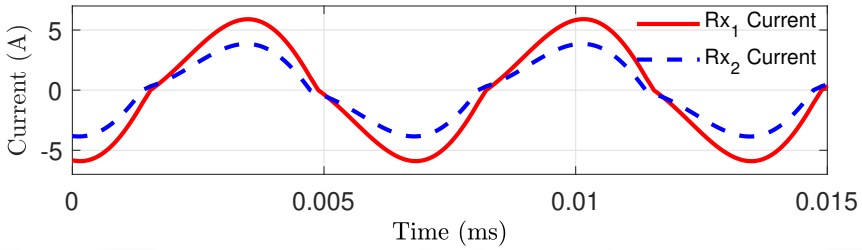
$$\mathrm{CBR}(\%) = 100(1 - \frac{|\mathrm{I_{Rx1}} - \mathrm{I_{Rx2}}|}{\mathrm{I_{total}}}) \tag{3.48}$$

Table 3.1: Cross-coupled analytical input parameters and results

Input Parameters	**Values**	**Derived Parameters**	**Values**
$\mathrm{f_0}$	150 kHz	$\mathrm{V}_{out}(rms)$	112.2 V
L_{Tx}	82 μH	α	76.7°
L_{Rx}	66 μH	β	110.8°
$\mathrm{M_1}$	14.71 μH	$\mathrm{I}_{Tx}(rms)$	8.6 A
$\mathrm{M_2}$	13.97 μH	θ	19.5°
$\mathrm{V}_{in}(rms)$	90 V	M_s	11.02 μH
$\mathrm{I}_{Rx,1}(rms)$	4.1 A		
$\mathrm{I}_{Rx,2}(rms)$	2.8 A		
R_L	20 Ω		



(a) 150 kHz Decoupled Condition ($I_{Rx1} = 6.2A_{rms}, I_{Rx2} = 0.5A_{rms}$)



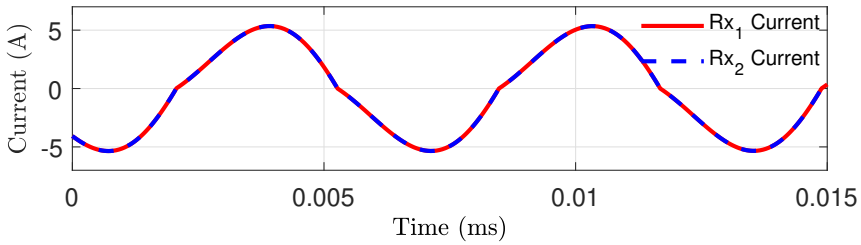
(b) 150 kHz Cross-Coupled Condition ($I_{Rx1} = 4.1A_{rms}, I_{Rx2} = 2.7A_{rms}$)

Figure 3.9: Effect of cross-coupling on the current sharing for misaligned case.

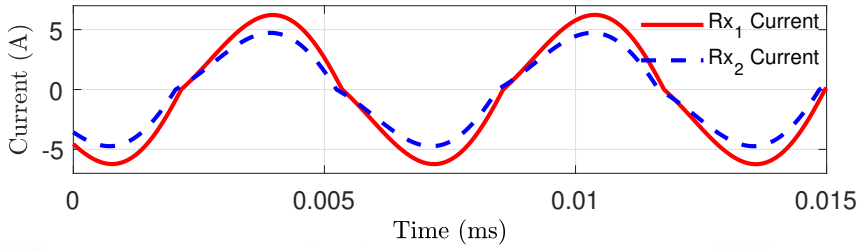
3.2.2 Intentional De-tuning of the Receiver Side Resonant Tank

It is observed that increasing operating frequency (while keeping the resonant frequency constant) results in a more balanced current distribution. However, as the operating frequency deviates further from the resonant frequency, the output voltage decreases, and hence the output power reduces. The same current balancing effect can be achieved by intentional de-tuning of the receiver resonant tank for unbalanced modules. Feng *et al.* investigate a detuned 1Tx-1Rx system, and the effect of varying coupling coefficient is analyzed [43]. In this section, the effect of Rx side detuning on current sharing is expanded for a 1Tx-2Rx system. Firstly, an analytical model is derived for a single Tx and single Rx system, and the effect of operation frequency and resonant tank frequencies are discussed. Secondly, a similar approach is used to analyze the effect of Rx side de-tuning for a 1Tx-2Rx system.

The FHA circuit representation of the 1Tx-1Rx system is presented in Fig. 3.11. The Tx and Rx resonant tank impedances are presented in (3.49) and (3.50). Then, the impedance matrix (3.51) can be solved for the transmitter and receiver currents as



(a) 135kHz Decoupled Receivers Fully-Aligned Condition



(b) 135kHz Decoupled Receivers Misaligned Condition

Figure 3.10: Effect of detuning on the current sharing.

shown in (3.52) and (3.53).

$$jL_{Tx}(\frac{\omega^2-\omega_{Tx}^2}{\omega^2}) = jL_{Tx}(\Delta\omega_{Tx}) \tag{3.49}$$

$$jL_{Rx}(\frac{\omega^2-\omega_{Rx}^2}{\omega^2}) = jL_{Rx}(\Delta\omega_{Rx}) \tag{3.50}$$

$$\begin{bmatrix} V_{in} \\ 0 \end{bmatrix} = \begin{bmatrix} Z_{Tx} & j\omega M \\ j\omega M & -Z_{Rx} \end{bmatrix} \begin{bmatrix} I_{Tx} \\ I_{Rx} \end{bmatrix} \tag{3.51}$$

$$I_{Tx} = \frac{V_{in}(-L_{Rx}\Delta\omega_{Rx} + jR_L)}{L_{Tx}R_L\Delta\omega_{Tx} + j(M^2\omega^2 + L_{Tx}L_{Rx}\Delta\omega_{Tx}\Delta\omega_{Rx})} \tag{3.52}$$

$$I_{Rx} = \frac{M\omega V_{in}}{L_{Tx}R_L\Delta\omega_{Tx}\Delta\omega_{Rx} + j(M^2\omega^2 + L_{Tx}R_L\Delta\omega_{Tx})} \tag{3.53}$$

In conventional series-series IPT systems, the Tx and Rx side resonant tank frequencies are chosen equally in order to achieve load/coupling independent operation. However, it is shown in this paper that for common DC bus parallel-connected multi-Rx systems, the current sharing can be improved by intentional de-tuning. When both Tx and Rx frequencies are equal to each other, the Tx and Rx currents can be derived

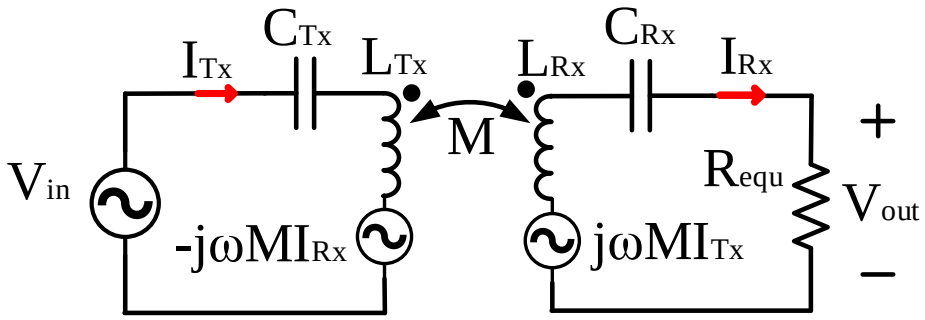


Figure 3.11: First harmonic approximation of single transmitter single receiver IPT system.

as in (3.54) and (3.55) respectively. Under this condition, the Rx current lags the Tx current by 90°.

$$I_{Tx} = \frac{V_{in} R_L}{M^2 \omega^2} \tag{3.54}$$

$$I_{Rx} = \frac{-jV_{in}}{M\omega} \tag{3.55}$$

However, if the Rx resonant tank is de-tuned and the operating frequency is kept at the resonant frequency of the Tx, the Tx and Rx currents can be derived as in (3.56) and (3.57).

$$I_{Tx} = \frac{V_{in} R_L}{M^2 \omega^2} + \frac{jV_{in} L_{Rx} \Delta\omega_{Rx}}{M^2 \omega^2} \tag{3.56}$$

$$I_{Rx} = \frac{-jV_{in}}{M\omega} \tag{3.57}$$

Therefore, detuning the Rx side results in either leading or lagging Tx current while the Rx current stays the same. If the resonant frequencies of the Rx's are chosen below the resonant frequency of the Tx side, the overall system resonant frequency will be above the resonant frequency of the transmitter and vice-versa. The analytical derivations can be expanded for a 1Tx-2Rx system as shown in Fig. 3.5. The cross-coupling is ignored during derivation of Rx side detuning, and the rectifier can be

modeled as a variable load with common output voltage. The matrix equations for the system are shown in (3.58) and the receiver currents as in (3.59) and (3.60) are obtained.

$$\begin{bmatrix} V_{in} \\ 0 \\ 0 \end{bmatrix} = \begin{bmatrix} Z_{Tx} & j\omega M_1 & j\omega M_2 \\ j\omega M_1 & -Z_{Rx,1} & 0 \\ j\omega M_1 & 0 & -Z_{Rx,2} \end{bmatrix} \begin{bmatrix} I_{Tx} \\ I_{Rx,1} \\ I_{Rx,2} \end{bmatrix} \tag{3.58}$$

$$I_{Rx,1} = \frac{jI_{Tx}M_1\omega^2}{R_{L1}\omega + j(L_{Rx}^2(\omega^2 - \omega_{Rx}^2))} \tag{3.59}$$

$$I_{Rx,2} = \frac{jI_{Tx}M_2\omega^2}{R_{L2}\omega + j(L_{Rx}^2(\omega^2 - \omega_{Rx}^2))} \tag{3.60}$$

Although the load distribution of the modules are unknown, the magnitude of the voltages are equal as shown in (3.61). The extended formulation is shown in (3.62).

$$R_{L1} \mid I_{Rx,1} \mid = R_{L2} \mid I_{Rx,2} \mid \tag{3.61}$$

$$\begin{aligned} I_{Tx}M_1\omega^2 R_{L1}\sqrt{R_{L1}^2\omega^2 + L_{Rx}^4(\omega^2 - \omega_{Rx}^2)^2} \\ -I_{Tx}M_2\omega^2 R_{L2}\sqrt{R_{L2}^2\omega^2 + L_{Rx}^4(\omega^2 - \omega_{Rx}^2)^2} = 0 \end{aligned} \tag{3.62}$$

When $\omega = \omega_{Rx}$, (3.63) can be derived. For this equation to be valid, either R_{L1} or R_{L2} must go to infinity since $M_1 \neq M_2$.

$$I_{Tx}M_1\omega^3 R_{L1}R_{L2} - I_{Tx}M_2\omega^3 R_{L1}R_{L2} = 0 \tag{3.63}$$

However, if $\omega \neq \omega_s$ and with the assumption of a high quality factor, (3.64) can be obtained. Using the same assumptions, (3.62) can be written as in (3.65).

$$\sqrt{R_{L2}^2\omega^2 + L_{Rx}^4(\omega^2 - \omega_{Rx}^2)^2} = L_{Rx}^2(\omega^2 - \omega_{Rx}^2) \tag{3.64}$$

$$I_{Tx}\omega^3 L_{Rx}^2(\omega^2 - \omega_{Rx}^2)(M_1R_{L1} - M_2R_{L2}) = 0 \tag{3.65}$$

By simplifying (3.65) and under the assumption that the Rx side is detuned and the quality factor is high, the load distribution is inversely proportional to the mutual inductances ratio as shown in (3.66).

$$\frac{R_{L1}}{R_{L2}} = \frac{M_2}{M_1} \tag{3.66}$$

In summary, increasing operation frequency while keeping the same resonant tank at Tx and Rx results in a better current distribution. However, as the frequency gets further into the inductive region, the power output decreases. If the Rx side resonant frequency is decreased, the maximum balancing can be achieved as provided in (3.66). Moreover, with detuning operation at the resonant frequency is still achievable without any loss in the maximum power delivery capability. Again without any change, frequency control can be used to control the power output. The simulation result for the normal and de-tuned receiver is given in Fig. 3.10.

A major disadvantage of a detuned Rx side is the variation of the resonant frequency for different loading and couplings. In the literature, a series-series topology is usually selected for its independence of resonant frequency for variable operating conditions[44, 45]. In our final 2Tx-4Rx design, the variation of the reflected impedance is minimized. As the Rx modules rotate, the Tx side the magnetic coupling with another Rx module while it decreases with the other Rx module. Therefore, change in the resonant frequency is minimal in our system.

3.3 Summary

In this Chapter, an analytical bifurcation free design for a 2Tx-4Rx system is presented. The derivation was based on a previous work presented in [42]. Since, the proposed system is symmetric, the analysis are performed for 1Tx-2Rx system where the findings are directly applicable to 2Tx-4Rx systems.
In the next section, two novel current balancing method for series-series compensated, parallel connected common DC-bus system are given. The first proposed method is the addition of cross-coupling between the Rx modules such that, the induced voltage on each Rx side IPT coil is equalized. The analytical derivations are performed for a initially given minimum current balance ratio which is selected as 82%. Moreover, the initial assumption of a maximum of 5% coupling difference is taken from the FEA results which will be given in detail in Chapter 4. Then the minimum required cross-coupling is calculated for 1Tx-2Rx system as -0.166. The next proposed method is the intentional detuning of the Rx side resonant frequency. Intentional detuning in-

troduces inductive or capacitive component on the Rx side current. This results in slight shift of the initially selected resonant frequency. However, combined with the cross-coupling method, nearly the same gain plot as the initial bifurcation free design can be achieved which will be presented in Chapter 5. Finalized 2Tx-4Rx system parameters are presented in Table 3.2.

Table 3.2: Finalized System Parameters for 2Tx-4Rx System

f_0	150 kHz	$P_{in,DC}$	1000 W
f_{Tx}	150 kHz	f_{Rx}	135 kHz
L_{Tx}	82 μH	C_{Tx}	13.8 nF
L_{Rx}	66 μH	C_{Rx}	21 nF
$k_{Tx,Rx}$	0.2 μH	$k_{Rx,Rx}$	-0.162
$M_{Tx,Rx}$	15 μH	M_s	11.02 μH
V_{DC}	100 V_{DC}	V_{out}	100 V_{DC}
R_L	10 Ω		

CHAPTER 4

IPT COIL AND PCB DESIGN

In section 2.2, the first design considerations were introduced. Later in Chapter 3, an initial system was designed analytically. Then, the simulations showed a current unbalance problem. This problem was solved with the addition of cross-coupling between the Rx modules and intentional detuning of Rx side resonant frequency. However, until this point, no practical design was presented. In this Chapter, the IPT coil geometry will be determined using finite element analysis. Then, Tx side full bridge-converters, Rx side full bridge diode rectifiers will be designed . In Table 3.2, the finalized analytical parameters were given.

4.1 IPT Coil Design

The IPT coil design plays an important role in the overall system efficiency. The aim during IPT design is to achieve the highest intrinsic quality factor for the desired inductance. This statement can also be interpreted as using the minimum amount of copper for a predetermined inductance. Although there are different IPT coil geometries and many optimization methods to increase the overall efficiency, in this thesis, no optimization method is used during the design process.

In Chapter 1, the effect of coil geometry on the shaft eddy loss was discussed. For a conventional spiral IPT geometry, the eddy losses were found significantly higher than the proposed IPT coil in Fig. 2.12. A major downside of this geometry is the reduction of the coil area, which results in a lower intrinsic quality factor for a specific inductance value. This trade-off can be reduced by increasing the coil size, which

also increases the air gap between the Tx and Rx modules.

In Chapter 3, the addition of cross-coupling on the current balancing was discussed. In the finalized analytical design, the parameters are given as in Table (4.1). The IPT coil designs are performed in ANSYS Maxwell.

Table 4.1: Self and Mutual Inductances of the Proposed System

L_{Tx}	82 μH
L_{Rx}	66 μH
M_{Tx-Rx}	15 μH
M_{Rx-Rx}	11 μH

Another issue is the selection of litz wire strand diameter and number. Firstly, the skin depth should be calculated. During calculation, 200 kHz is taken as the peak frequency. Skin depth (δ) at 200 kHz is calculated as in (4.1) where ρ is the resistivity, μ is the permeability of copper. AWG38 with 0.1 mm diameter is found suitable.

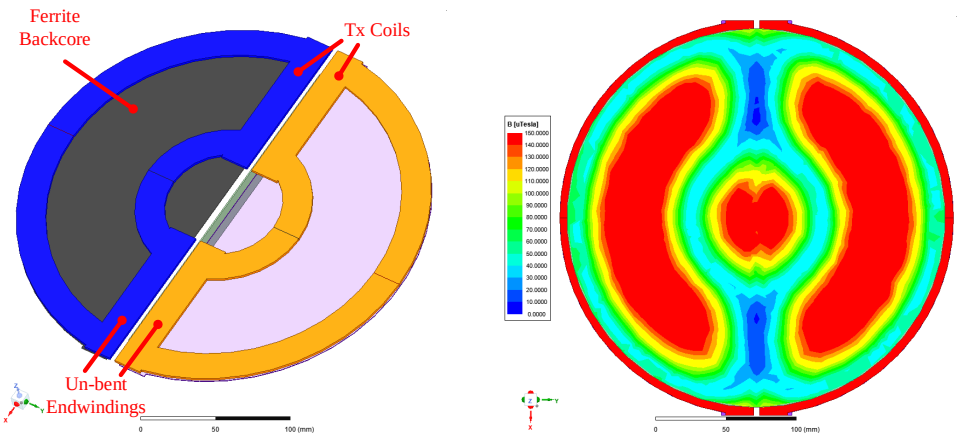
$$\delta(200\ kHz) = \sqrt{\frac{\rho}{\pi \mu f}} = 146 \mu m \tag{4.1}$$

The RMS current of the Tx side is 6.5 A. Taking the current density as $J = 4\ A/mm^2$ results in $1.6\ mm^2$ copper area. Knowing that the copper area of AWG38 is 0.008 mm^2 a total of 200 strands should practically suffice. However, strand number is selected as 300, such as safety factor which resulted in a litz wire with 2 mm diameter. The same litz wire is used for both Tx and Rx sides.

4.1.1 Tx Side IPT Coil Design

In Chapter 3, the effect of current balancing due to coupling mismatch was discussed, and two methods were introduced. The coupling mismatch occurs due to different flux linkages. Therefore, the aim during Tx side IPT coil design is to achieve a uniform radial flux density in the airgap. Consider the half-circle IPT coil in Fig. 4.1

which is somewhat similar to the spiral coil shape. Using FEA, the radial airgap flux density can be calculated as in Fig. 4.1.

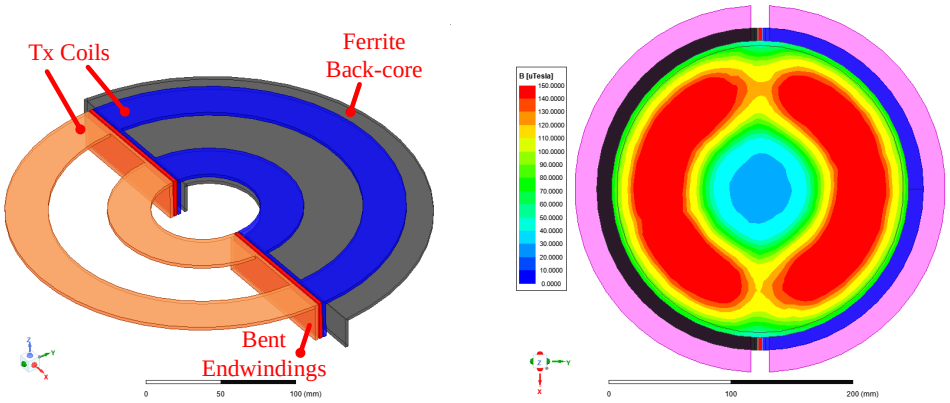


(a) Tx coil geometry. (b) FEA result

Figure 4.1: Un-bent end-winding Tx side IPT coil geometry and airgap B-field density.

As given in Fig. 4.1, the magnetic field density changes at the end-windings of the coil geometry. This results in unequal flux linkage between the Rx modules and hence introduces current unbalance. A possible solution is to bend the end-winding of the Tx side IPT coils such that a much more uniform flux density in the air gap is achieved. However, bending the end winding also introduces cross-coupling between the Tx modules, which is undesired. Therefore, a ferrite strip should be inserted as magnetic shielding. Since the total coil area increases, the inductance of the bent Tx coils are larger than the coils given in Fig. 4.1. Therefore, for the same inductance value, the coils given in Fig. 4.2 will surely have a lower number of turns. Decreasing the number of turns results in lower magnetic field density for the same airgap, and hence the air gap should be decreased to achieve the same magnetic coupling between the Tx and Rx modules.

In the literature, ferrite back-core are used both as flux guide and shielding purposes [37]. Moreover, the addition of ferrite back-core significantly increases the overall coil inductance. Therefore, the same inductance can be obtained with less number of turns, which means less copper and resistance, which results in higher system efficiency. As for magnetic shielding, the ferrite back-core guides the magnetic field and



(a) IPT coil geometry.

(b) FEA result.

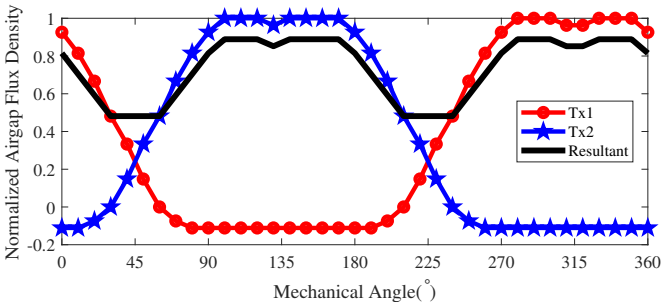
Figure 4.2: Bent end-winding Tx side IPT coil geometry and airgap B-field density.

encloses the magnetic field between the Tx and Rx coils. This reduces EMI problems on PCB that are in the vicinity of the IPT coils. For shielding material, I 20x14x2 mm N87 ferrite from TDK/EPCOS with B66483P0000X187 manufacturer part number is used.

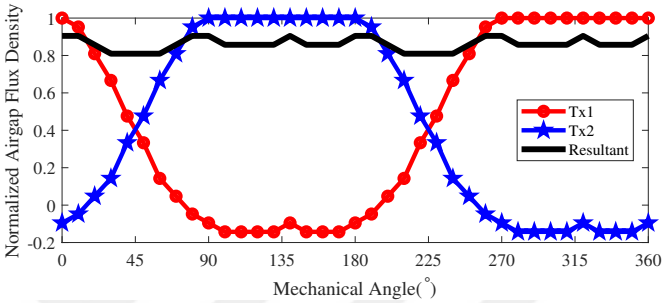
The 2Tx-4Rx system is modeled in Maxwell environment, and a parametric sweep is applied to the rotational angle of a single Rx coil which models a search coil. The normalized non-bended and bent end winding FEA results are given in Fig. 4.3. Compared to non-bent coil geometry, the flux density (B_z) is significantly more uniform in the airgap. This decreases the change in total magnetic coupling of the Rx coils and hence reduces the change of induced voltage. Less difference in the induced voltages reduces the current unbalance and hence less Rx side cross-coupling is required. However, a downside of this method is the increased copper length of the Tx coils which slightly decreases the intrinsic quality factor.

4.1.2 Rx Side IPT Coil Design

In Table 4.1, the Rx side inductance is given as $66\ \mu H$. In addition, each Rx coil should have $-11\ \mu H$ mutual inductance with the adjacent coil. Similar to the Tx IPT coil design, the upward curvature of the Rx coils results in a negative cross-



(a) Magnetic couplings between the Tx-Rx coils for non-bended endwinding configuration.



(b) Magnetic couplings between the Tx-Rx coils for bended endwinding configuration.

Figure 4.3: Tx-Rx couplings of non-bended and bended endwinding for a complete rotation.

coupling. By changing the area of the end-windings, it is possible to control the cross-coupling without any significant change in the overall coil inductance. The Rx side coil geometry is presented in Fig. 4.4. Similar to the Tx coil I 20x14x2 mm N87 ferrite from TDK/EPCOS with B66483P0000X187 manufacturer part number is used as back-core.

4.1.3 Reduction of Ferrite Core Requirement

Compared to conventional high-frequency transformers used in power electronics isolated converters, IPT coils have significantly higher airgaps, and hence the equivalent reluctance of the magnetic circuit model is high. Therefore, the change in the inductance with the addition of ferrite back-core is mostly to guide the magnetic field and shield the outer components from EMI. Moreover, to increase the air gap, the major-

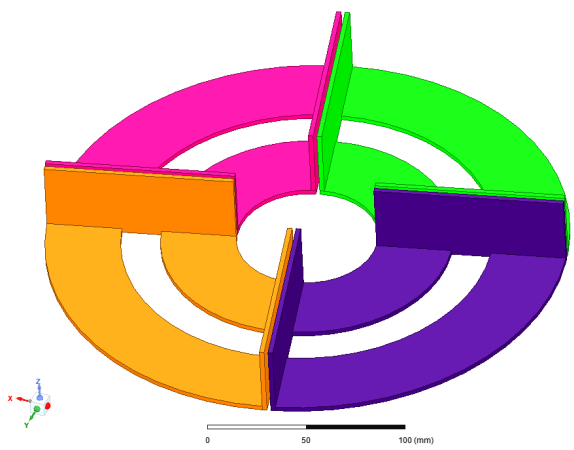
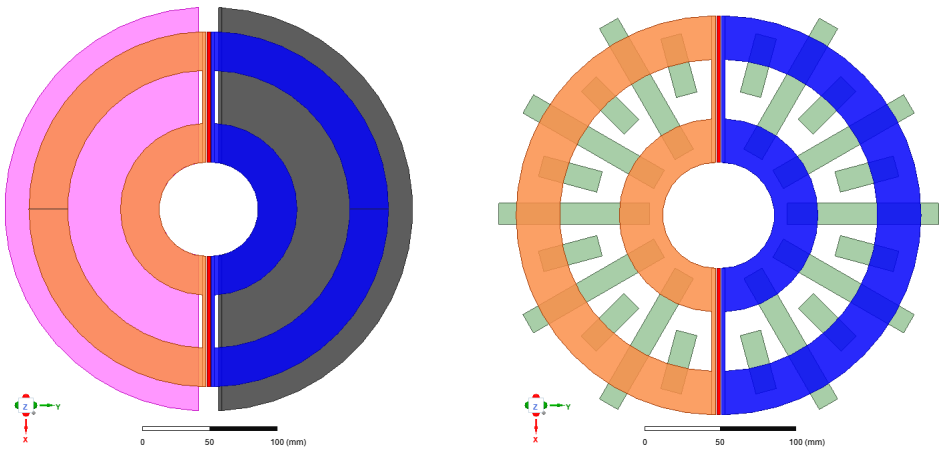


Figure 4.4: Overall Rx side IPT coil systems. (Ferrite back-cores are omitted for visual clarity.)

ity of the IPT coils (presented in Chapter 1) are planar inductors which results in a high inductor area. Although covering a larger area surely results in a higher intrinsic quality factor, the mass and cost of ferrite will also be significantly higher. To reduce the ferrite mass and cost, ferrite spokes are often employed. In Fig. 4.5, Tx coils with full ferrite back-core and ferrite spokes are presented.



(a) Tx coils with complete ferrite back-core

(b) Tx coils with complete ferrite spokes

Figure 4.5: Tx coil with complete ferrite back-core and ferrite spokes.

Both of these IPT coils are modeled in ANSYS Maxwell environment, and for the same geometries, the inductances are found as 80.94 μH and 65.4 μH for complete ferrite back-core and ferrite spokes, respectively. In the simulation, the airgap is given as 30 mm, and the Rx coils have complete ferrite back-cores. The complete back-core has an inner diameter of 70 mm and an outer diameter of 280 mm. Complete ferrite back-core and ferrite spokes have an area of 669 cm^2 and 207 cm^2, which results in 69% ferrite mass reduction for an inductance difference of nearly 20%. The Tx coil with a complete ferrite back-core has 13 turns. Increasing this number to 14 for Tx coil with ferrite spokes results in 78 μH.

4.1.4 IPT Coil System FEA Results and Setup

The Tx coils are designed such that the desired inductances are achieved with a nearly uniform radial airgap flux density. During the Rx coil design, the end windings are curved upwards to achieve both the coil inductance and the required cross-coupling.

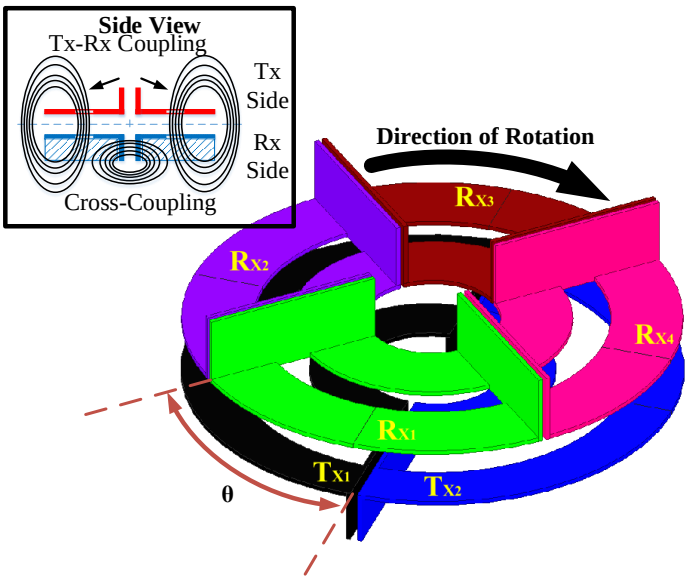
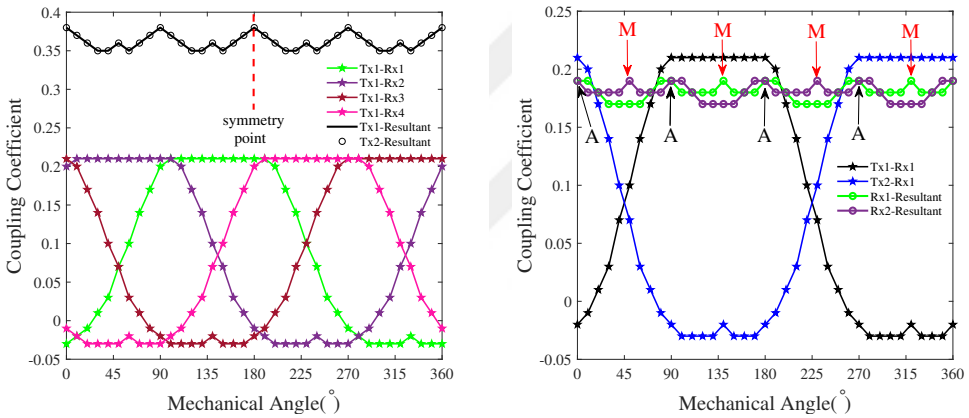


Figure 4.6: Overall IPT coil systems. (Ferrite back-cores are omitted for visual clarity.)

From Fig. 4.3, it is clear that the bent end winding Tx coil geometry is superior in terms of uniform radial B-field, which is crucial for a better Rx module power distribution. The overall IPT coil system is given in Fig. 4.6. The coupling of the Tx coils and two adjacent Rx coils are given in Fig. 4.7. For no axial misalignment, the couplings of the Tx modules are equal. This also means that the reflected impedances are equal, which results in equal Tx currents. "A" and "M" for the Rx coils stand for aligned and misaligned positions, respectively. In Chapter 3, 5% coupling difference was assumed, but until now, an explanation was missing. For the misaligned condition in Fig. 4.7, there exists a maximum of 5% coupling difference for the two adjacent Rx coils. The manufactured IPT coils are presented in Fig. 4.8. The FEA and experimental setup IPT inductance comparison is performed in Table 4.2 where the fully-aligned and misaligned conditions are taken from Fig 4.7.



(a) Coupling of a transmitter with respect to full rotation.

(b) Coupling of two adjacent receivers with respect to full rotation.

Figure 4.7: Tx and Rx coil couplings for a complete rotation.



(a) Manufactured Tx side IPT coil.

(b) Manufactured Rx side IPT coil.

Figure 4.8: Manufacured Tx and Rx side IPT coils.(Rx side ferrites are omitted for visual clarity.)

Table 4.2: Comparison of Inductance Values Obtained from Experimental Results and FEA Simulations

	Experiment(μH)		**FEA**(μH)	
	Fully-Aligned	**Misaligned**	**Fully-Aligned**	**Misaligned**
L_{Tx}	83.5	83.5	80.95	80.95
L_{Rx1}	65.5	65.6	63.7	63.7
L_{Rx2}	65.4	65.4	63.7	63.7
M_1	13.9	12.3	15.86	13.71
M_2	14.5	15.2	15.86	16.9
M_s	-10.7	-10.7	-9.1	-9.1

4.2 Tx Side Full Bridge Converter Design

In Table 3.2, the rated power is given as 1 kW, which results in 500 W on each Tx module. However, the analytical values were calculated under 100% efficiency, which is not realistic. In the literature [19, 23, 46], the IPT system efficiencies were given between 80% to 95%, depending on the system requirements. In this study, the full bridge converters are designed to have 650 W as their rated power under $100\ V_{DC}$ input voltage. Which results in 6.5 A drawn from the supply for each Tx module.

4.2.1 Half Bridge Design

During IPT operation, the ZVS is achieved during MOSFET turn-on. Although this results in significantly smooth switching transients, designing the system to tolerate hard-switching is necessary for safe operation. Even for well-designed converters, hard switching may result in voltage spikes. A common practice is to choose the voltage rating of the semiconductor 1.5-2.5 times the nominal input voltage of the half bridge topology. For resonant frequency operation, the voltage and the current are in phase. The input voltage is given in Table 3.2, as $90\ V_{rms}$ which results in $7.2\ A_{rms}$ per module. Moreover, the selected MOSFET should have low C_{DS} and C_{GS} in order to operate at high frequencies. The selected Si-MOSFET is Infineon Technologies OptiMOS3 BSC600N25NS3G. The rated voltage is 250 V and has a continuous drain current of 16 A. The recommended gate driver for the selected MOSFET is EiceDRIVER 2EDF7275F. It has a 4 A/8 A source/sink current. Although the source/sink current is high for ZVS operation, this selection is made to ensure proper switching under hard-switching conditions. The important parameters of selected MOSFET and gate-driver are given in Table 4.3.

4.2.1.1 Gate-Drive Method and Layout Considerations

Another major challenge under high-frequency operation occurs during hard-switching conditions, which is the false turn-on condition. Although the threshold voltage of

Table 4.3: Finalized System Parameters for 2Tx-4Rx System

MOSFET		**Gate-Driver**	
V_{ds}	250 V	Type	Half-bridge
$I_{D,cont}$	16 A	Source/Sink Current	4 A/8 A
$R_{ds,on}@25°C$	60 mΩ	Isolation	1.5 kV
$R_{ds,on}@80°C$	80 mΩ	Signal Isolation	Yes
t_{rise}	10 ns		
t_{fall}	8 ns		
$t_{off,delay}$	22 ns		
$R_{j,c}$	1 K/W		

the selected MOSFET is around 2 V at $100°C$ junction temperature, during hard-switching, a voltage induced on the gate loop of a non-conducting MOSFET may result in false turn-on during switching transients. To avoid such a false turn-on, the gate is closed and held with negative voltage during off state.

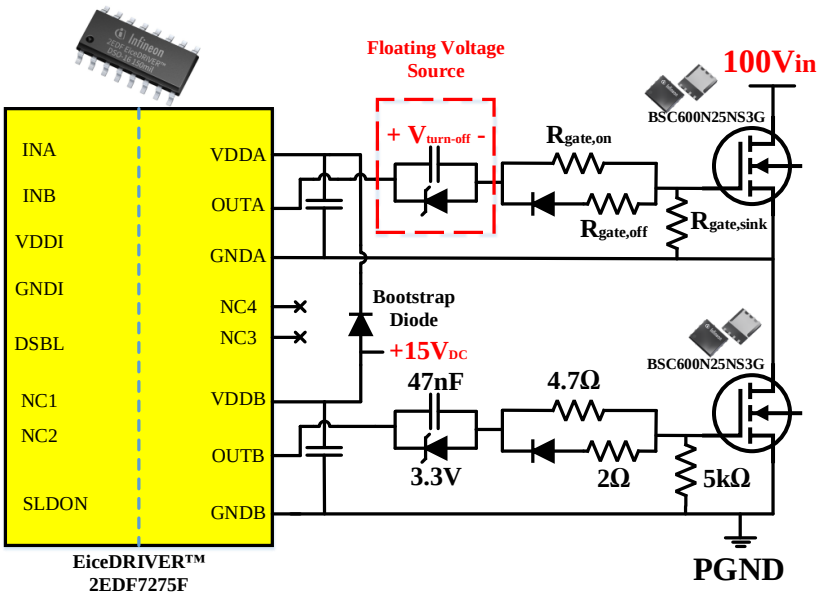


Figure 4.9: Boostrap gate drive method with negative gate turn-off capability.

Texas instruments suggest three different negative turn-off gate drive topologies in [47]. The selected gate drive topology is a negative turn-off with bootstrap method given as in Fig. 4.9. The addition of an extra zener diode and parallel-connected capacitor results in a floating voltage supply. During turn-on, the capacitor is charged until the zener voltage. This floating supply is used during turn-off where the V_{gs} is held at slightly lower than $-V_z$. In Fig. 4.9, 15 V is selected as the gate turn-on voltage. Since the zener diode has a zener voltage of $3.3\,V$, the turn on voltage applied to the gate drops to 12.7 V and the turn-off voltage is slightly lower than $-3.3\,V$. This method is considered the simplest and smallest method to achieve negative turn-off. However, a downside of this method is its duty-cycle limitation. If the mean voltage of the supplied gate signal is lower than V_z, the desired negative turn-off voltage may not be achieved. Therefore, this method is more suited to constant duty cycle operations like frequency or phase control. The PCB layout is realized in Altium Designer. The turn-on and off gate loops for a single MOSFET are given in Fig. 4.10.

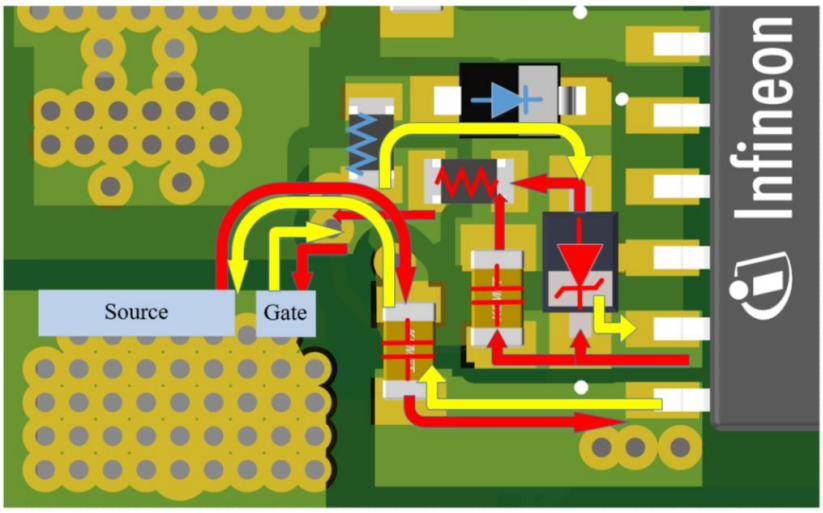


Figure 4.10: Gate turn-on/off loops for a single MOSFET.(red: turn-on, yellow:turn-off)

4.2.1.2 Thermal Management

Thermal management of the overall system is an important issue that requires special attention. The MOSFET thermal loss components can be divided into two parts which

are the conduction and switching losses. The conduction losses can be calculated using the RMS current on the semiconductor and the $R_{ds,on}$ resistance. According to the datasheet of BSC600N25NS3G MOSFET, the $R_{ds,on}$ resistance at 12.7 V as gate voltage for $80°C$ junction temperature is around $80\ m\Omega$. The sinusoidal line current rms is taken as 7.2 A_{rms}. Each MOSFET is under conduction for half a sine cycle. The rms of the half-wave sine wave is 5 A_{rms}. The conduction loss of each MOSFET can be calculated as in (4.2).

$$P_{conduction} = R_{ds,on} I_{ds,rms}^2 = 80 \times 10^{-3} \times 25 = 2\ W \tag{4.2}$$

Switching losses on a MOSFET can also be divided into two parts which are turn on and off losses. Since ZVS is achieved under normal operation, turn-on losses are negligibly small. The turn-off power loss is given in Fig. 4.3. In the datasheet, the fall delay time and fall time are given as 22 ns and 8 ns, respectively. Each MOSFET is subject to 100V during turn-off. The subjected voltage is not trivial since it is directly related to the power factor. When the operation is close to the resonant frequency, the turn-off current is close to zero-crossing of the sine wave. When operation shifts further into the inductive region, the current at turn-off is close to the peak current. However, since the power transfer decreases, the current peak also decreases. Therefore, for simplicity 2.5 A is taken. During calculation, the average voltage is taken as the half of the rated voltage due to its triangular rise shape, which results in 2.5 W loss per MOSFET during rated operation.

$$P_{turn-off} = f \int_0^{t_{off,delay}+t_{fall}} V_{ds}(t) I_{ds}(t)\, dt = 150 \times 30 \times 2.5 \times 50 \times 10^{-6} = 0.56\ W \tag{4.3}$$

The thermal model is given in Fig. 4.11. The losses of each MOSFET is modelled as current sources. The junction to case thermal resistance R_{j-c} is given as 1 K/W.

The selected MOSFET (BSC600N25NS3G) is a bottom cooled device. Therefore, the MOSFET and the heatsink are on the opposite sides of the PCB. The thermal interface achieved using thermal vias. In [48], the calculation of the thermal resistance is given as in (4.4). N is the number of vias, $\lambda_{CU} = 4W/cmK$, $Length$ is 1.6 mm, $radius = 0.1524\ mm$ and $plate\ thickness = 0.0035\ cm \times OZ_{CU}$. In the PCB

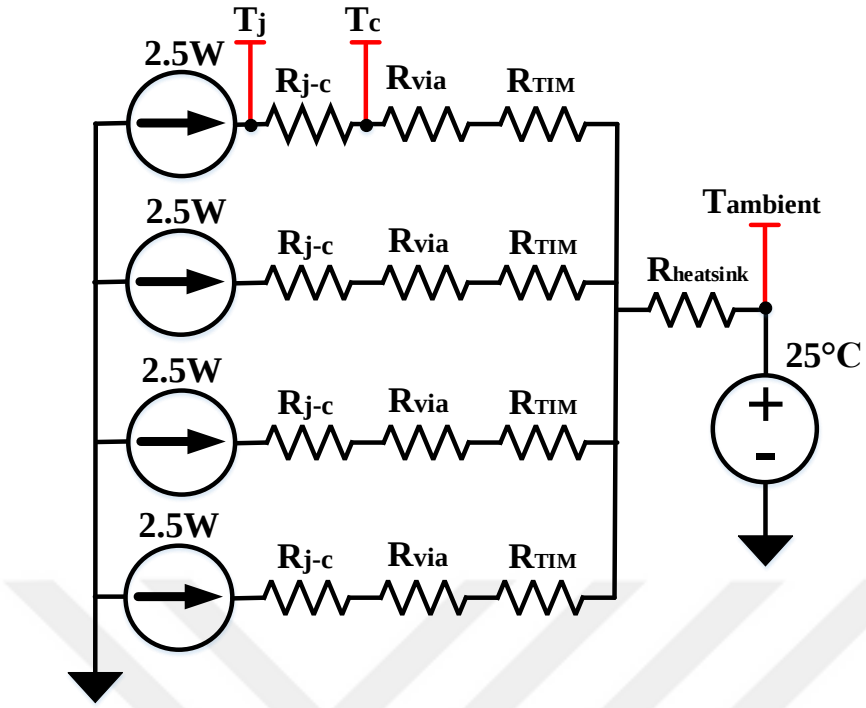


Figure 4.11: Thermal model of the full bridge converter.

layout, there are 45 vias per MOSFET, the vias have 0.1524 cm radius, and we have a total of 7 oz copper. The thermal resistance of thermal via interface is found as $R_{VIA} = 1.88K/W$.

$$R_{VIA} = \frac{1}{N} \frac{\frac{1}{\lambda_{CU}} \times Length}{\pi \times [(radius)^2 - (radius - plate\ \ thickness)^2]} = 1.88K/W \quad (4.4)$$

The thermal interface material is necessary to be able to transfer heat from the vias to the heatsink with electrical isolation. The selected thermal pad for each MOSFET has 9 K/W thermal resistance R_{TIM}. Finally, it is possible to select a proper heatsink. An initial assumption was made during the conduction loss calculation is the maximum junction temperature is $80°C$. By placing the thermal resistances to the model in Fig. 4.11, the $R_{heatsink}$ is calculated as 2.5 K/W. This value is unfeasible for a 40x40 mm heatsink for passive cooling option, and hence a fan is required. APF40-40-13CB/A01 has the dimensions of 40x40x12.7 mm and has 2.3 K/W ther-

mal resistance under 200 LPM forced conduction. The heatsink and fan connection are given in Fig. 4.12.

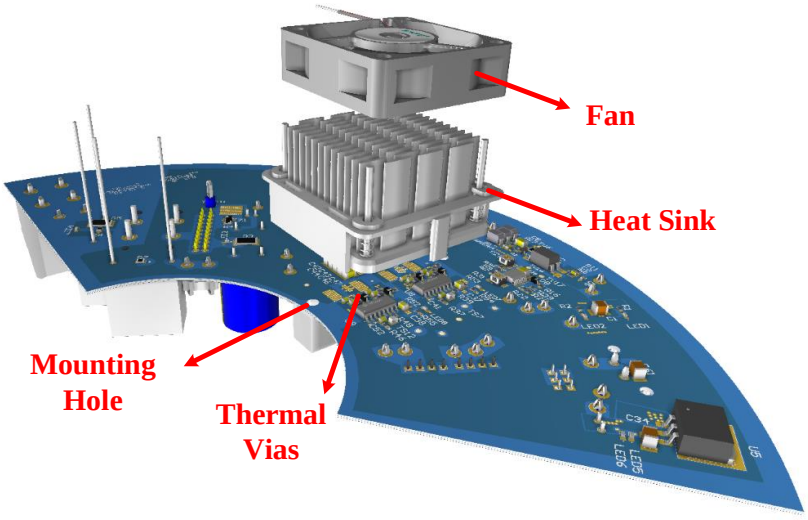


Figure 4.12: Heatsink and fan connection to the PCB.

4.2.2 Over Voltage Protection (OVP)

In series-series IPT systems with a high-quality factor, the voltage across the terminals of the compensation capacitors are often dangerously high, which was previously discussed in detail in Chapter 1. Therefore, over-voltage protection circuitry is necessary for safe operation. The proposed over-voltage protection topology is given in Fig. 4.13.

The OVP circuit is connected between the PGND and the middle of the resonant capacitor and inductor on the Tx side. The three series connected diodes allow one-directional current-flow when the voltage on the resonant capacitor exceeds a certain voltage level which is set by series connected zener diodes. During normal operation, the voltage peaks are in the range of 700-1000 V and this voltage is also on the diodes. Series-connection allows voltage sharing and hence reduces the voltage stress on a single diode. Series connected zener diodes allow flexible OVP voltage level selection. In case of an over-voltage, the V_c node is charged until the upper voltage clamp of 12 V is achieved. If V_c surpasses 4.7 V, the NMOS gate is turned on, which

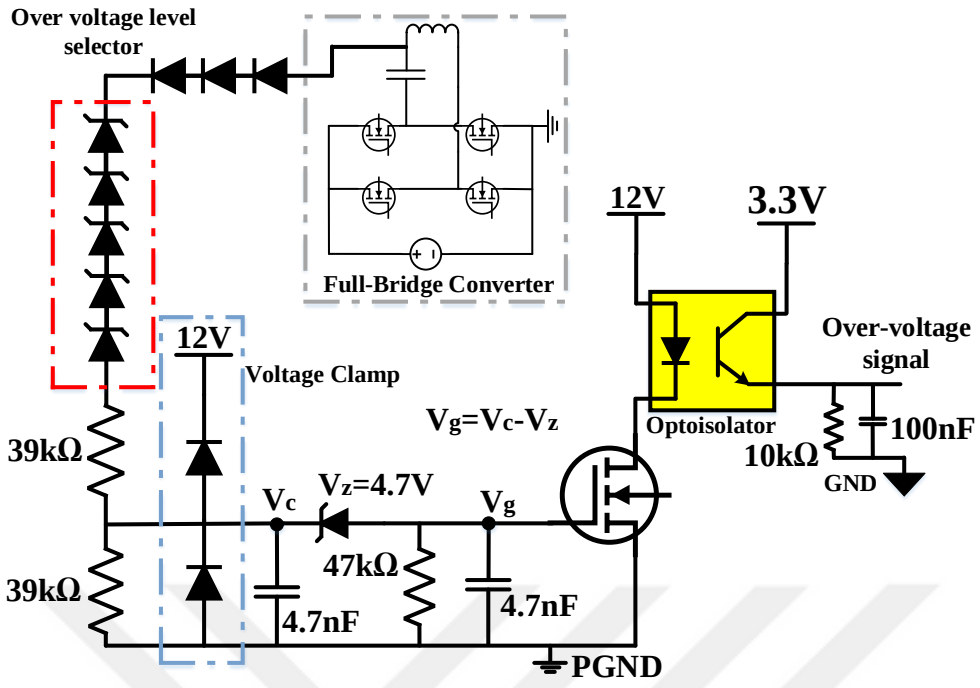


Figure 4.13: Over-voltage protection circuit.

is isolated using a digital opto-coupler and as long as V_c is charged an over-voltage signal is generated in the signal side. The signal is connected to the micro-controller's single event trip-zone interrupt, which activates pull-down on all full-bridge converter gate signals. The OVP circuit is modeled in LT-Spice environment and simulated in Fig. 4.14.

In Fig. 4.14, a 1000 V sinusoidal signal is given as the resonant capacitor voltage. The OVP voltage level is set to 950 V using the series connected zener diodes. With each period, the voltage across the capacitor (V_c), is charged and the output of the opto-coupler (V_{signal}) becomes 3.3 V under four over-voltage cycles. The rise time of the signal is strictly dependent on the capacitance, voltage divider resistors on the OVP circuit, and the output capacitance/resistance of the optocoupler.

4.2.3 Reverse Voltage Polarity Protection

The reverse voltage polarity protection circuit is given in Fig. 4.15. In the figure, the voltage polarity is given in its correct connection. When correctly connected,

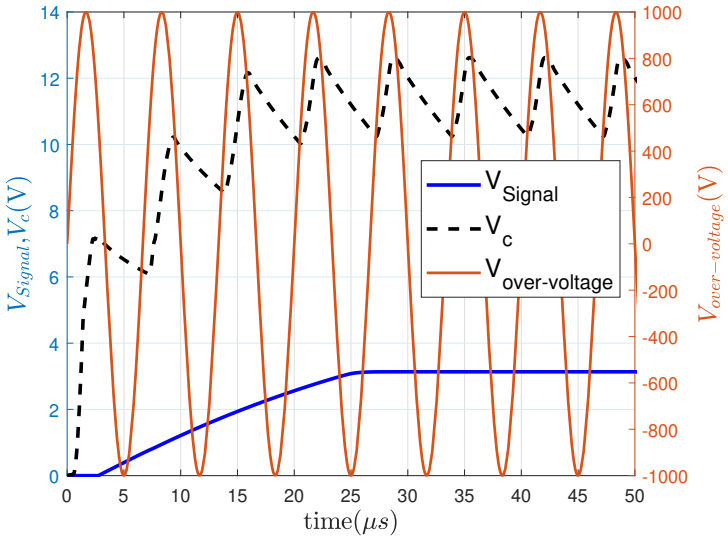


Figure 4.14: Over-voltage protection simulation.

the voltage across the positive side of $V_{in,+}$ and source of MOSFET is equal to V_{in}. Therefore, a current, limited by the gate resistor, flows continuously. The zener diode is used to determine the V_{gs} voltage of the MOSFET. The MOSFET is placed on the return path, and the main current flows from the source to the drain of the MOSFET. When reverse voltage polarity is applied, no gate voltage can be applied to the MOSFET. Therefore, the MOSFET stays off, and the rest of the circuit is also protected.

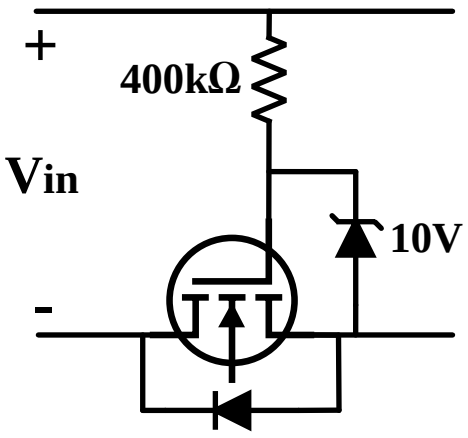


Figure 4.15: Reverse voltage polarity circuit.

An important consideration at this stage is the MOSFET selection. Considering the correct voltage polarity is applied, the MOSFET is turned on and continuously conducts the line current. It also means that the only loss element on the MOSFET is the $R_{ds,on}$ resistance. In the design, the same MOSFET (BSC600N25NS3G) is selected. During testing, reverse voltage polarity protection worked without any problem. However, as the power drawn from the supply increasses, the MOSFET failed in terms of cooling. During the design, a bypass system is also implemented to disable the RVP protection. For low power tests the RVP was enabled while to avoid failure it is disabled as the power level increases. A revision is necessary in the future with a larger MOSFET with a lower $R_{ds,on}$.

4.3 Rx Side Full Bridge Diode Rectifier Design

The induced voltage on the Rx side IPT coil should be rectified at the output. Rx modules should be parallel connected, and they should be mounted around a rotating shaft. The parallel connection can either be made on the PCB or on the load side. However, parallel connection on the load side will interfere with compact design, and hence the parallel connection is achieved on the PCB.

The diodes are chosen as C3D10060G from CREE/WOLFSPEED. The voltage rating is 600 V and has a current rating of 10 A each. The diodes are slightly over-designed since during Rx side open-circuit fault, a power unbalance was observed.

4.3.1 Thermal Management

A similar thermal design given in the full-bridge converter design section is used for the Rx side diode rectifier. According to the datasheet, the forward voltage (V_f) is equal 1.2 V. During conduction, the mean current on a single diode is around 1 A. Therefore, for each diode, there is 1.2 W power dissipation in the form of heat. As for heatsink 908-35-2-23-2-B-0 component from Wakefield-Vette is selected. The junction to case thermal resistance(R_{j-c}) is given as 1.2 K/W. The thermal via ther-

mal resistance is calculated as 0.8 K/W. Using the same thermal model given in Fig. 4.11, the junction temperature(T_j) is found as $75°C$ with natural air convection. In Fig. 4.16, the heatsink, thermal-vias, and common DC-bus connectors are presented.

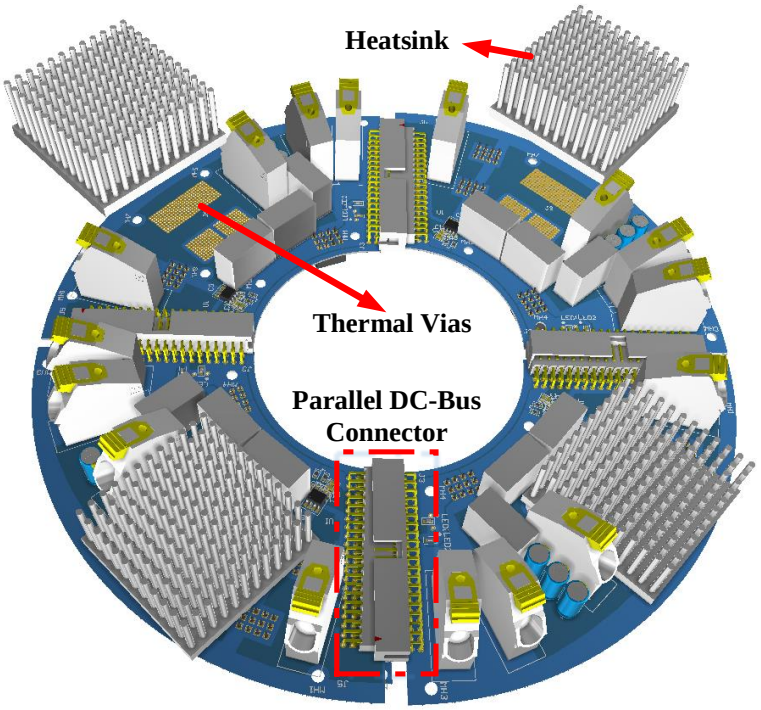


Figure 4.16: Rx side heatsink, thermal-vias and common DC-bus connector.

The finalized Rx modules are given in Fig. 4.17. The resonant capacitors are also mounted on the same PCB with connectors. This way, different resonant capacitors can be easily mounted, and different IPT systems can be tested.

4.4 Summary

In this section, the 2Tx-4Rx IPT experimental setup design is presented. The parameters in Table 3.2 are realized in a physical manner where the IPT coils and Tx and Rx power electronic PCBs are designed.

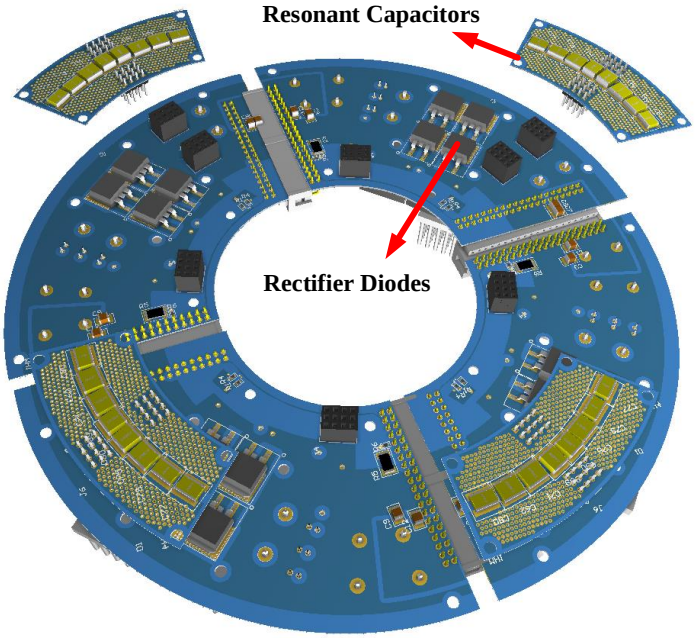


Figure 4.17: Rx side rectifier diodes and resonant capacitor PCB cards.

The IPT coils are designed such that a balanced Rx module power is achieved. Compared to the non-bended IPT coil geometry; a bent geometry is found to be superior in terms of uniform radial B-field distribution. Therefore, the end windings of the Tx coils bent. To reduce Tx side cross-coupling, ferrites are used to achieve magnetic shielding. With a similar geometry, the Rx coil end windings are also bent. However, unlike the Tx coil design, the aim is to control the cross-coupling between the adjacent Rx coils. Moreover, the effect of using ferrite spokes instead of complete ferrite back-core is discussed where nearly 70% ferrite mass is reduced for only 20% reduction in the coil inductance where a slight increase of the Tx side turn can equalize the inductances for the presented ferrite geometries. The finalized geometric parameters of the IPT coil system are presented in Table 4.4.

During Tx side full-bridge converter design, first, the switching semiconductors are selected. Then, the gate-loop is designed where negative turn-off is applied using a floating voltage source composed of a parallel connected zener diode and a capacitor. This method is strictly limited by the duty-cycle. Since, both frequency and phase control methods are realized using constant duty cycle, this method is not

Table 4.4: Finalized IPT Coil System Geometric Parameters

	Tx Coil	Rx Coil
D_{in}(mm)	70	70
D_{out} (mm)	280	280
Coil Angle	180	90
Turns	13	16
Coil Inductance	83.1-83.5	65.6-65.4-66-64.9
Rx side Mutual inductance μH		-10.7
Airgap(mm)	30	
Ferrite	I20x2 N48	

only straight forward but also cheaper than other methods. Then, the reverse voltage polarity protection is explained. Although the method successfully blocked reverse voltage due to thermal failure, this circuit block is bypassed during testing. Finally, the over-voltage protection circuitry is implemented. The over-voltage protection is implemented to protect the resonant capacitors from over-loading, and it also acts as over-current protection since the capacitor voltage is dependent on the capacitor voltage as given in (4.5). Finally, the required heat-sink and cooler fan are selected using the lumped port thermal model.

$$I_c = C\frac{dV_c}{dt} \Longrightarrow \Delta V_c = \frac{1}{C} I_c \Delta t \tag{4.5}$$

With a similar approach, the Rx modules are also connected. The Rx modules are designed such that the full-bridge diode rectifiers can operate under fault conditions; hence they are slightly over-designed. The parallel DC-bus connection is realized using connectors between four Rx modules. Similar to the Tx modules, the Rx side capacitors are placed on an external PCB and connected in series using header connectors such that different IPT systems can be tested with ease.

CHAPTER 5

2TX-4RX IPT SYSTEM SIMULATION AND EXPERIMENTAL RESULTS

The proposed common DC-bus IPT system constists of 2Tx-4Rx modules where the Rx modules are connected in parallel. While, it aims to decrease the semiconductor ratings and increase the fault tolerance of the overall system, the current balancing was a major issue. In Chapter 3, the system is first designed where bifurcation phenomenon is avoided. Later, the current balancing issue was solved using cross-coupling and intentional de-tuning of the Rx side. Simulation results in Fig. 3.9 shows the improvement in current balancing using additional cross-coupling. Similarly, in Fig. 3.10, the effect of Rx side de-tuning shown. Although, the improvement is proven both analytically and using simulation, an experimental verification is still necessary. Therefore, in the first section of this Chapter, the effect of current balancing methods will be presented experimentally both separately and combined.

Secondly, experimental verification of the rotational system is required. Therefore, in the third section of this Chapter, the overall system testing ranging from rotation to faulty mode of operation. The testing is performed using the Tx and Rx coils presented in Fig. 4.8 and the Tx and Rx modules presented in Fig. 4.12 and Fig. 4.16 respectively.

5.1 Experimental Results and Discussion for the Proposed Current Balancing Methods

The 1Tx-2Rx system is presented in Fig. 5.1, where there is a single full-bridge converter, and the other Rx circuits consist of passive diode full-bridge rectifiers con-

nected in parallel to the same load. For the cross-coupled Rx modules, the coupling is set to be $k = -0.15$, and for the detuned Rx side, the resonant frequency of the Rx side is adjusted to 135 kHz. For 1Tx-2Rx experiments, a half-circular structure is used where a slight misalignment between a single Tx and two adjacent Rx modules is given where the maximum ΔM is satisfied, which was previously presented in Fig. 6.1. For 1Tx-2Rx experiments, the output power is set to 500 W, and similarly, for the 2Tx-4Rx case, this number is doubled to 1000 W. For all experiments, the load resistance (R_L) is kept constant. Therefore, keeping the output power constant also means a constant output voltage $V_{out,DC}$. The experimental setup parameters are listed in Table 5.1.

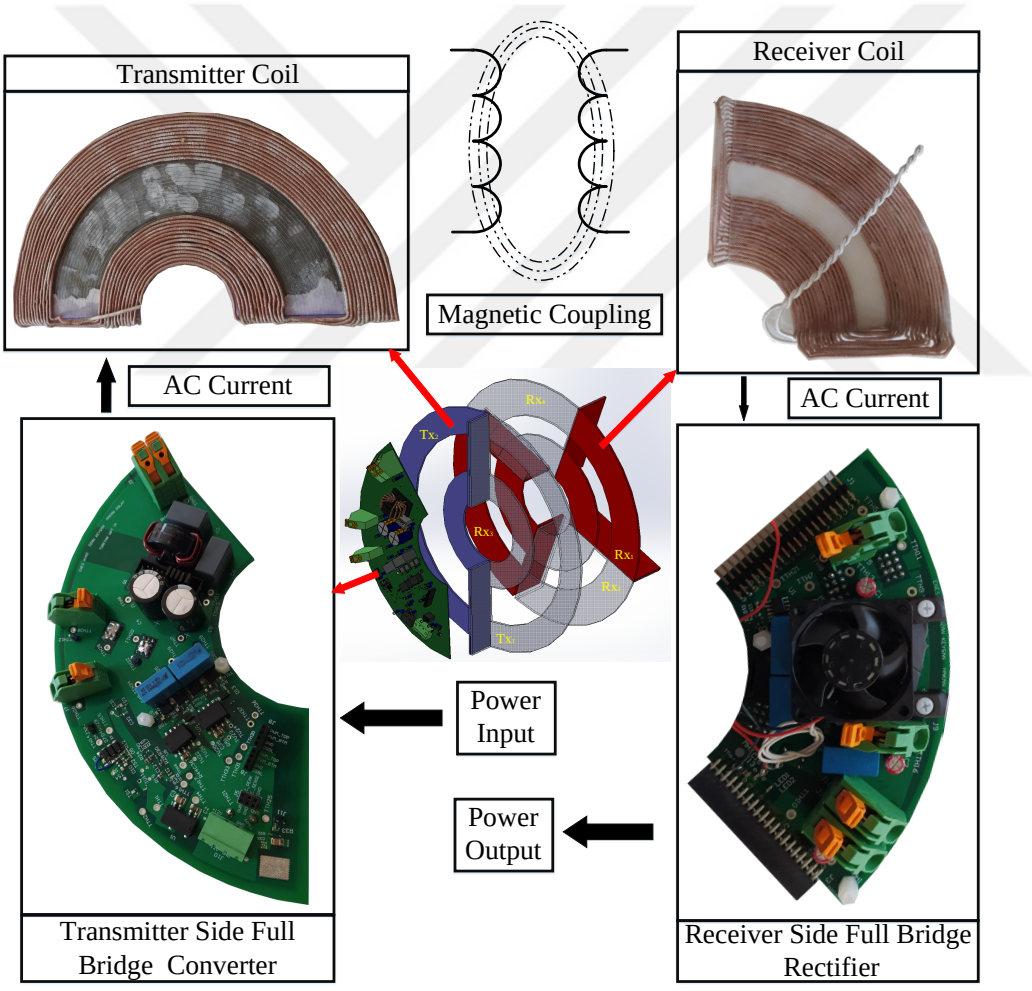


Figure 5.1: Test setup illustration.

Table 5.1: Experimental Setup Parameters

Tx side MOSFET	BSC600N25NS3G	Tx side Gate Driver	2EDF7275F
Rx side Diodes	C3D10060G	Litz Wire	400x0.08mm ($2\ \mathrm{mm}^2$)
Tx coil $\mathrm{D_{in}}$ and $\mathrm{D_{out}}$	70-280 (mm)	Tx coil # of turns	13
Tx coil	83.1-83.5 (μH)	Rx coil $\mathrm{D_{in}}$ and $\mathrm{D_{out}}$	70-280
Rx # of turns	16	Rx inductances	65.6-65.4-66-64.9 (μH)
$\mathrm{M_s}$ (μH)	-10.7	$\mathrm{C_{Tx}}$ (nF)	13.8
$\mathrm{C_{Rx}}$ (nF)	21.1	Airgap (mm)	30
$\mathrm{f_0}$	150 kHz	f	155 kHz

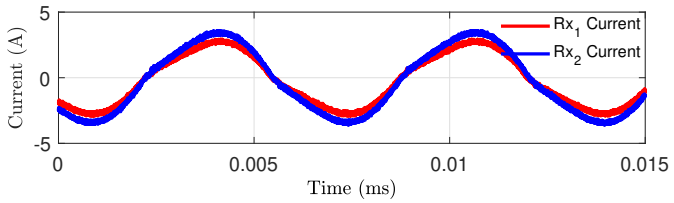
5.1.1 Fully-Aligned Case

The inductance values of the full-aligned system are presented in Table 4.2. Current distributions for decoupled/fully-tuned, decoupled/detuned and coupled/fully-tuned cases are presented in Fig. 5.2. Since the couplings between the Tx and Rx modules are very close, all Rx currents are nearly identical. However, since there exist small coupling and inductance differences current balancing effects of the proposed methods are observable.

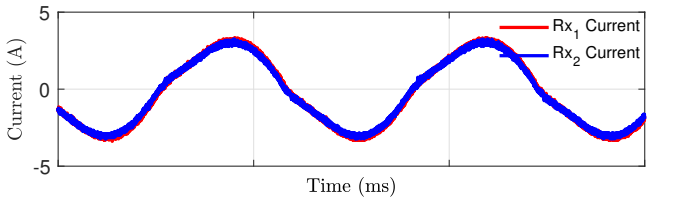
5.1.2 Misaligned Case

The inductance values of the misaligned system are presented in Table 4.2. The current balancing effect comparisons are first done for cross-coupling effect and detuning and finally for the combined balancing methods.

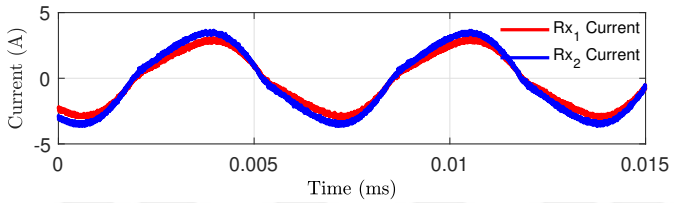
In Fig. 5.3-b, the effect of cross-coupling for fully-tuned Rx side is presented. In Fig. 5.3-c, the effect of detuning for no cross-coupling is presented. In Fig. 5.3-d, the combined current balancing effect of cross-coupled and detuned Rx modules is presented.



(a) 150 kHz Decoupled Receivers ($I_{Rx1} = 1.9A_{rms}, I_{Rx2} = 2.4A_{rms}$)



(b) 135 kHz Decoupled Receivers ($I_{Rx1} = 2.2A_{rms}, I_{Rx2} = 2.1A_{rms}$)



(c) 150 kHz Cross-Coupled Receivers ($I_{Rx1} = 2.0A_{rms}, I_{Rx2} = 2.4A_{rms}$)

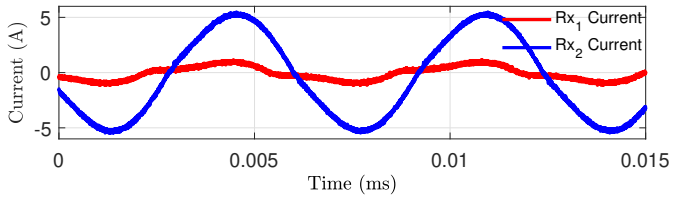
Figure 5.2: Rx current waveforms for fully-aligned case and different current balancing methods.

5.2 Discussion

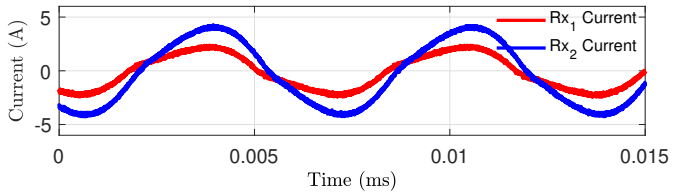
In this section, firstly the experimental results will be discussed. Then the gain plots of the proposed methods will be presented. Let us define a current balance ratio (CBR) as in (5.1).

$$\mathrm{CBR}(\%) = 100(1 - \frac{|\mathrm{I_{Rx1}} - \mathrm{I_{Rx2}}|}{\mathrm{I_{total}}}) \tag{5.1}$$

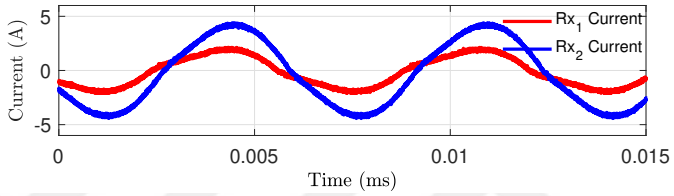
When each Rx module currents are equal, CBR is 100%. Experiment results are presented in Table 5.2 and the effect of current balancing methods are included. As shown in Table 5.2, there is 55.8% improvement in the current sharing compared to the de-coupled and fully-tuned case. The Rx side coil AC resistance was measured as 0.3 Ω. The total Rx side coil ohmic loss was also given in Table 5.2. Although the output power is kept constant for each experiment, the Rx side coil ohmic losses increases as the system becomes unbalanced due to an increased sum of $I_{Rx,1}^2 R +$



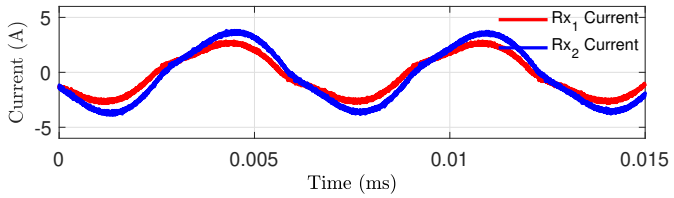
(a) 150 kHz Decoupled Receivers ($I_{Rx1} = 0.6A_{rms}, I_{Rx2} = 3.7A_{rms}$)



(b) 150 kHz Cross-Coupled Receivers ($I_{Rx1} = 1.5A_{rms}, I_{Rx2} = 2.8A_{rms}$)



(c) 135 kHz Decoupled Receivers ($I_{Rx1} = 1.3A_{rms}, I_{Rx2} = 2.9A_{rms}$)



(d) 135 kHz Cross-Coupled Receivers ($I_{Rx1} = 1.8A_{rms}, I_{Rx2} = 2.5A_{rms}$)

Figure 5.3: Effects of cross-coupling and detuning on the Rx side current distribution for the missaligned case.

$I_{Rx,2}^2R + I_{Rx,3}^2R + I_{Rx,4}^2R$. The same is valid for Rx side rectifier diodes conduction losses.

Another critical issue is the variation of the overall system gain characteristics when cross-coupling and Rx side de-tuning methods are introduced. In Fig. 5.4, the gain characteristics for different current balancing methods are presented under fully-aligned position. The initial system design resonant frequency was selected as 150 kHz as in Table 3.1. As we introduce a negative cross-coupling, the peak of gain plots

Table 5.2: Current Sharing for Missaligned Different Balancing Methods and Improvements

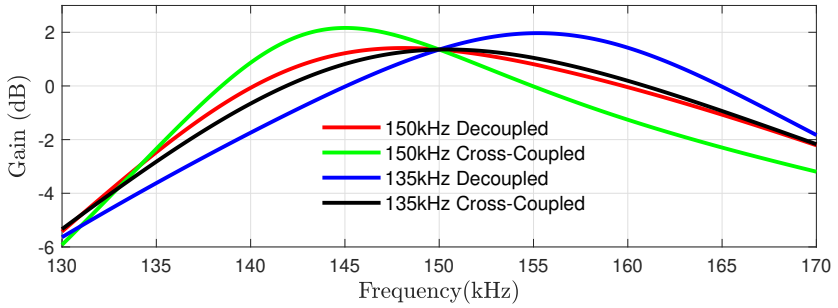
	Decoupled Rx Fully Tuned	**Cross-Coupled Rx Fully Tuned**	**Decoupled Rx De-tuned**	**Cross-Coupled Rx De-tuned**
Rx-1 Current	0.6 (A_{rms})	1.5 (A_{rms})	1.3 (A_{rms})	1.8 (A_{rms})
Rx-2 Current	3.7 (A_{rms})	2.8 (A_{rms})	2.9 (A_{rms})	2.5 (A_{rms})
Rx Copper Loss	4.21 (W)	3.03 (W)	3.05 (W)	2.85 (W)
CBR	27.9 (%)	69.7 (%)	61.9 (%)	83.7 (%)
Improvement		41.8 (%)	34 (%)	55.8 (%)

shifts to lower frequencies. The increase in the gain at the resonant frequency is expected as the Rx coils also induces an EMF component on each other, which further increases the output voltage as previously discussed in Fig. 3.7. De-tuning the Rx modules such that the resonant frequency is lower shifts the gain plot to higher frequencies. This is due to the reflected impedance of the Rx side to the Tx side. The reflected impedance can be expressed as in (5.2).

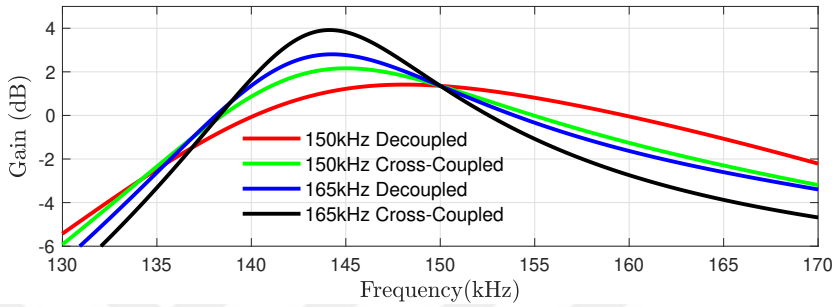
$$Z_r = \frac{\omega^2 M_1^2}{R_{equ,1} + j\omega L_{Rx} + \frac{1}{j\omega C_{Rx}}} + \frac{\omega^2 M_2^2}{R_{equ,2} + j\omega L_{Rx} + \frac{1}{j\omega C_{Rx}}} \tag{5.2}$$

Decreasing the Rx side resonant frequency may have the same effect as increasing the series capacitor. With a higher Rx side capacitance, a higher frequency is needed for the resonance. A similar statement can be made for the opposite case where the Rx side resonant frequency is adjusted higher than the resonant frequency of the Tx side. In this case, the resonant frequency decreases.

During the overall system design, a maximum allowable current balance ratio(CBR) of 82% was selected. Using the analytical model presented in the fourth section, resulted in either positive or negative cross-coupling with a magnitude of minimum of 0.15. The addition of negative cross-coupling is achieved by an up-curvature IPT coil design as given in Fig. 6.1-a. By controlling area of the curvature of two Rx coil, the cross-coupling can be adjusted without a significant change in the self inductance. To further balance the currents, 135 kHz is selected as Rx side resonant frequency while the Tx side is adjusted to 150 kHz. Compared to the initial design given in Fig. 5.4 (150 kHz Decoupled), the gain characteristics of the finalized design is nearly the same.



(a)



(b)

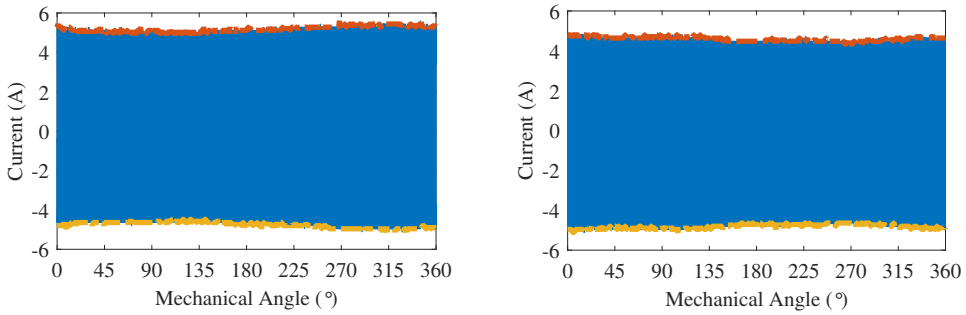
Figure 5.4: $\frac{V_{out}}{V_{in}}$ gain plots for different current balancing methods.

5.3 2Tx-4Rx Rotational System Experimental Results and Discussion

The overall resonant frequency of the proposed system is 150kHz. The rated rotational speed is $1500\ rpm = 25\ Hz$. This means that for one full rotation there are 6000 gate switchings. Therefore, the system can be assumed to be stationary regardless of the rotational speed of the Rx side.

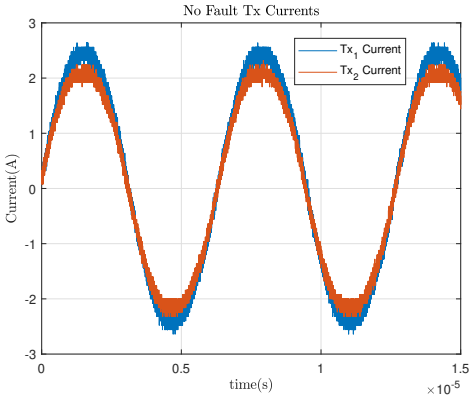
Firstly the Rx side is rotated a complete turn and the time scale is adjusted such that whole rotation is presented with an envelope as shown in Fig. 5.5 where the Tx currents are equal and nearly constant regardless of the angle of the Rx side. This means that the reflected impedance to the Tx side is almost the same. Both currents lags the Tx input voltages which means that ZVS is achieved throughout the rotation.

In Fig. 5.4, the gain plot of the proposed system was given. The operating frequency of the system was swept from 120 kHz to 180 kHz to achieve the gain plot of the experimental setup. Experimental data points are taken at low power since loss of



(a) Tx_1 current

(b) Tx_2 current



(c) Zoomed view of the presented Tx current envelopes

Figure 5.5: Tx side current for a complete rotation.

ZVS operation below resonant frequency increases the thermal stress on the Tx side semiconductors. In Fig. 5.6 an acceptable agreement between the simulated and experimental gain plots can be seen. At higher frequencies, a much higher current is present during the dead-times. Therefore, not only the $\mathrm{C_{DS}}$ parasitic capacitance is drained but also the body diodes goes into conduction for a higher time. Therefore, a higher switching loss is present which can be the reason behind the difference in experimental and simulated gain plots for higher frequencies.

Another challenge is the current balancing of the Rx side modules. Unbalanced power transfer not only results in higher semiconductor stress but also lower efficiency. The current balancing methods were previously discussed in [49]. In order to show the current distribution, the Rx side module currents for a full rotation are given in Fig. 5.7.

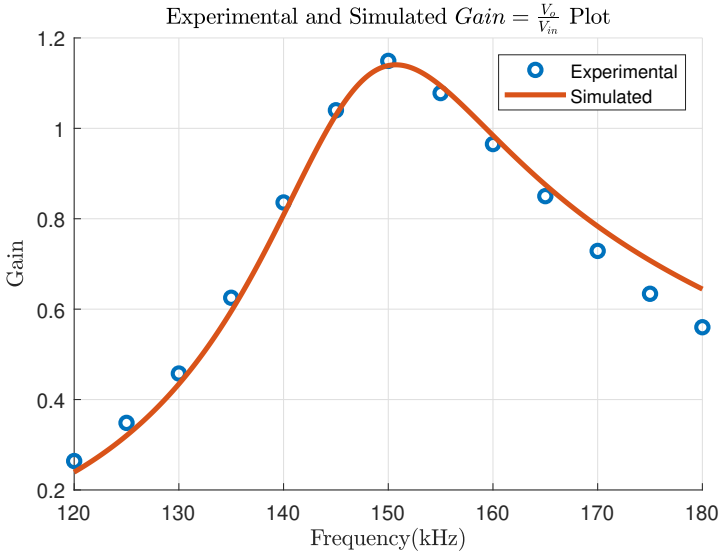


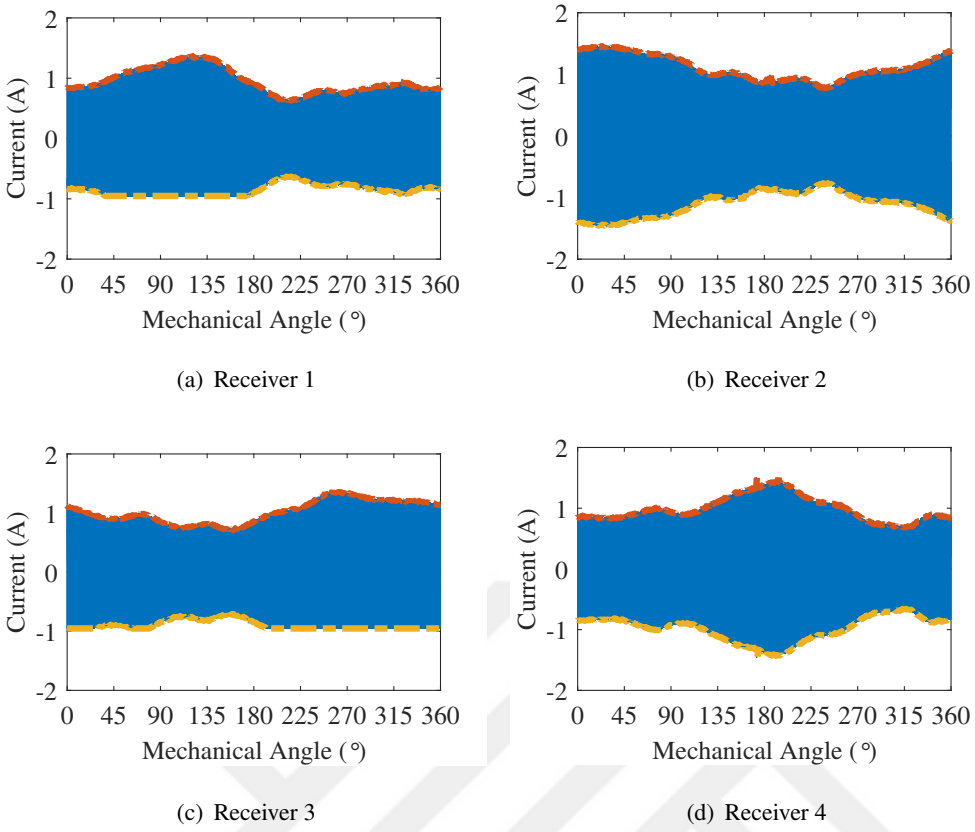
Figure 5.6: Comparison of simulated and experimental gain plots of the test setup. The gain plot is taken for normal operation without any faulty condition. Since uniform radial B-field is achieved usign the proposed coil geometry, the gain plot is constant for different Tx-Rx positions.

The system is tested for different power outputs and the efficiency curve is presented in Fig. 5.8. During testing the Rx side is adjusted as fully-aligned and operating frequency is set to 154 kHz. For 1 kW power output, the thermal images of the test setup is given in Fig. 5.9.

5.3.1 Operation Under Fault

The main idea behind having modular structure for a common DC-bus parallel connected Rx modules is to increase the reliability. In conventional SS topology, open circuited Rx side results in dangerously high Tx currents and having multiple Rx modules coupled with a single Tx module increases the fault tolerance to open circuit Rx side fault conditions.

To verify modularity of the system, a single Rx module was open circuited. For single Rx side fault condition, the reflected impedances at the Tx side are not balanced. Therefore, power balancing of the Tx modules is not achieved. The switching



(a) Receiver 1

(b) Receiver 2

(c) Receiver 3

(d) Receiver 4

Figure 5.7: Rx module current waveforms for a full rotation.

frequency is set to be 156 kHz and a full rotation is made. The normalized power sharing is given in Fig. 5.10 and Fig. 5.11.

Depending on the position the Rx modules, the power sharing changes. Therefore, a best and worst alignment cases are selected. The best alignment is when the faulty module has equal magnetic coupling with both of the Tx modules and the worst alignment is when the faulty module has its maximum coupling with a single Tx module.

5.4 Summary

In this Chapter, experimental results of 2Tx-4Rx system is presented. Firstly, the system is tested for 1Tx-2Rx system to experimentally validate the effect of additional cross-coupling and intentional detuning of the Rx side on the Rx module current sharing. As stated in Table 5.2, the combined effect of cross-coupling and detuning

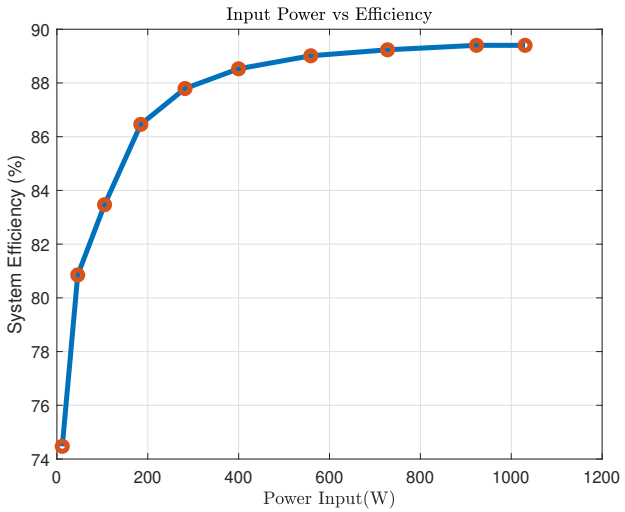
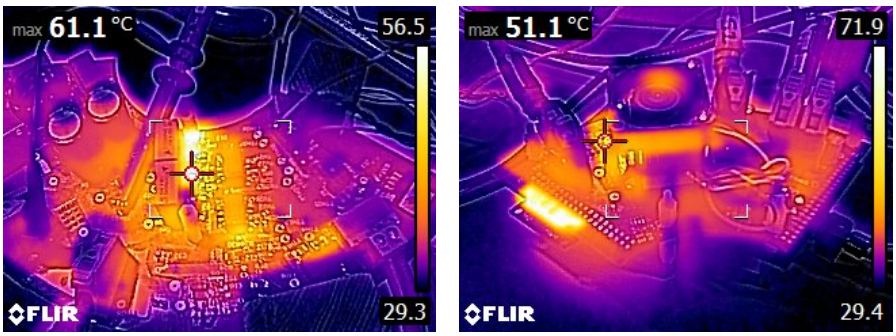


Figure 5.8: Efficiency for different power inputs. The experiment was performed for normal operation without faulty condition.

yields an increase of 55.8% in the Rx side current balancing. The system resulted in 89.7% in efficiency at rated power. Also the experimental and simulated gain plots are compared and an acceptable agreement has been seen. Later, the system is tested for a complete rotation where the Tx currents are found to be equal and constant throughout the rotation as given in Fig. 5.5. Rx currents are also presented in Fig 5.7. Throughout, the rotation, the maximum limit of 50% current difference is achieved. However, for the faulty mode of operation both Tx and Rx currents are significantly unbalanced. Therefore, equal power sharing during fault conditions is still problematic and requires further attention.



(a) Transmitter (b) Receiver

Figure 5.9: Thermal images of Tx and Rx PCB's for rated power output. The maximum temperature at the Tx is $61.1°C$ and $51.1°C$ at the receiver.

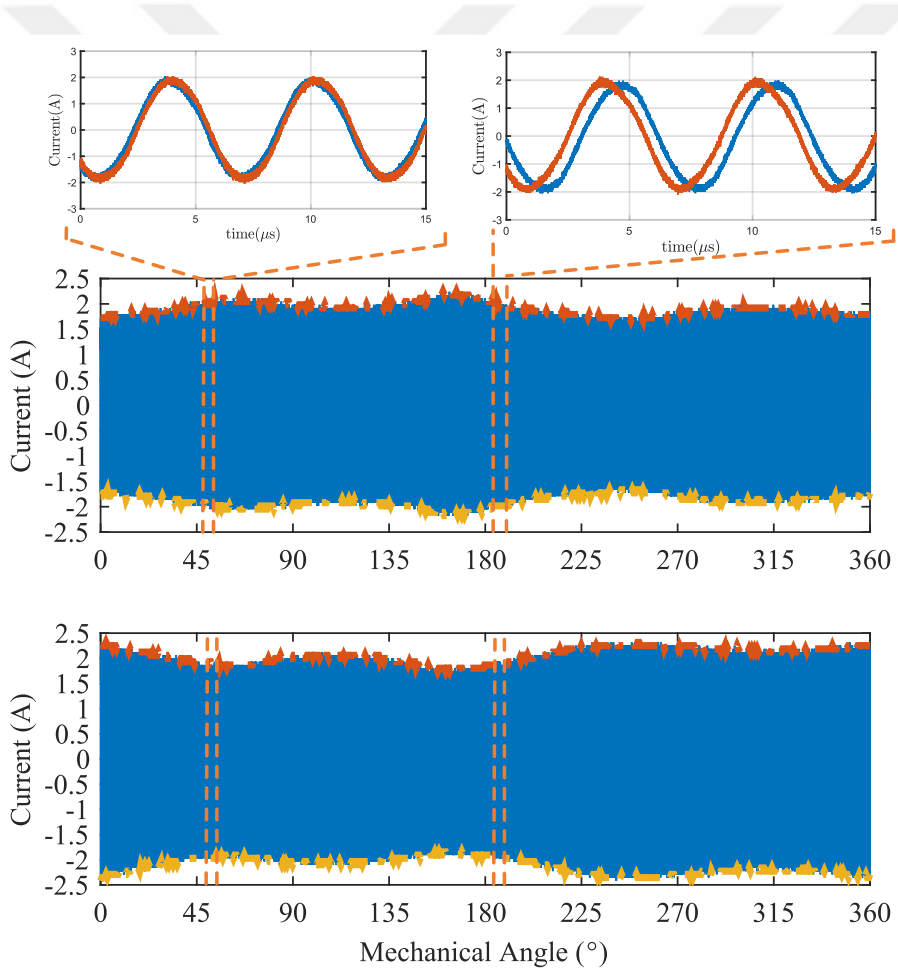
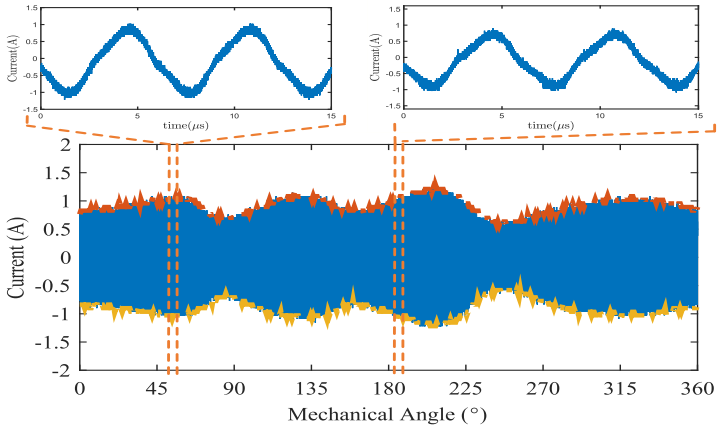
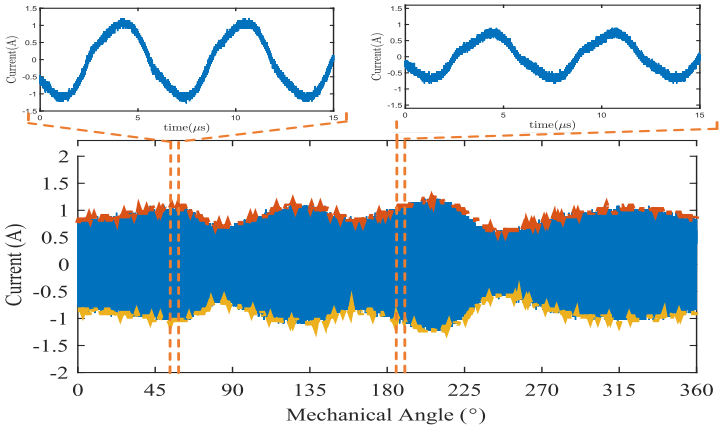


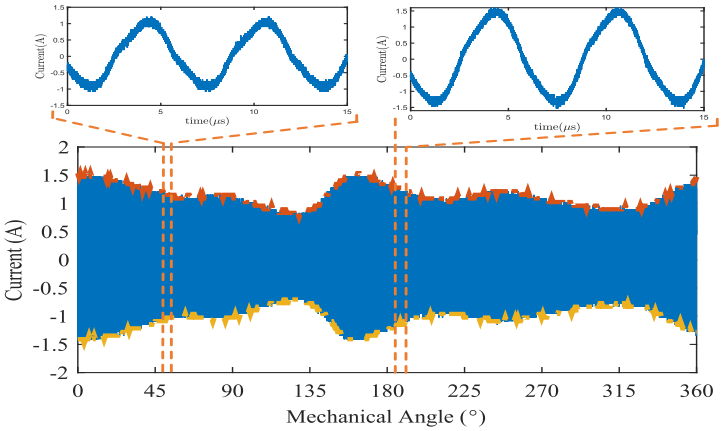
Figure 5.10: Tx current envelope for a complete rotation. The Rx-4 module is open-circuited to investigate faulty mode of operation.



(a) Current of the first receiver for a complete rotation.



(b) Current of the second receiver for a complete rotation.



(c) Current of the third receiver for a complete rotation.

Figure 5.11: Rx current envelope for a complete rotation. The Rx-4 module is open-circuited to investigate faulty mode of operation.

CHAPTER 6

DESIGN AND TESTING OF 2TX-4RX SYSTEM WITH MIDDLE STAGE RESONATOR

Until this point, a modular common DC-bus connected series-series compensated IPT system was presented. Using the current balancing methods proposed in Chapter 3, a modular system with improved fault tolerance is achieved, current unbalances were observed under fault mode of operation as given in Fig. 5.11. While, operation under fault is in safe region of the power converters, long period of faulty operation will surely induce other problems and hence it cannot be sustained. Similar to current unbalance issue under normal operation, again the unbalance under faulty mode originates from unequal magnetic coupling between the Tx and Rx coils. Due to parallel connection, module with higher coupling has the highest power delivery. Under faulty operation, the heat stress on the modules may be equal due to thermal time constant compared with rotation however, this strictly contradicts the wide speed range operation.

The solution is to eliminate the coupling between the Tx and Rx coils completely where the power delivery is achieved by a middle stage resonator. Since, there is only a single circular resonator coil, the coupling between the resonator and the Rx coils are equal for all angles and rotational speeds. The same is also true for the magnetic coupling between the Tx and resonator coils.

This Chapter proposes the addition of middle stage resonator to 2Tx-4Rx where equal Rx module power-sharing is achieved under various open-circuit fault conditions. Moreover, in this Chapter, a conventional bifurcation free series-series IPT system

design given in [42] is extended to be applicable to systems with middle stage resonators. The proposed 2Tx-4Rx system with middle stage resonator is presented in Fig. 6.1. The power is transferred from a stationary Tx side to a rotating resonator and rotating Rx modules.

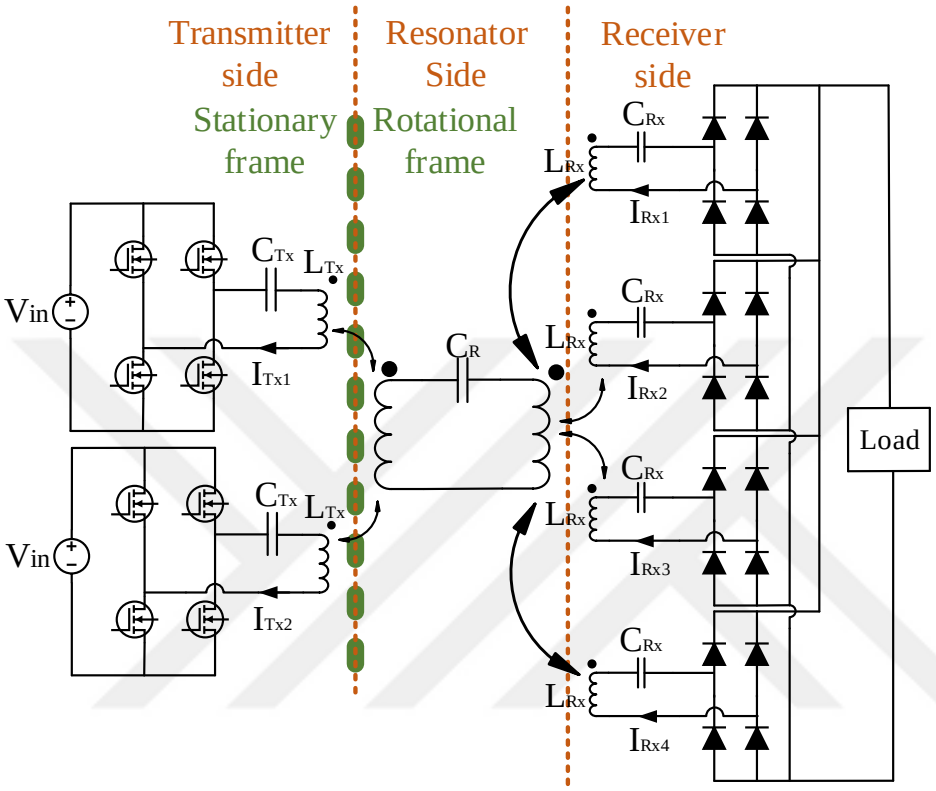


Figure 6.1: The proposed 2Tx-4Rx system with resonator circuit.

The advantages of adding a middle stage resonator coil may be listed as follows:

- Regardless of the current phase and magnitude of the Tx coils, a single sinusoidal current passes through the resonator coil, which allows flexible control over the power transfer.
- The sinusoidal current of the resonator creates a constant magnetic flux density, which results in equal coupling between each Rx module and the resonator.
- In case of an open circuit fault in the Rx side, the air gap flux distribution is not disturbed, and hence the coupling between all Rx modules and the resonator

coil stays constant. Therefore, normal operation can still be achieved naturally without any complex control techniques. A similar statement can also be made for open-circuited Tx fault where power can still be delivered through a single Tx module.

6.1 Design Methodology

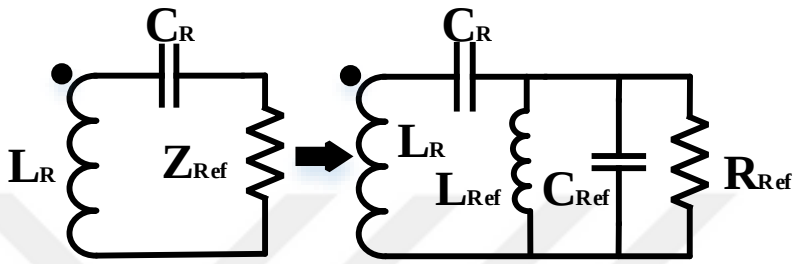


Figure 6.2: Reflected impedance from Rx side to resonator side.

The proposed system structure is presented in Fig. 6.1. It consists of 2 Tx and 4 Rx modules. In the proposed system, the Tx and Rx side are decoupled. The power is transferred with a resonator coil placed between the Tx and Rx coils.

The reflected impedance model from Rx side to resonator side is presented in Fig. 6.2. The reflected impedance Z_{ref} is given in (6.1).

$$Z_{ref} = \frac{\omega^2 M_{R,Rx}^2}{j\omega L_{Rx} + \dfrac{1}{j\omega C_{Rx}} + R_L} \tag{6.1}$$

The reflected parallel resonance circuit impedance can be written as in (6.2).

$$Z_{ref} = \frac{1}{\dfrac{1}{j\omega L_{ref}} + j\omega C_{ref} + \dfrac{1}{R_{ref}}} \tag{6.2}$$

By using (6.1) and (6.2) L_{ref}, C_{ref} and R_{ref} can be found as in (6.3) where $\Phi = \omega^2 M_{R,Rx}^2$.

$$L_{ref} = \Phi C_{Rx}, C_{ref} = \frac{L_{Rx}}{\Phi}, R_{ref} = \frac{\Phi}{R_L} \tag{6.3}$$

The parallel resonant impedance $L_{ref} \parallel C_{ref}$ acts as an open circuit at the vicinity of the resonant frequency. However, it is beneficial to have a low-quality factor at

the parallel resonant circuit since an open-circuited $L_{ref} \parallel C_{ref}$ results in a single resistive component, and the circuit can be reduced to a conventional SS topology. To achieve a low-quality factor at the parallel reflected resonant circuit, L_{ref} should be high, which means that C_{Rx} should also be selected high. The quality factor of the Rx side (Q_{Rx}) is given in (6.4). The internal resistance of the Rx side IPT coil is neglected since it is often negligibly smaller than the load resistance.

$$Q_{Rx} = \frac{\omega L_{Rx}}{R_L} = \frac{1}{\omega C_{Rx} R_L} \tag{6.4}$$

From (6.4), it can be derived that the Q_{Rx} should be selected low, which means a lower inductance value should be selected for the Rx side. However, a very low Q_{Rx} is not desired since it increases the required inductance of the resonator and its size. A low quality factor can be compensated by increasing the coupling between the Rx and resonator coils. However, for some applications increasing the coupling may not always be feasible.

The analysis so far shows that under low Q_{Rx} condition, conventional series-series design methods can be used. Aditya *et al.* proposed a method where the bifurcation phenomenon is eliminated during the design procedure [42]. [1]

The proposed method follows a similar approach. Using the first harmonic approximation (FHA) and under the assumption of 100% efficiency, initial system parameters can be defined as in Table 6.1.

An initial selection should be made for the percentage (Ψ) of the resonator current to the Tx current as in (6.5).

$$\Psi = \frac{I_R}{I_{Tx}} = 1 \tag{6.5}$$

From (6.5) I_R can be found as 5.55 A_{rms}. At the resonant frequency, the induced voltage on the Tx coil is equal to the input voltage. Hence the mutual inductance between Tx and resonator coils can be calculated as in (6.6).

$$M_{Tx,R} = \frac{V_{in}}{\omega_0 I_R} = 15.62\ \mu H \tag{6.6}$$

[1] Bifurcation is the pole siplitting phenomenon occurs for doubly-tuned circuits. Under high-loading or coupling operation above resonant frequency doesn't guarentee ZVS operation. Details were previously discussed in section 2.1.3

Table 6.1: System Parameters

Parameters	Value
Power Rating	500 W
Input Voltage $\mathrm{V_{in}}$	100 V_{DC}
Output Voltage $\mathrm{V_{out}}$	100 V_{DC}
Resonant Frequency	150 kHz
Load Resistance $\mathrm{R_L}$	20 Ω
Input Voltage $\mathrm{V_{in,rms}}$	90 V_{rms}
Output Voltage $\mathrm{V_{out}}$	100 V_{rms}
Input Current $\mathrm{I_{Tx}}$	5.55 A_{rms}
Output Current $\mathrm{I_{Rx}}$	5 A_{rms}

A similar approach can be made for the mutual inductance between resonator and Rx side coils as in (6.7).

$$M_{Rx,R} = \frac{V_{out}}{\omega_0 I_R} = 17.36\ \mu H \tag{6.7}$$

At this stage, two parameters should be selected, which are the coupling factors between Tx-resonator ($k_{Tx,R}$) and resonator-Rx side ($k_{Rx,R}$). A selection of relatively low quality Rx side is necessary, as discussed before. Since our load resistance is constant during operation, low Rx side inductance should be selected. A selection of $Q_{Rx} = 1.5$ and $k_{Rx,R} = 0.4$ is found to be suitable for our design. High coupling between resonator and Rx side means that the air gap is small between these coils. Hence, the Rx side inductance can be calculated as in (6.8) where R_{equ} is the resistance seen from the diode rectifier in the Rx side.

$$L_{Rx} = \frac{Q_{Rx} R_{equ}}{\omega_0} = 25.47\ \mu H \tag{6.8}$$

Since the $k_{Rx,R} = 0.4$ was selected, it is now possible to determine the resonator inductance as in (6.9).

$$L_R = \frac{M_{Rx,R}}{k_{Rx,R}^2 L_{Rx}} = 73.98\ \mu H \tag{6.9}$$

At this stage, the equivalent load resistance(R_{equ}) can be reflected to the resonator side to find the quality factor of the resonator(Q_R) given in (6.10).

$$Q_R = \frac{\omega_0 L_R}{R_{ref}} = \frac{\omega_0 L_R R_{equ}}{\omega_0^2 M_{Rx,R}^2} = 4.167 \tag{6.10}$$

In order to achieve a bifurcation free operation the critical coupling formula presented in [42] is used. The critical coupling(k_c) is found in (6.11) .

$$k_c = \frac{1}{Q_R}\sqrt{1 - \frac{1}{4Q_R^2}} = 0.2382 \tag{6.11}$$

It is important to note that this approximation is only valid when the Q_{Rx} is selected low and/or $k_{Rx,R}$ is selected to be high. A selection of 0.2 for the coupling between Tx and resonator($k_{Tx,R}$) is found to be suitable for bifurcation free operation. Finally, the Tx side coil inductance can be calculated as in (6.12).

$$L_{Tx} = \frac{M_{Tx,R}}{k_{Tx,R}^2 L_R} = 82.51\ \mu H \tag{6.12}$$

All three coils are adjusted to have the same resonant frequency and hence the C_{Tx}, C_R and C_{Rx} can be calculated as in (6.13).

$$\begin{gathered} C_{Rx} = \frac{1}{L\omega_0^2}, C_{Tx} = 13.6\ nF \\ C_R = 15.21\ nF, C_{Rx} = 44.2\ nF \end{gathered} \tag{6.13}$$

The presented methodology is appliable for various applications ranging from small power applications to large power applications like electric vehicle IPT chargers by using the generalized design flow-chart is given in Fig. 6.3. The finalized system parameters for the contactless slip ring design are presented in Table 6.2.

The initial assumption of a low Q_{Rx} allowed us to use of conventional IPT design as proposed in [42]. However, the feasibility of the assumption should be checked. In Fig. 6.4 the critical coupling of the analytical design and simulations are given. The design is repeated with a higher Q_{Rx}, and the analytical k_c value are given. The L_{Tx} is calculated using the analytical critical coupling value. For a low Q_{Rx} assumption, the analytical design gives successful limitations for bifurcation free operation. Whereas simulation limits deviate from analytical design as Q_{Rx} increases. The increase of Q_{Rx} also increases the sizing of the Rx side IPT coil whereas, the resonator and Tx side coil sizes decreases.

6.2 IPT Coil Design Considerations

In the previous section, a design methodology for the proposed topology was introduced. Although there are a few studies about the effect of coupling between the Tx

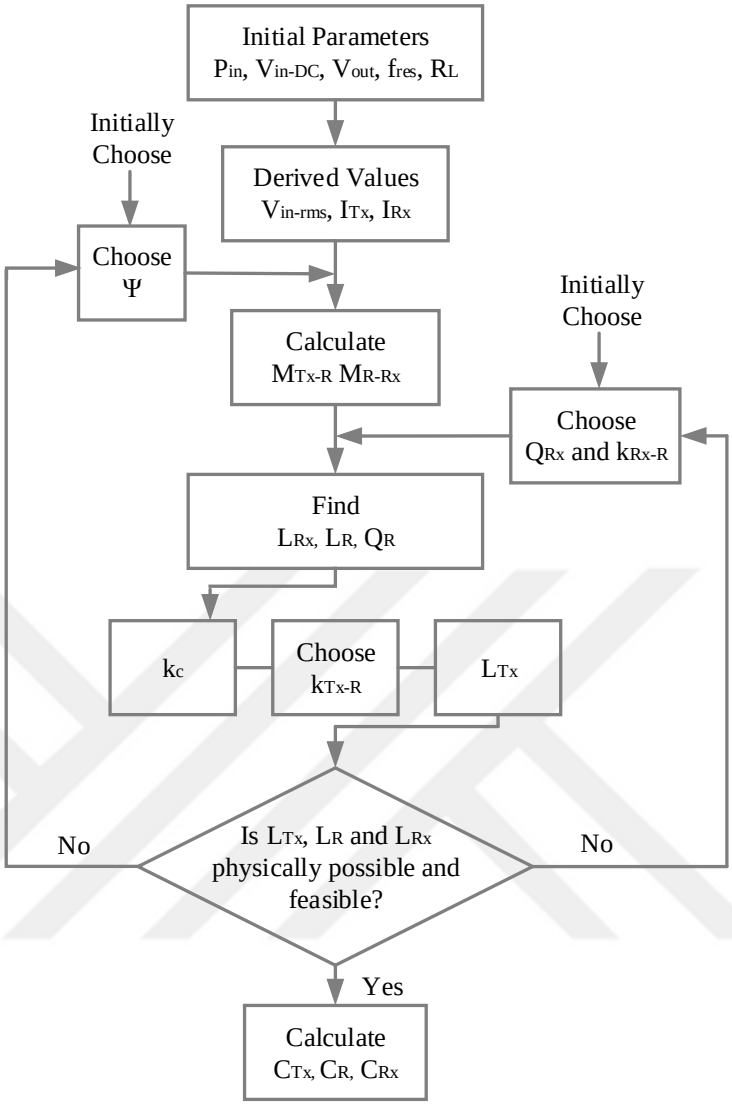


Figure 6.3: Flowchart of the proposed design.

and Rx coils [50, 51], the coupling between Tx and Rx coils should be eliminated for the proposed design method. Since the air gap is under the designer's control, the resonator coil can be separated into two coils that are connected in series, where one coil couples the Tx and the other coil couples the Rx coils. With the addition of ferrite shielding between the resonator coil sections, the coupling between the Tx and Rx modules can be significantly reduced. However, it is important to note that the mutual inductances given in Table 6.2 will be harder to achieve with large air gaps. Therefore, the feasibility of such a system structure should be investigated with pos-

Table 6.2: Final System Parameters

Parameters	Contactless Slip Ring
Resonant Frequency	150 kHz
Ψ	1
L_{Tx}	82.51 μH
L_{R}	73.98 μH
L_{Rx}	25.47 μH
C_{Tx}	13.60 nF
C_{R}	15.21 nF
C_{Rx}	44.20 nF
$M_{Tx,R}$	15.62 μH
$M_{Rx,R}$	17.36 μH
$k_{Tx,R}$	0.2
$k_{Rx,R}$	0.4

sible iterations based on the block diagram presented in Fig. 6.3.
In the proposed system structure, the resonator can be placed on both the rotating and stationary frame. Since the mutual inductance between the resonator and Rx coils is higher, the resonator coil is placed at the rotating frame. However, relatively lower mutual inductance and magnetic coupling between the Tx and the resonator coil results in a larger air gap.

The sizing of the ferrite core is highly dependent on the required level of fault tolerance. For open-circuited Rx module faults, the output power will be shared by the remaining Rx modules. Hence, choosing a larger core provides safe operation under Rx module faults. After the initial design, PQ32x20 with N87 material with an air gap of 0.4 mm was found to be the minimum required magnetic core. Therefore, PQ35x35 with N87 material is selected as the magnetic core. The finalized HF coupled inductor (HFCI) parameters are presented in Table 6.3.

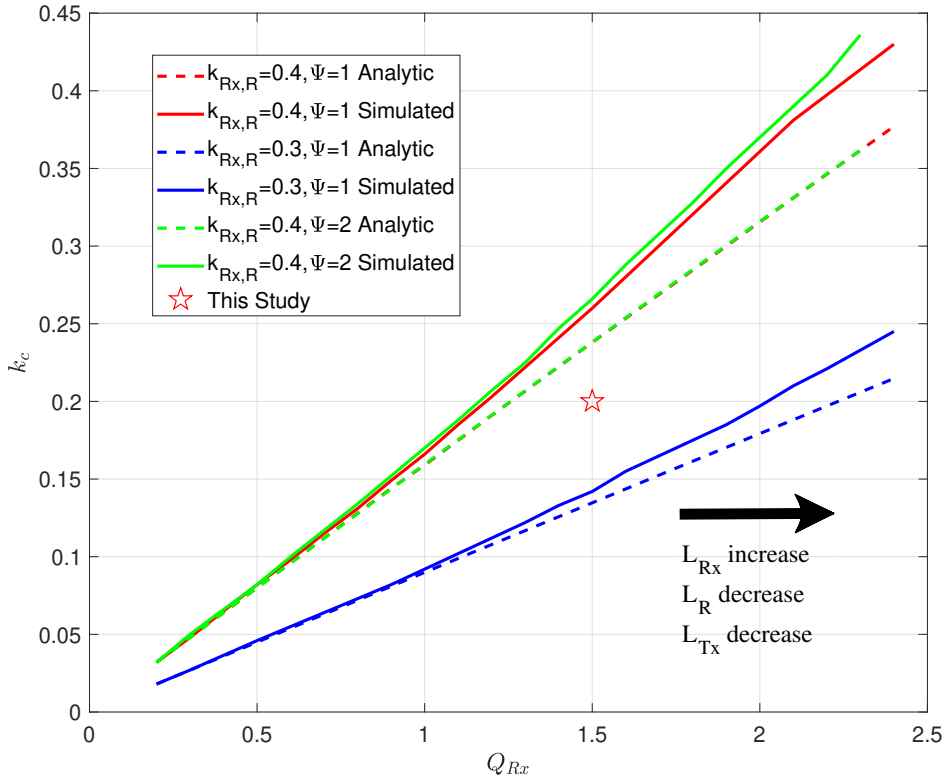


Figure 6.4: Comparison of analytical and simulated critical coupling for different design parameters.

The resonator sides of the HFCI presented in Table 6.3 are connected in series, and 53 μH was achieved for the Rx side resonator coil. Therefore for the Tx side, a coil with $L_{self} = 21\ \mu H$ and $L_{Tx-R} = 15.62\ \mu H$ is designed.

The self inductance of the resonator coil was calculated as 74 μH. Since we have four HFCI connected in series on the resonator side, the remaining inductance of 20 μH should be wound as an IPT coil. The resonator coil geometry and FEA is given in Fig. 6.5. The geometric parameters of the resonator coil are given in Table 6.4.

6.3 Experimental Results

To verify the proposed system, a 1 kW prototype is built with 2Tx-4Rx module and a single middle stage resonator as shown in Fig. 6.6. The experimental setup pa-

Table 6.3: Parameters of the High Frequency Coupled Inductors

Parameters	$HFCI_1$	$HFCI_2$	$HFCI_3$	$HFCI_4$
$L_R(\mu H)$	13.37	13.27	13.19	13.25
$L_{Rx}(\mu H)$	26.88	26.85	26.89	27.07
$M(\mu H)$	18.05	18.14	18.01	18.09
Core Size	PQ 35x35			
Core Material	N87			
Airgap	0.4 mm			
Number of R Turns	6			
Number of Rx Turns	9			

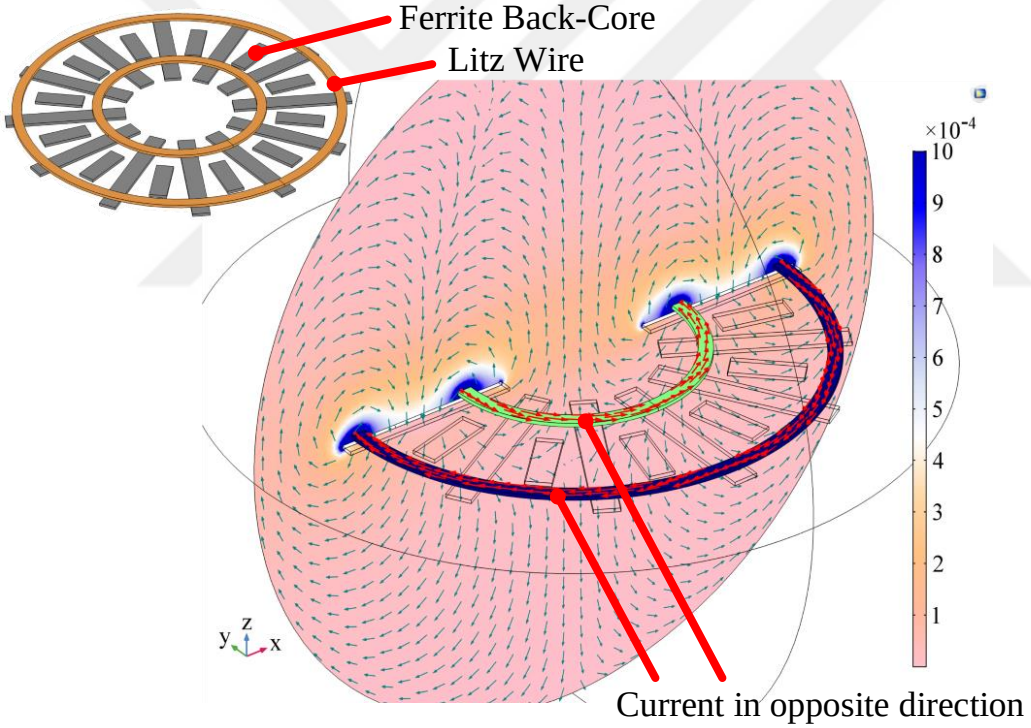


Figure 6.5: Resonator IPT coil geometry and FEA solution. The color table indicates the B-field magnitude on the circular surface in $\frac{Wb}{m^2}(T)$.

rameters are listed in Table 6.4. Unlike most IPT systems, the air gap of the IPT system is under the designer's control for the contactless slip ring design. However,

as stated previously, fault tolerance is the key for reliable operation, which is the main motivation behind adding a resonator coil.

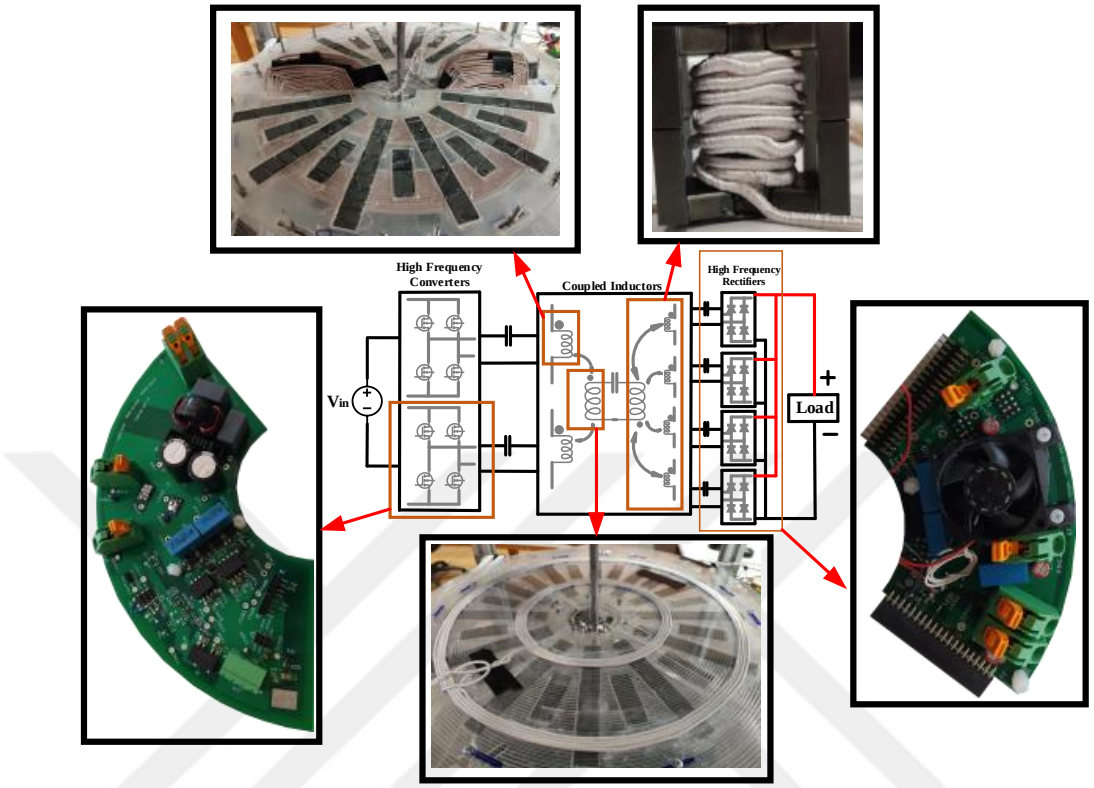


Figure 6.6: Experimental setup for the proposed IPT system.

At this stage, it is essential to discuss the effect of rotation. The rated rotational speed is set to be 1500 rpm (25 Hz) with a resonant frequency of 150 kHz. Therefore for a complete rotation, there exists 6000 gate switching, which results in nearly 17 gate switchings for 1° rotation. Moreover, the Tx and the resonator coil design satisfy constant k_{Tx-R}, and hence the system can be assumed to be stationary regardless of the angular speed.

6.3.1 Normal Operation

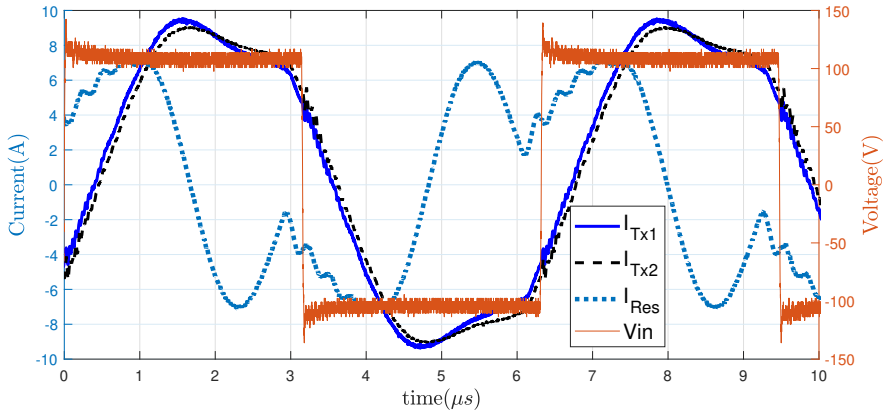
Firstly, the system is operated at 156 kHz, slightly above the resonant frequency, which satisfies the zero voltage switching. The experimental results under normal

Table 6.4: Experimental Setup Parameters

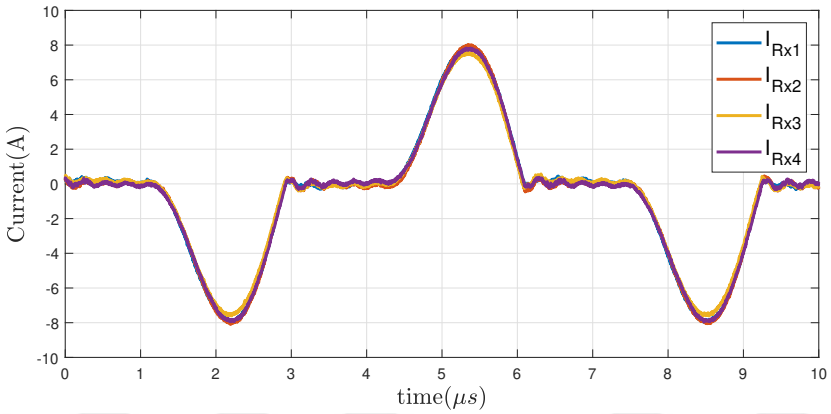
Tx side MOSFET	BSC600N25NS3G
Tx side Gate Driver	2EDF7275F
Rx side Recrifier Diodes	C3D10060G
Litz Wire	400x0.08mm ($2\ \mathrm{mm}^2$)
Tx coil $\mathrm{D_{in}}$ and $\mathrm{D_{out}}$	70-280 (mm)
Tx coil # of turns	13
Tx coil inductances	83.1-83.5 (μH)
Resonator IPT coil $\mathrm{D_{in}}$ and $\mathrm{D_{out}}$	65-280 (mm)
Resonator IPT coil # of turns	5
Resonator IPT coil inductance	23 (μH)
$\mathrm{C_{Tx}}$	13.6 (nF)
$\mathrm{C_{R}}$	15.21 (nF)
$\mathrm{C_{Rx}}$	44.2 (nF)
Airgap	5 (mm)
$\mathrm{f_0}$	150 kHz
f	155 kHz
Ferrite shield	I20x2 N48

operation are given in Fig. 6.7. The Rx currents are nearly equal and have a third harmonic component due to full-bridge diode rectifiers at the output stage. The reflected third harmonic component can also be seen at the resonator current.

In the analytical design, under 100% efficiency assumption, the Tx and resonator currents are taken equal. In the proposed system, the resonator coil is divided into two parts where the coupling between the resonator and Rx side is achieved by HFCI's. Therefore, the length of litz wire used is much shorter than the Tx coils. Moreover, the HFCI's are slightly over-designed to satisfy the rated power transfer under single Rx module open circuit fault condition. Moreover, since ZVS operation is achieved, semiconductor losses are significantly reduced. Hence, it is safe to assume that the



(a) V_{in},$I_{Tx1,2}$ and I_R for normal operation.



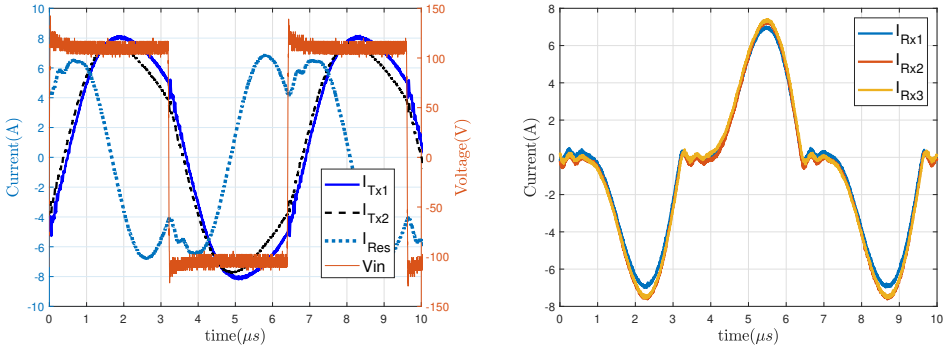
(b) Rx module currents for normal operation.

Figure 6.7: Input voltage, Tx side currents, resonator current and Rx currents for no-fault operation. ($I_{Tx1,2} \approx 6.5\ A_{rms}, I_R = 5.4\ A_{rms}$)

majority of the power loss occurs on the Tx side IPT coils. Therefore, unlike the analytical design, Tx currents are slightly higher than the resonator current.

6.3.2 Single and Double Rx Open Circuit Fault

In Fig. 6.8 a single Rx open circuit fault is presented. As there are faulty Rx modules, the output power is shared between the remaining Rx modules. Therefore the power can either be reduced, which will result in a smaller system, or the Rx module can be over-designed, and hence the output power can be kept at the desired value under faulty conditions. Increasing the number of Rx modules will result in less stress on

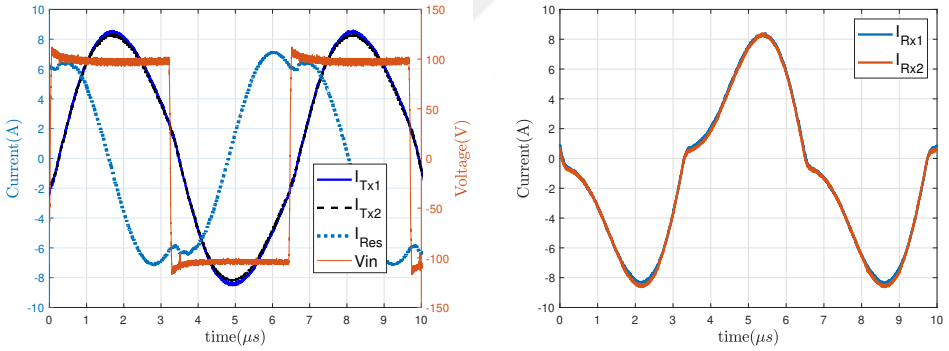


(a) V_{in},$I_{Tx1,2}$ and I_R for single open-circuit Rx fault condition.

(b) Rx module currents for single open-circuit Rx fault condition.

Figure 6.8: Input voltage, Tx side currents, resonator current and Rx currents for single open circuited Rx fault.

the remaining modules under faulty conditions; however, it also increases the chance of a semiconductor failure due to the increased number of semiconductors.



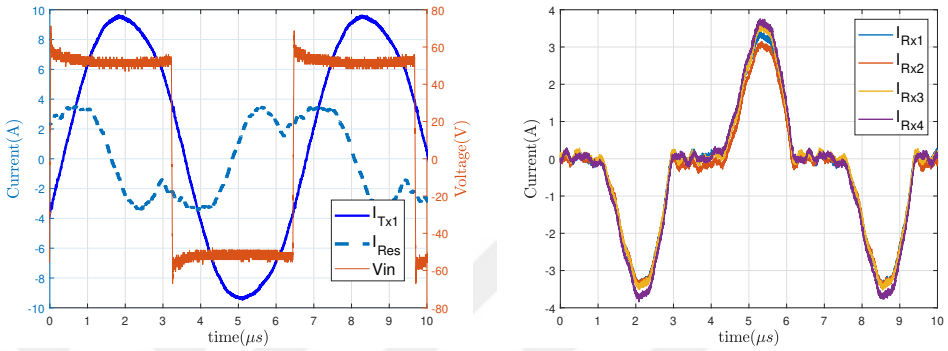
(a) V_{in},$I_{Tx1,2}$ and I_R for double open-circuit Rx fault condition.

(b) Rx module currents for double open-circuit Rx fault condition.

Figure 6.9: Input voltage, Tx side currents, resonator current and Rx currents for , double open circuited Rx fault.

The proposed system is tolerant to receiver module faults. Under single Rx module open circuit faults, the Rx module currents are still nearly equal as shown in Fig. 6.8. The loss of a single Rx module resulted in a decrease of the reflected third harmonic component in the resonator current.

Then the effect of simultaneous faults in two Rx modules is investigated. The results are presented in Fig. 6.9. The reflected third harmonic component reduced even further on both the Rx and resonator current. Since less modules are transferring power in this case, the over-design rating of the Rx modules must be higher in order to supply rated output power.



(a) V_{in},$I_{Tx1,2}$ and I_R for since open-circuit Tx fault condition.

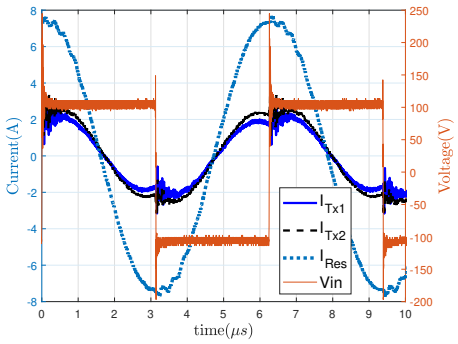
(b) Rx module currents for single open-circuit Tx fault condition.

Figure 6.10: Input voltage, Tx side current, resonator current and Rx currents for single open circuited Tx fault.

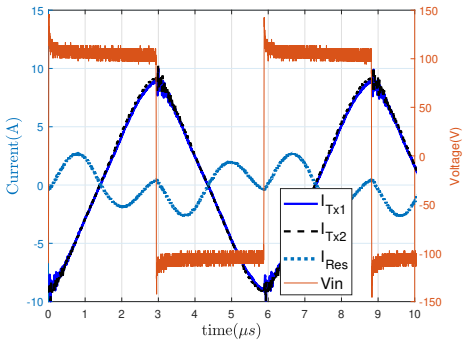
6.3.3 Single Tx Open Circuit Fault

Finally, a single open circuit Tx fault is applied. Although the rating of each module is 500 W, a maximum of 250 W is transferred due to the current limit as shown in Fig. 6.10. Again the Rx module currents are nearly identical. The induced emf on the Tx side depends on the frequency, mutual inductance, and the secondary side current. Under an open-circuited Tx fault, the flux linkage is reduced by half, which also decreases the resonator current. Therefore, the induced emf on the Tx side is also halved, which results in high currents drawn from the source. Limiting the output power, the rated power under open-circuited Tx faults, the current rating of the Tx side power semiconductors should be increased. Another method is to increase the number of Tx modules, which will surely decrease the stress on the remaining modules during

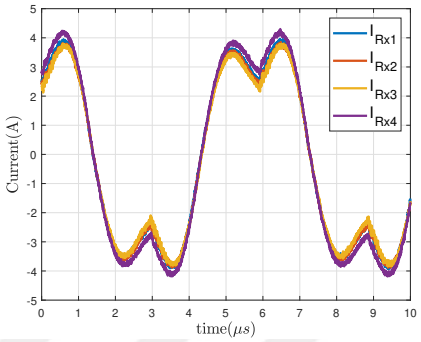
fault.



(a) Open circuit fault V_{in}, I_{Tx} and I_R.



(b) Short circuit fault V_{in}, I_{Tx} and I_R.



(c) Short circuit fault I_{Rx}.

Figure 6.11: Open and short circuit fault conditions. V_{in}, I_{Tx}, I_R and I_{Rx} are shown for each type of fault. $f_{operation} = 165\ kHz$

6.3.4 Open and Short Circuited Load Fault

The experimental results for open and short-circuited load conditions are also given in Fig. 6.11. In conventional series-series IPT systems, during open-circuited faults, the induced emf on the Tx side is theoretically zero, which results in dangerously high Tx side input currents. However, in the proposed system, it is the opposite. The induced emf on the resonator due to the Rx side becomes zero, and the intrinsic resistance of the resonator coil acts as the load. Assuming that the system operates near resonance

frequency, the reflected impedance on the Tx side can be written as in (6.14).

$$Z_{ref} = \frac{\omega^2 M_{Tx-R}^2}{j\omega L_R + \frac{1}{j\omega C_R} + R_R} \approx \frac{\omega^2 M_{Tx-R}^2 \omega^2}{R_R} \tag{6.14}$$

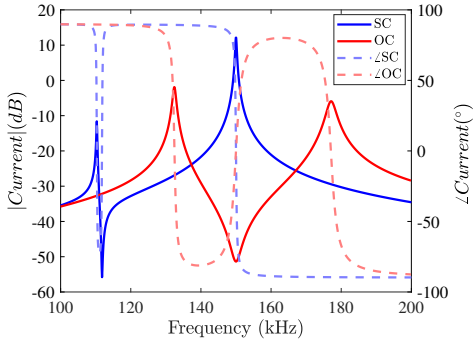
Therefore, the induced emf on the Tx side is high, which results in low input currents. The experimental results also support the analytical discussion as given in Fig. 6.11-a. The short-circuited load condition is more challenging. The reflected impedance from the Rx to the resonator side becomes extremely high. Due to high impedance, resonator current reduces, and the reflected impedance on the Tx side due to the resonator becomes low. Therefore, dangerously high Tx input currents can be induced. The experimental results for open and short-circuited load conditions are given in Fig. 6.11. At this stage, it is important to discuss a critical property of IPT systems with a middle resonator coil. Unlike conventional IPT systems, there exist three resonant frequencies, including the design resonant frequency. The upper frequency can be presented as in (6.15) where $L_{Tx,leakage}$ is the leakage inductance of the Tx coil[52].

$$\omega_{upper} = \frac{1}{\sqrt{C_{Tx} L_{Tx,l}}} \approx 175\ kHz \tag{6.15}$$

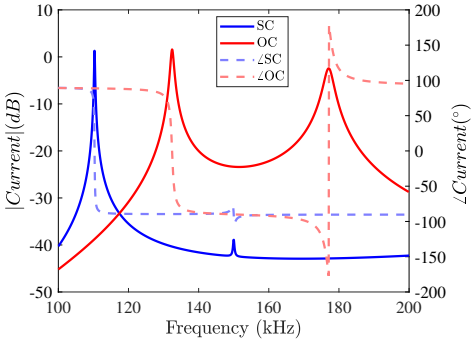
The open and short circuit fault conditions are simulated in the frequency domain using the proposed system parameters and the results are presented in Fig. 6.12. During short-circuited load conditions, the quality factor of the input current gain increases significantly. Therefore, under the assumption of operation at slightly above the resonant frequency (to guarantee ZVS), the system is highly fault tolerant to short-circuited fault conditions.

Under open-circuited load condition, the situation is a bit different. Similar to the short circuit fault case, the quality factor of the input current increases significantly. However, for the higher resonant frequency, ω_{upper}, the current gain increases significantly. Moreover, the input current starts to lead the input voltage, which results in the loss of ZVS operation. However, the magnitude of the input current drops which results in purely capacitive power drawn from the source with a magnitude less than the nominal real power.

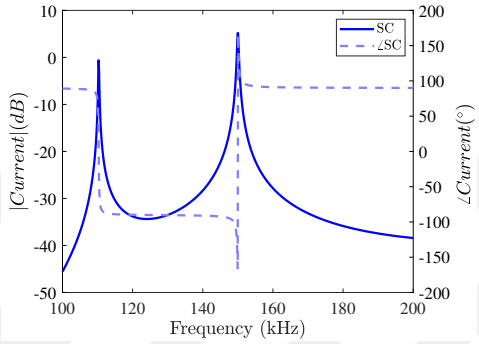
Although the system is tolerant to both open and short circuited load faults, it is not feasible to further transfer power under these fault conditions. These analyses show that even if there is a load fault, the results are not catastrophic, and the system can be



(a) Open and short circuit fault simulations for I_{Tx}.



(b) Open and short circuit fault simulations for I_R.



(c) Open and short circuit fault simulations for I_{Rx}.

Figure 6.12: Open and short circuit fault condition simulation in frequency domain. I_{Tx}, I_R and I_{Rx} are shown for each type of fault.

turned off safely. The system is tested under various faults. The system efficiencies for the rated power of the system are given in Table 6.5.

6.4 Discussion

The experimental results show that the proposed design is highly tolerant to Tx and Rx side open circuit faults. However, few topics require special attention, which are the effect of modularity on the fault tolerance to open circuit Tx faults, modes of operation, and the origins of the third harmonic component in the Rx currents under normal and fault conditions.

Table 6.5: Efficiencies of the System Under Different Fault Conditions

Operation	P_{in}(W)	P_{out}(W)	Efficiency(%)
Experimental	1103.0	1000.0	90.9
Single Rx open fault	993.9	891.0	89.6
Double Rx open fault	988.8	885.5	89.5
Single Tx fault	296.9	242.4	81.6

6.4.1 Effect of Modularity on Fault Tolerance

Another critical topic is the discussion of the number of modules and maximum power transfer under a single Tx module fault condition. As stated in the experimental results, for a total of 1 kW system having two 500 W rated Tx modules, the maximum power which can be delivered under a fault condition is 250 W due to the current rating of the module. In Fig. 6.13, a theoretical approach for Tx module number, power rating per module, and maximum power transfer capability under single Tx module open-circuit fault is given. If it is desired to transfer rated power under a single Tx fault condition, it is feasible to increase the number of Tx modules. However, as the module number increases, the system sizing is problematic due to the reduced air gap to achieve the designed coupling between the Tx and the resonator coils. Moreover, the decrease of the intrinsic quality factor of the Tx modules will reduce the overall system efficiency. Therefore, the number of Tx modules is highly dependent on the system requirements.

6.4.2 Modes of Operation

The proposed system has two separate modes of operation, which are constant voltage (CV) and constant current (CC) points. The CV point is at the design resonant frequency ($f_0 = 150\ kHz$), and the CC point is at the upper resonant frequency ($f_{upper} = 187\ kHz$). In Fig. 6.12, the zero phase angles are at 150 kHz and 178 kHz which overlaps with ω_{upper} given in (6.15). The slight differences between the simulation and experimental results are due to the slight deviation of the experimental parameter compared to the design parameters.

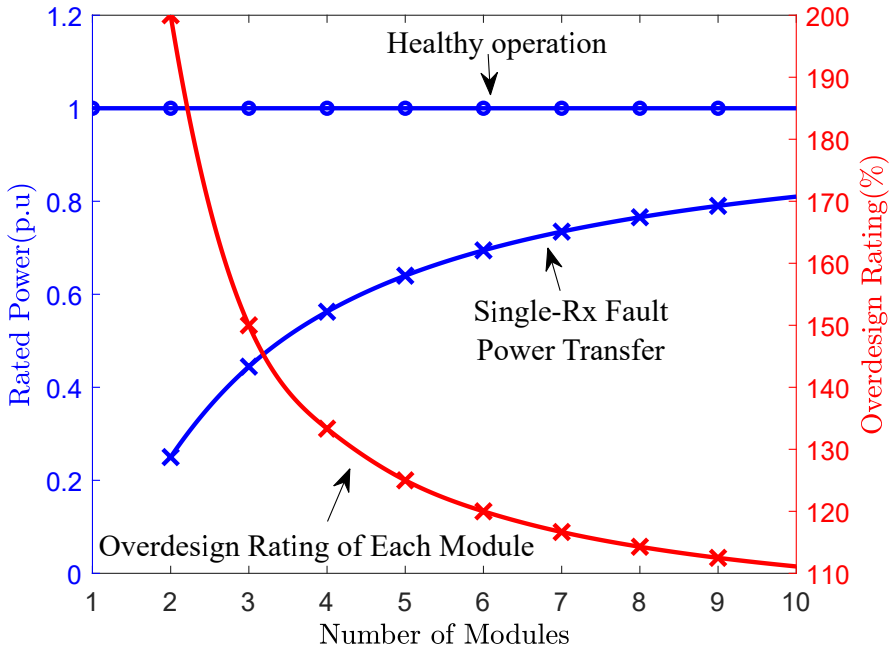
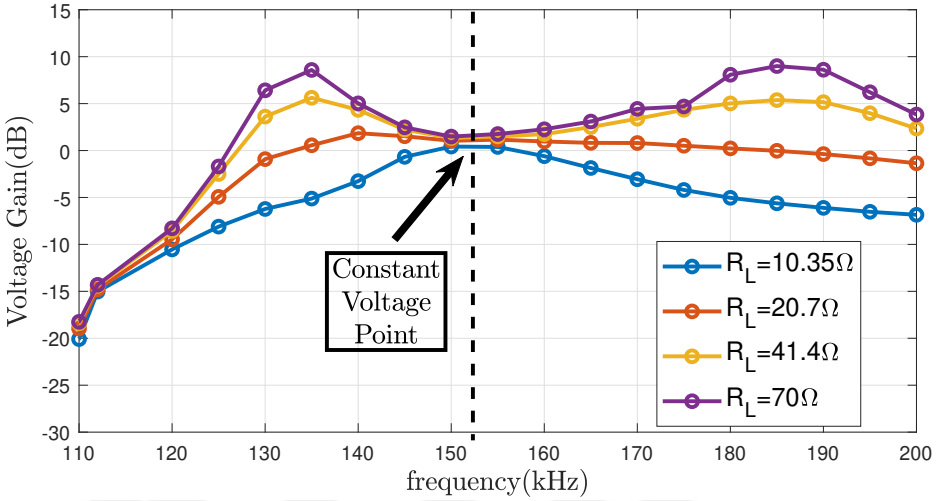
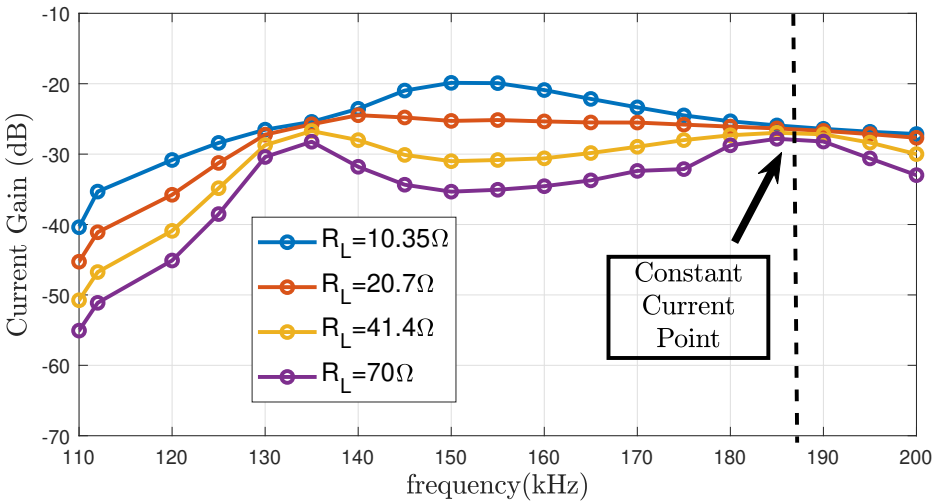


Figure 6.13: Theoretical maximum power transfer for normal and single Tx side open circuit fault condition. Over-design rating of each Tx module to transfer the rated power under fault condition is also given.

The operation frequency is swept over a wide range to achieve the voltage and current gain plots for different load conditions under CV and CC operations as shown in Fig. 6.14. The data are taken for low voltage/power input since the loss of ZVS results in increased switching loss. CV and CC operation is beneficial for battery



(a) Voltage gain for different loading conditions.



(b) Current gain for different loading conditions.

Figure 6.14: Voltage and current gain plot for the experimental setup under different loading conditions. The CV and CC operation points are also presented.

charger applications. However, as also given in Fig. 6.12, under CV operation, the

system is prone to short circuited load fault, and the opposite is valid for CC operation. Therefore, the system should still have over-current protection.

6.4.3 Third Harmonic Component

In this study, the design methodology based on fundamental harmonic approximation (FHA) is presented under these assumptions: No-higher order harmonics and continuous coil current, also known as continuous current mode (CCM)[53]. However, an IPT system can also operate in discontinuous current mode (DCM) because of the diode rectifiers, and load conditions [54]. In DCM, the current of the coils have odd harmonics (3rd, 5th), which are comparable to fundamental component. Thus, the results may deviate from the FHA model. In this situation, the time-domain analysis (TDA) can be applied to consider the harmonics into account [55]. Although the system is designed using FHA (considering CCM), we have experiment and simulation results having odd harmonics, which shows that the system is actually in DCM. However, a significant challenge is to obtain a bifurcation-free operation with the proposed modular design. The operation in DCM does not affect the bifurcation phenomenon and the power output. Thus, odd harmonics (especially the third) do not significantly distort the FHA assumptions, which can be used to obtain a bifurcation-free system.

6.5 Three Coil Rotational System

In Chapter 5, the 2Tx-4Rx system was tested for a complete rotation. Although the system satisfied the initial requirements, operation under fault condition was below the desired fault tolerance criteria. With the addition of the middle stage resonator, the fault tolerance of the overall system significantly increased. The proposed three coil system was mounted on an electric motor as given in Fig. 6.15. The HFCIs are mounted between the resonator IPT coil and Rx side rectification modules. The power is delivered to the load using slip rings for testing purposes.

The Tx and resonator coils are placed in epoxy resin enhanced with fiberglass to achieve mechanical stability during rotation. However, due to the thickness of the epoxy, adjusting the air gap given in Table 6.4 becomes problematic. Therefore,

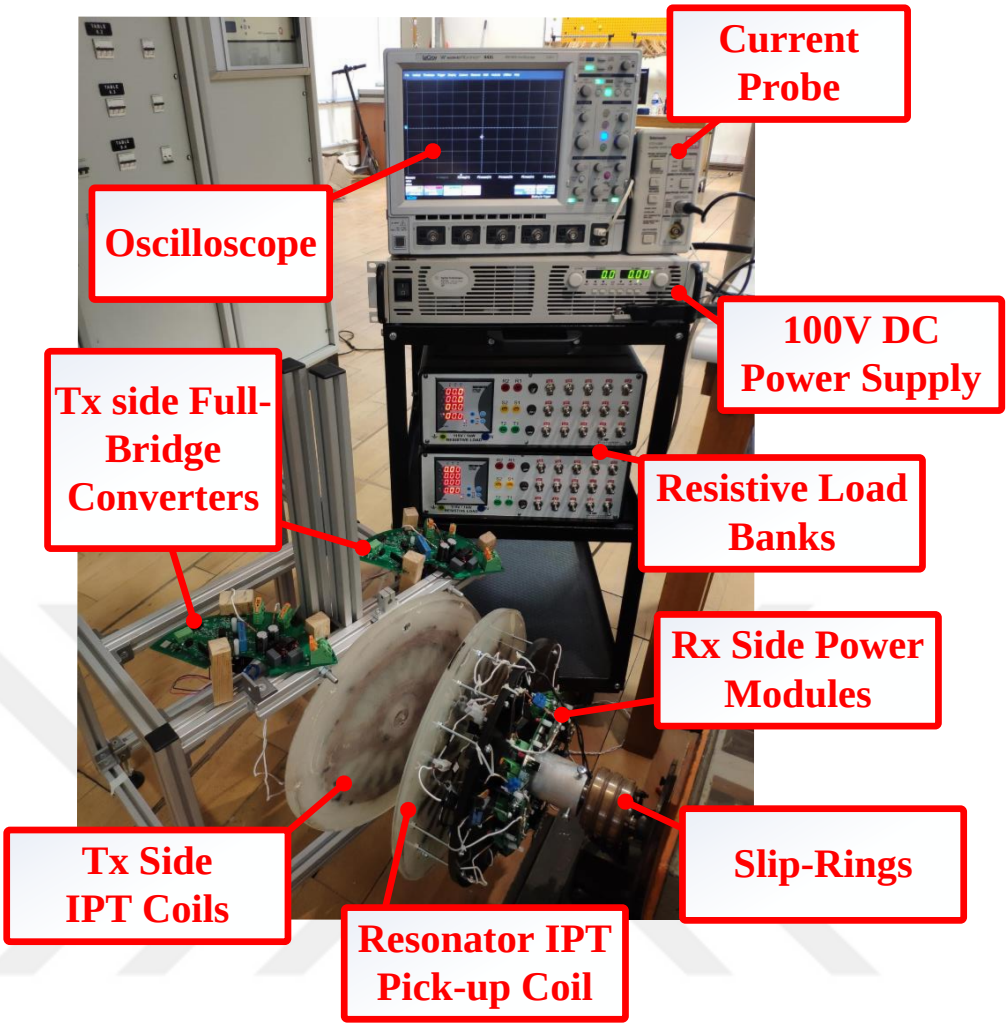
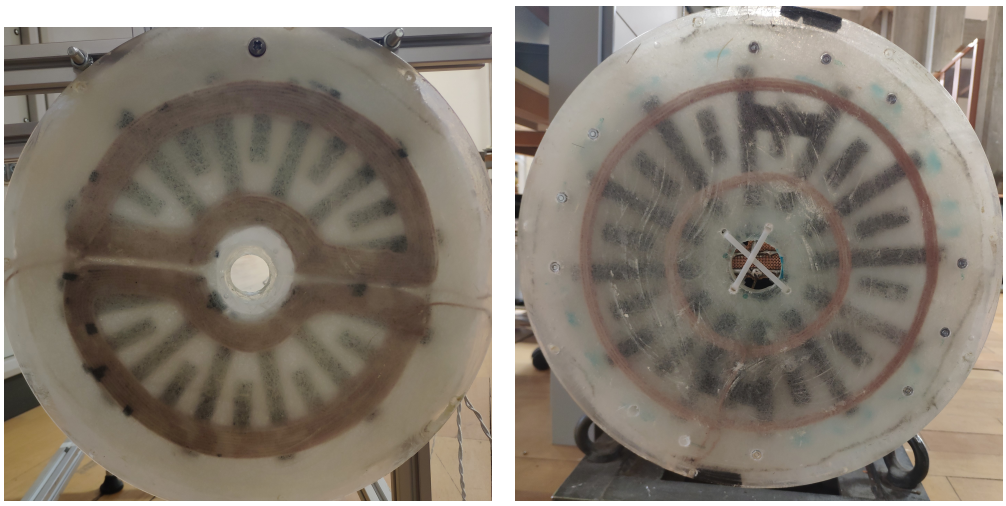


Figure 6.15: IPT system with middle stage resonator mounted on a rotating shaft. (The Tx side IPT coil is placed with an angle for visual clarity.)

a new set of Tx coils with an inductance of 150 μH was built. Compared to the initial three coil system, the upward curvature is also unnecessary as long as the $k_{Tx,R}$ couplings can be kept stationary. The new Tx coils and the resonator coils in epoxy resin are given in Fig. 6.16. Using ferrite strips, the intrinsic quality factor of the IPT coil decreases slightly; however, the amount of ferrite and the overall weight of the system decreases significantly.

The number of turns of each Tx coils are increased to 18 turns with 2 layers each having nine turns. This results in a coil with increased resistance, and hence the effi-



(a) Tx side IPT coil for rotational system. (b) Resonator IPT coil for rotational system.

Figure 6.16: Tx and resonator IPT coils in epoxy resin for the rotational system. Instead of using a complete back-core, ferrite sticks are placed.

ciency of the overall system is expected to be lower.

6.5.1 Experimental Results

The presented system is coupled to a DC motor where the rotational speed is determined by external DC input voltage. The Tx module currents are presented in Fig. 6.17. The rms of I_{Tx1} and I_{Tx2} are 6.73 A_{rms} and 6.3 A_{rms}. The slight difference and periodic oscillation indicate an axial misaligned resonator IPT coil. The testing is performed at 150 rpm.

The input voltage of the DC-supply is set to nominal 100 V_{DC}. The input DC current is measured in Fig. 6.18. The maximum and minimum input current is measured as 11.75 A and 9.45 A, respectively. Again the oscillation around 10.7 A indicates an axial misalignment. The average input power can be calculated as 1070 W.

Since the power at the Rx module is transferred to the stationary frame using slip rings, the load voltage can also be measured as given in Fig. 6.19. The average voltage across the resistive load is 94 V_{DC}. The maximum and minimum output voltages are

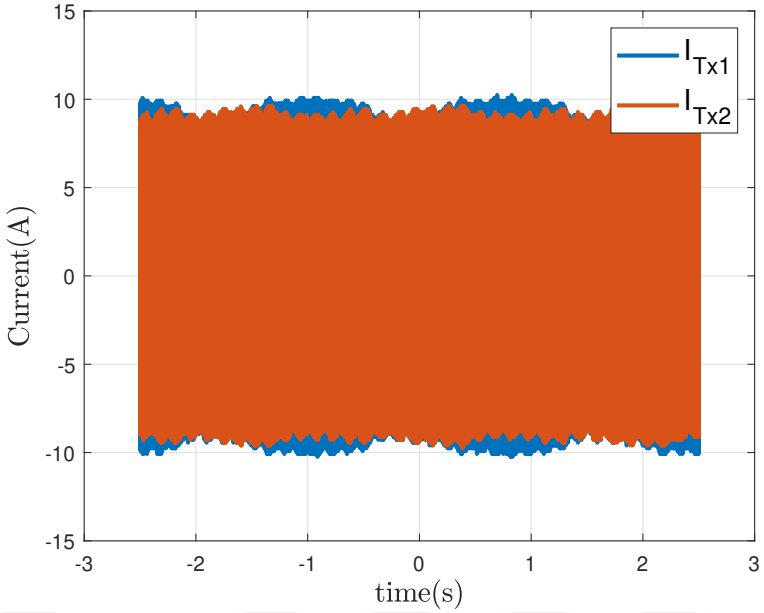


Figure 6.17: The measured AC Tx module current envelope at 150 rpm.

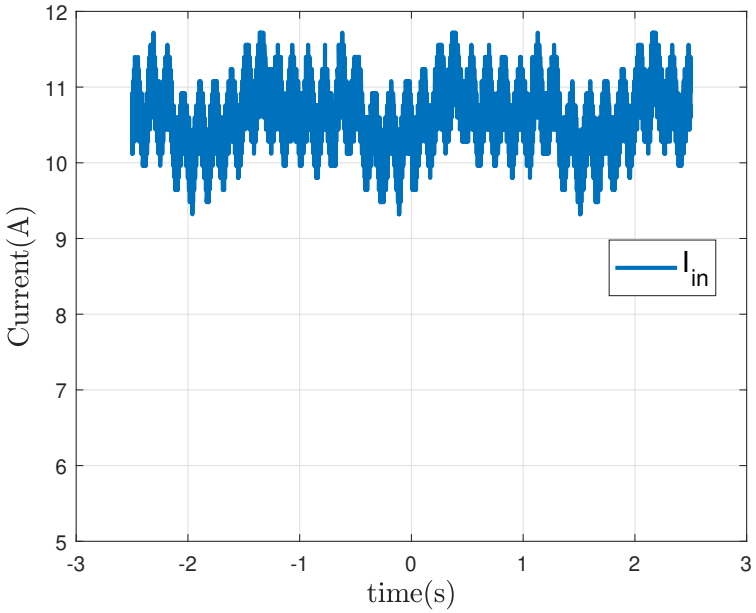


Figure 6.18: The measured input DC current at 150 rpm.

96 V and 90 V. The load resistance is set to 10.3 Ω. Using the load resistance and average voltage, the average output power can be calculated as 857 W, which results in an overall DC to DC efficiency of 80%. This value is not surprising since the

increased litz cable length in the Tx IPT coils. Also, there are extra resistive loss elements on the slip ring due to contact resistance.

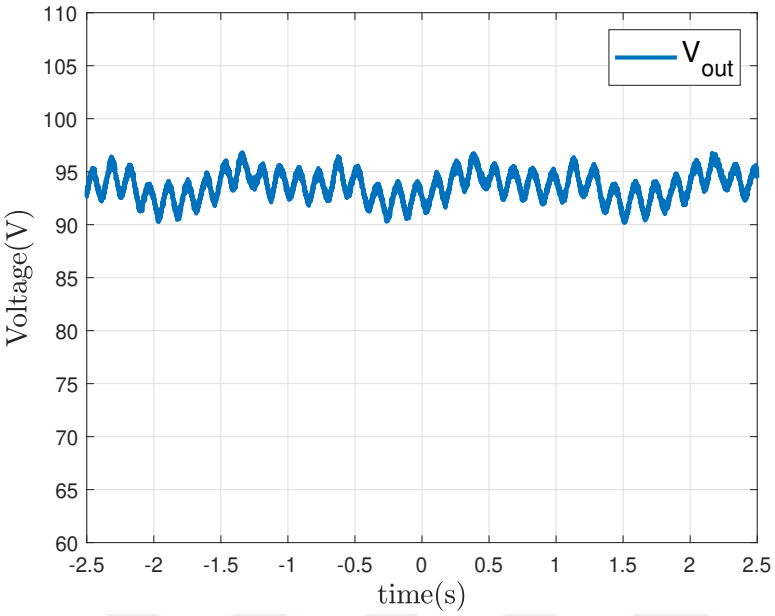


Figure 6.19: The measured output voltage at 150 rpm.

6.5.2 250 RPM Rotational Fault Tests

After testing the normal operation, fault tests are performed for the rotational system. Unlike the previous system, the frequency is kept constant at 155 kHz. For all fault simulations, open-loop frequency control is applied. The faults are simulated using relays and manual switches. The selected relay is a normally open 30 A relay with a working voltage of 12V. For all fault conditions, the system is rotated at 250 rpm.

6.5.2.1 Single Rx Open Circuit Fault

The relay is connected in series of a single Rx module IPT coil. The relay voltage is provided using additional slip rings. The output voltage is set to 80 V. While rotating at 250 rpm, the relay voltage is brought to 0 V using an isolated power supply. Even if the relay voltage is zero, the mechanical disconnection occurs shortly after the off signal. In Fig. 6.20, the fault transient of the Tx side currents and the output voltage

is presented. While the output voltage (V_{out}) stays constant, the Tx currents peak also reduces. However, peak reduction doesn't necessarily imply an increase in efficiency. In fact, the efficiency of a single Rx module fault compared to normal operation is constant as given in Table 6.5. In Fig. 6.7 the peak of Tx currents are between 9.25-9.6 A whereas in Fig. 6.8 they are 8 A. The reduction of the peak current is due to the reduction of the third harmonic component. In section 6.4.3, the origins of the third harmonic is discussed. Since the system operates at DCM, higher harmonic components flow through the circuit, and the third harmonic is also drawn from the Tx modules.

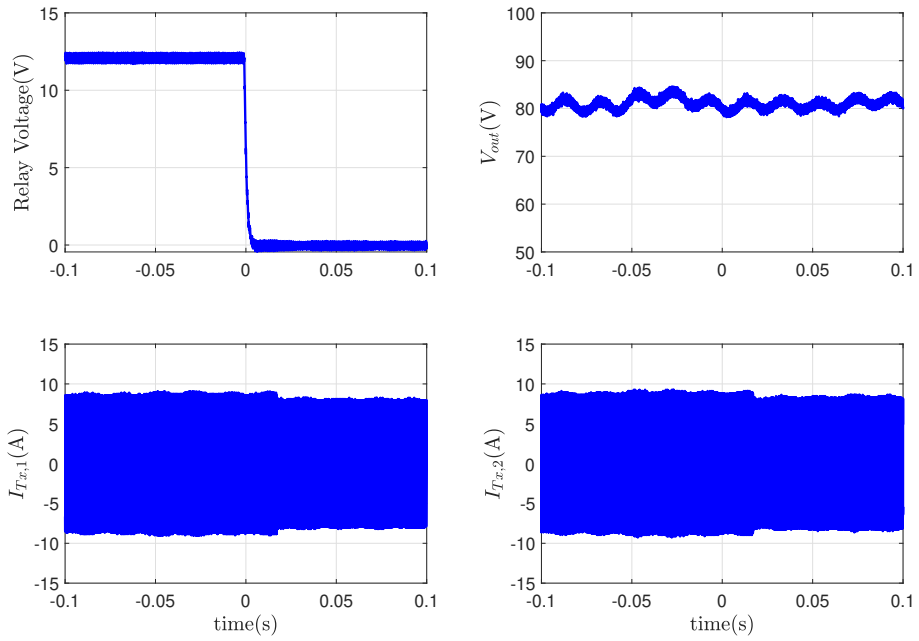


Figure 6.20: Single Rx coil open circuit fault for 250 rpm rotational speed.

6.5.2.2 Double Rx Open Circuit Fault

Using a similar approach, the double Rx module open circuit fault is modeled. This time two relays are connected in parallel, and the power lines are connected in series to two separate Rx IPT coil. In Fig. 6.21, the output voltage and Tx side currents are presented. The output voltage (V_{out}) increases while the peak of the Tx currents decreases. At first glance, the only possible explanation seems as if the efficiency;

however, from Table 6.5, it is known that the efficiency of the overall system reduces slightly due to increased thermal loss on the Rx side diodes. In Fig. 6.9, the third harmonic component is significantly reduced compared to normal operation. Therefore, the peak Tx module current difference is more visible in the double open-circuited fault case.

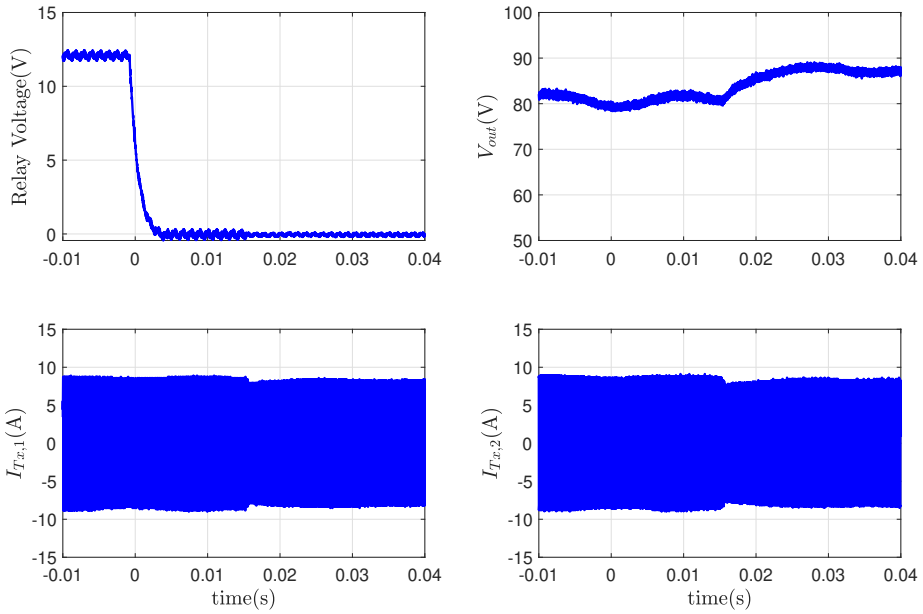


Figure 6.21: Double Rx coil open circuit fault for 250 rpm rotational speed.

6.5.2.3 Short Circuited Fault

The short-circuited fault modeling is achieved by a manual switch where the closure of the switch creates a short circuit fault condition on the output. In Fig. 6.12, the short circuit transconductance gain of the system is presented. As stated previously in section 6.3.4, the behavior of the system to open and short circuit fault conditions are highly dependent on the operation frequency. Since the system operates very close to the resonant frequency, the system is prone to short-circuited faults at 155 kHz. Therefore, the testing is performed at 40 V at the output. As expected, the Tx currents increase when the fault is applied.

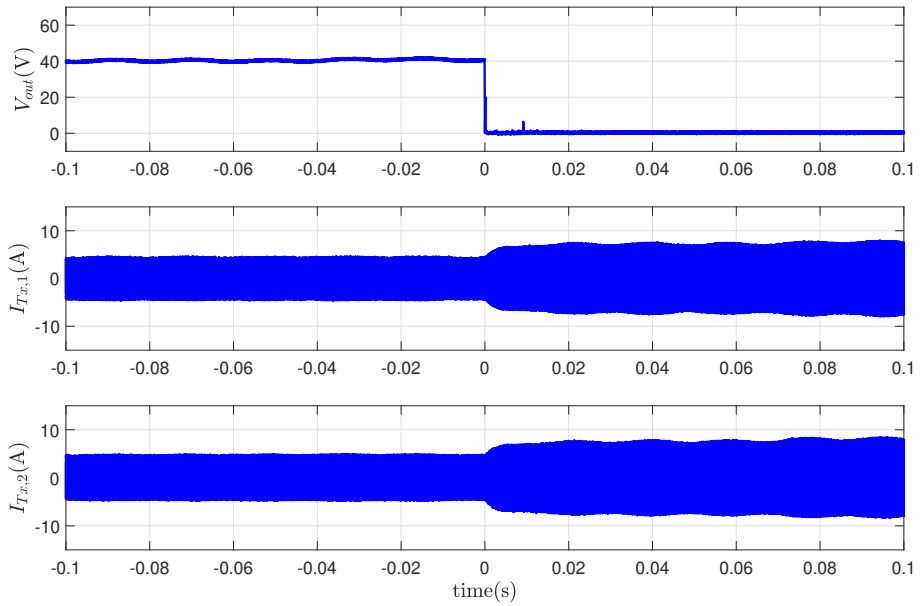


Figure 6.22: Short circuited load fault for 250 rpm rotational speed.

6.5.2.4 Open Circuited Load Fault

Similar to the short circuit fault case, an open-circuited load fault is modeled by connecting a manual switch in series with the load. In Fig. 6.12, the open circuit fault is problematic in the upper resonant frequency given in (6.15). Since the operation is close to the design resonant frequency, a sharp decrease in the Tx currents is expected. In Fig. 6.23, the voltage across the load and the Tx module currents are presented. After the fault, the Tx currents are highly capacitive, and ZVS operation is lost. However, since the apparent power of the system also drops sharply, the power loss due to hard-switching is thermally manageable. However, the system behavior under fault is again highly dependent on the operation frequency.

6.5.2.5 Single Tx Open Circuit Fault

Finally, a single Tx side open circuit fault is modeled using a series-connected relay to the Tx IPT coil. In Fig 6.24, the relay voltage, output voltage (V_{out}) and the Tx module currents are given. After the relay off signal is applied, arcing at the mechan-

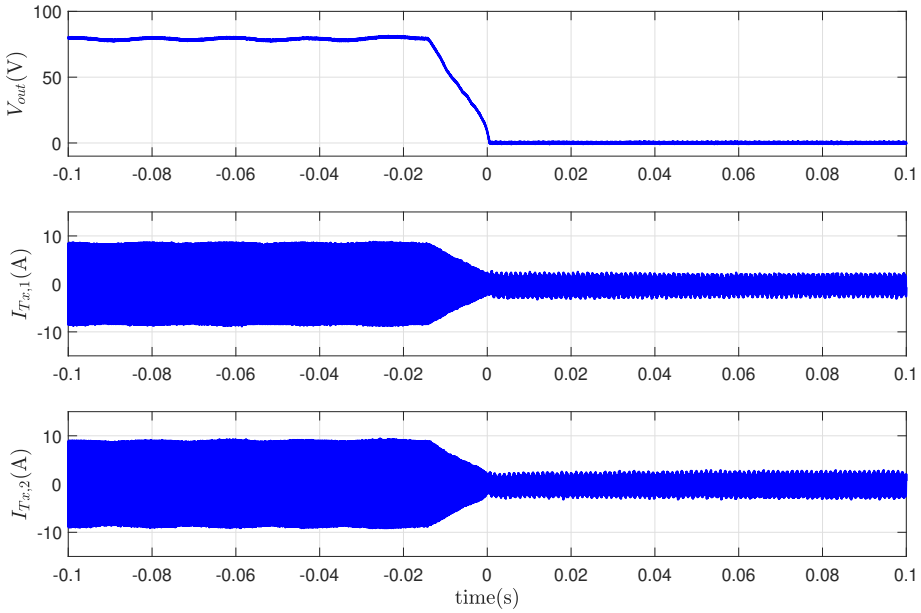


Figure 6.23: Open circuited load fault for 250 rpm rotational speed.

ical relay switch caused increased contact resistance, and hence voltage oscillations are observed until the electrical contact is diminished at $t = 0.042\ s$. While the output voltage drops to 20 V, a slight decrease in the current peak of the healthy Tx module is observed. Although this result seems to contradict the experimental results in Fig. 6.10, it is found to be due to the elimination of cross-coupling between the Tx IPT coil set. The explanation will be given in the next section.

6.6 Discussion

Unlike the previous experimental setup, the rotational system consists of two Tx coils with an inductance of 150 μH as given in Fig. 6.16-a. While the Tx coils are isolated with ferrite shielding at the up-curvature given in Fig. 6.6, the IPT coils in the rotational system have negative mutual inductance. Therefore, in the absence of the other coil, the inductance of the healthy module increases. The resonant frequency

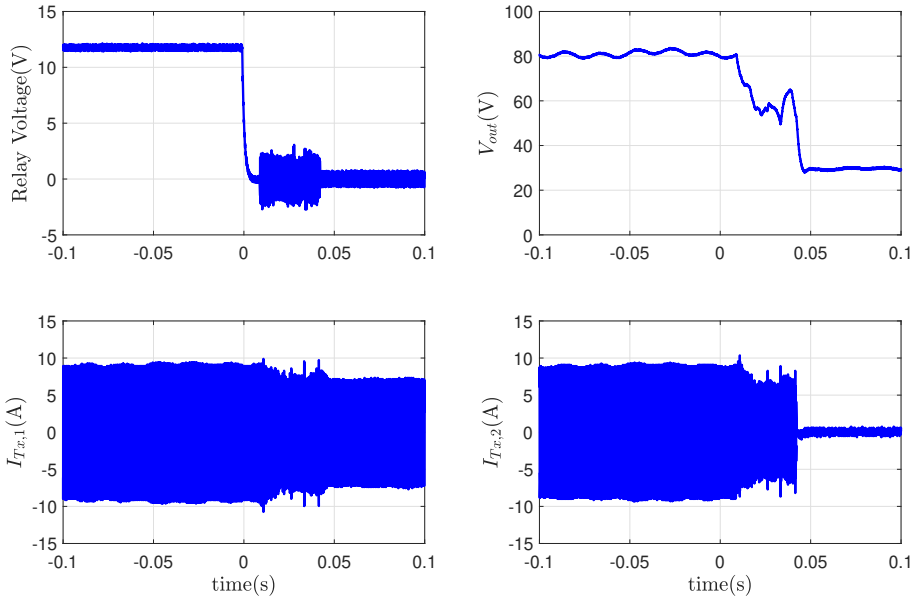


Figure 6.24: Short circuited load fault for 250 rpm rotational speed.

of series-connected LC circuit is given in (6.16). The increasing Tx coil inductance results in a decrease in the resonant frequency.

$$\omega_{resonant}^2 = \frac{1}{LC} \tag{6.16}$$

This phenomenon is tested experimentally. In Fig. 6.25, experimental measurement of 1Tx and 2Tx operation input to output voltage gain is presented. As expected, the resonant frequency shifts into lower frequencies when a single Tx coil is open-circuited. The mutual inductance between the Tx coils is measured -10 μH. Therefore, the Tx coil inductance increases from 150 μH to 160 μH, which results in a change of resonant frequency from 150 kHz to 145 kHz as also verified in the experimental gain plots.

As given in Fig. 6.25, the quality factor of the system also increases for the faulty mode of operation. Assuming the operation is close to resonance, the reflected impedance is to the Tx side is purely resistive. Considering the magnetic circuit of the system, the power is transferred from two separate Tx modules, which results in twice the

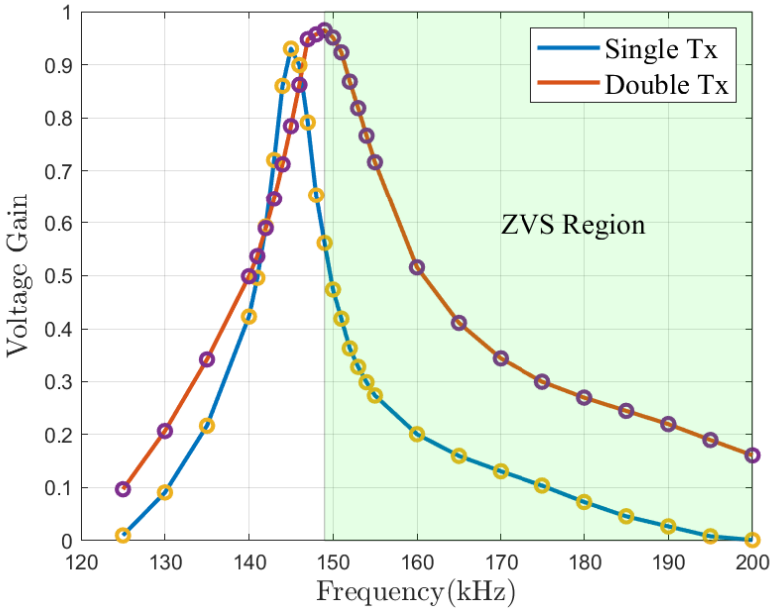


Figure 6.25: Experimental gain plots of double and single Tx operation for $M_{Tx1,Tx2} = -10\mu H$. The ZVS region is given for normal operation(i.e. double Tx operation.)

reflected resistance on each Tx module.

The experimental fault modeling for single Tx open circuit fault was performed at 155 kHz. The voltage gain suddenly drops from 0.75 to 0.28. Experimentally, the output voltage drops from 80 to 30 V_{DC} (see Fig. 6.24) which gives the same output voltage drop ratio as given in Fig. 6.25.

6.7 Summary

In this Chapter, the addition of a middle stage resonator to 2Tx-4Rx system is discussed. Firstly, a design methodology is shared. Using, low quality factor at the Rx side, the design methodology is reduced to a conventional series-series IPT design. The design flowchart is given in Fig. 6.3. The system parameters are chosen such that previous Tx side IPT coils and power modules given in Chapter 4 can be used. During normal operation under rated power transfer a peak efficiency of 90.0% is achieved

as given in Table 6.5. The system is tested for 1Rx open-fault, 2Rx open-fault, 1Tx open-fault, and open/short-circuited load fault conditions. For all conditions, equal Rx side current/power sharing is achieved. While, high fault tolerance is achieved for Tx and Rx side open-circuited fault conditions, open/short-circuited load fault tolerances are found to be dependent on operation frequency.

The proposed system is then mounted on a rotating shaft. To increase the air gap a new set of Tx side IPT coils are designed. While, the air gap is increased, due to higher number of turns the system efficiency decreased to 82%. The system is first tested for 150 rpm where the output voltage and input current oscillations are investigated. Then using mechanical switches and relays, the previously presented fault conditions are experimentally presented for 250 rpm rotation. At 155 kHz operation frequency the system is highly fault tolerant to open-circuited Tx-Rx faults and open-circuited load faults however, since the operation is close to the resonant frequency short-circuited load operation is problematic. Moreover, unlike the initial system, the new set of Tx side IPT coils have negative coupling and hence for open circuited Tx fault condition the quality factor of the overall system increases and the resonant frequency shifts into lower frequencies.

CHAPTER 7

CONCLUSIONS

In this thesis, three different IPT systems are presented, from analytical design to system realization level. The proposed systems aim to replace slip rings and/or brushless exciters used in electrical machines. Due to lack of physical contact, regular maintenance of the system due to friction wear is eliminated. While the switching frequency is chosen in the range of 150-200 kHz, the mechanical rotational speeds are in the range of a few Hz. This results in a much faster response time, and hence the maximum speed is limited by the rated mechanical speed. If the mechanical design is rigid and can withstand high centrifugal forces, the practical operation speed can be increased as desired. Also, to increase the fault tolerance of the overall system, a modular structure is employed. Two different topologies are tested for different fault conditions, and finally, the 2Tx-4Rx with middle stage resonator system is mounted on a rotating shaft where several experimental results are presented.

7.1 2Tx-4Rx IPT System

The first prototype under investigation is 2Tx-4Rx series-series compensated parallel-connected common DC-bus. While the aim is to increase the overall fault tolerance to Rx side open circuit faults and increase the overall reliability of the system, parallel-connected common DC-bus introduced current balancing challenges. In Chapter 1, this problem definition is made where the small differences in the induced EMF due to magnetic-coupling differences resulted in unequal power/current sharing the Rx modules. In Chapter 3, the 2Tx-4Rx system is designed analytically where the derivations include bifurcation free design of 1Tx-2Rx system, which can be extended to multiple

Tx-Rx module configurations. Then, an in-depth analytical derivation is performed for both the addition of cross-coupling between the Rx module and intentional detuning of Rx side resonant frequency. While both methods are investigated separately, a combined effect is also simulated and experimentally verified. For the maximum misalignment condition, a CBR of 83.7% is achieved for the combined effect, which is a 55.8% improvement compared to no cross-coupling and fully-tuned circuit. Moreover, since the system is symmetric, the Tx currents are nearly equal to each other for all rotational positions, as verified experimentally in Fig. 5.5 under normal operation. The efficiency of the system at rated power transfer is 89.6%. The aim was to achieve fault tolerance under a single Rx module open-circuit fault. While the Tx and Rx power converters are below rated values, the current balancing was not achieved due to high misalignment difference at certain rotational positions as given in Fig. 5.10 and Fig. 5.11.

7.2 2Tx-4Rx IPT System With Middle Stage Resonator

Although current balancing is significantly improved for 2Tx-4Rx system, fault tolerance to multiple fault conditions is not achieved. Moreover, during faulty mode operation, the Rx currents are highly unbalanced. To solve this problem, a middle-stage resonator is added. While the Tx coils are coupled with the resonator, they are magnetically isolated from the Rx modules. Series connection of resonator side of HFCI, results in equal induced voltage on each Rx module. In the case of multiple open-circuited Rx faults, again, the induced voltages are the same. The system can also operate under single open-circuited Tx faults. However, due to the increased quality factor of the system, the maximum power transfer is limited by the Tx module current rating. Also, depending on the operation frequency, the system is fault-tolerant to open and short circuit load conditions. For the 2Tx-4Rx system with middle stage resonator, two different systems are built. For the first system, the same Tx side IPT coils are used as given in Chapter 4. The system is first tested at rated power, and efficiency of 90.9% is achieved. The open-circuited Rx module faults decrease the efficiency slightly due to increased core loss on the HFCI and higher conduction loss on the Rx side rectifier diodes. However, a major decrease in efficiency is when a

single Tx module is open-circuited. Due to increased quality factor, higher currents pass through the Tx coil, which results in a higher loss on both MOSFET's and the IPT coil. For this case, efficiency of 81.6% is achieved. Since the resonator coil is separated into two parts, the resonator IPT coil inductance is rather small. Therefore, in order to achieve the required coupling between the Tx-resonator coils, the airgap is significantly reduced (5 mm). The air gap is unfeasible for a rotational system due to mechanical tolerances, and hence a new set of Tx side IPT coils with higher inductances are used. This way, the required magnetic coupling can be achieved. However, the intrinsic resistance of the new Tx side IPT coil set is significantly higher, and hence an 8% decrease in the efficiency is observed. Using the rotational system, efficiency of 82.5% is achieved for an airgap of 10 mm.

While for the first system, the magnetic coupling between the Tx modules is eliminated using ferrite shielding, the rotational system has significantly higher negative cross-coupling between the Tx coils. Therefore, the resonant frequency of the system changes when there is a single Tx module fault. This is beneficial because, during fault transient, the current magnitude in the operational Tx is reduced, whereas in the first system, the Tx current may increase significantly.

7.3 Comparison

Until this point, all different IPT systems are presented. However, an overall system level comparison is still missing. In this section, the 2Tx-4Tx system, resonator system and the rotational system will be compared in terms of a few key features as presented in Table 7.1.

For applications like contactless slip-ring, where the air gap distance is no concern, the rotational resonator system is suitable. With a much robust mechanical design, the inductance of the Tx coils can be reduced, and hence the overall system efficiency can be increased as in the resonator system. With the proposed system design, increased fault tolerance to various fault conditions is achieved. Therefore, the system is highly

Table 7.1: Comparison of the Proposed IPT Systems

	2Tx-4Tx System	**Resonator System**	**Rotational Resonator System**
Resonant frequency	150 kHz	150 kHz	150 kHz
Voltage input	100 V	100 V	100 V
Voltage output	100 V	100 V	100 V
Peak Efficiency	89.6%	90.9%	82.5%
Normal operation current balancing	Within limits	Excellent	Excellent
Faulty operation current balancing	Highly unbalanced	Excellent	Excellent
Air gap	Highest (30 mm)	Lowest(8-10 mm)	Low(10-15 mm)
Single Rx open circuited fault tolerance	Yes	Yes	Yes
Double Rx open circuited fault tolerance	Module location dependent	Yes	Yes
Single Tx open circuited fault tolerance	Yes	Yes, but with reduced power	Yes, but with reduced power
Open circuited load fault tolerance	Frequency dependent	Frequency dependent	Frequency dependent
Short circuited load fault tolerance	Frequency dependent	Frequency dependent	Frequency dependent
Overall fault tolerance	Low	High	High

suitable for applications where reliability is a major issue.

The coil shape in all applications is chosen such that the eddy loss on the shaft is reduced as presented in section 2.2.1. However, modular designs like 2Tx-4Rx system are also highly suitable for wireless EV charging. The coil shapes can be modified such that misalignment tolerance is increased. Moreover, with proper IPT coil design, the air gap can be increased. While the module number is selected as 2Tx-4Rx as in section 2.2.2, to achieve magnetic symmetry, different module combinations can be used.

7.4 Summary of Contribution to Literature and Novelties

In the literature, there are some studies about the design of contactless slip-rings [6, 7, 8, 9]. However, all of these studies use a single Tx and a single Rx structure. Therefore, compared to the modular system design presented in this thesis, the fault tolerances are much lower. In addition, compared to the systems in the literature having the same power rating, the semiconductor ratings are much lower again due to modularity. Moreover, with the proposed middle-stage resonator system, the fault tolerance of the system is significantly increased. While the single Tx-single Rx system is prone to Rx side open-circuit faults, the proposed system is highly tolerant to

such fault conditions.

From an analytical perspective, in this thesis, the bifurcation phenomenon is generalized to n_{Tx} to $2n_{Rx}$ many modules. Also, while the current balancing problem in parallel connected common DC-bus systems are previously mentioned in [30, 56, 57], the effect of cross-coupling between the Rx modules and the combination of this method with the Rx side resonant frequency detuning is presented in this thesis. Moreover, in Chapter 6, the design of IPT systems with middle stage resonators is reduced to conventional series-series compensated IPT design under low Rx side quality factor. Overall the contributions to the literature and novelties can be listed as in Table 7.2.

Table 7.2: Contributions to Literature and Novelties

System Level	**Component Level**	**Analytical Level**
Modularity	Coil geometry reducing Eddy loss on shaft	Generalization of bifurcation phenomenon
Improved fault tolerance	Up-curvature of coil endwindings resulting in Rx cross-coupling	Generalization of series-series compensated IPT system design
Increased reliability	Up-curvature of Tx coil endwindings resulting in much more uniform radial B-field	Effect of Rx side cross-coupling on current balancing
		Effect of Rx side resonant frequency detuning on current balancing
		Reduction of IPT system with resonator design to conventional series-series system design

7.5 Practical Application Considerations

Both the 2Tx-4Rx and 2Tx-4Rx with middle-stage resonator systems are uni-directional, single quadrant DC-DC converters. Therefore, these systems are not suited for systems where field voltage reversal is required. In large generators connected directly to the grid, field voltage reversal is often required to increase the transient response to frequency fluctuations. Moreover, this system can be converted to a bi-directional structure by replacing the receiver side passive diode rectifiers with an active full-

bridge rectifier structure. However, this increases the complexity due to the additional need for receiver-side control. Although this system can operate at any practical rotational speed (limited by mechanical rating), it is not practical to use these systems for constant speed generators since brushless exciters already have significantly improved operational reliability.

Another possible application is the rotary power transfer in robotics. The same design procedure can easily be applied to a wide range of power levels. There are already a few industrial products in the industry for such applications. Compared to the products by the companies PowerbyProxi [58] and TDK Electronics [59] while the efficiencies are somewhat comparable, the reliability of the proposed system is much superior.

7.5.1 Field Current Filtering

In this thesis, two different IPT systems are designed to externally excite the field windings of wound rotor synchronous generators. While significant attention is given to IPT systems with modular structures having improved reliability, a short discussion is still required for industrial applications. In Fig. 6.20, the load is purely resistive, and due to small axial misalignment between the Tx and resonator IPT pick-up coil, there exists a low-frequency oscillation. Since any current oscillation in the field winding will surely induce torque ripples, it is crucial to discuss the extent of this problem. Consider the wound rotor synchronous machine presented in [6]. The important machine parameters are presented in Table 7.3.

Table 7.3: Wound Rotor Synchronous Machine Parameters [6]

Rotor Inductance (L_f)	30 H
Rotor Resistance ($R_f(@20°C)$)	31.4 Ω

Consider the system given in Fig. 7.1. The IPT system can be modeled as a voltage source with a waveform given previously in Fig. 6.20. The field winding can be modeled as series-connected RL circuit whose parameters are given in Table 7.3.

According to the simulation results, the field current has a magnitude of 2.54 A and a ripple of 0.4 mA_{rms} which corresponds to 0.015% in magnitude. Due to the high filtering capability of the field winding, the ripple in the current is negligibly small.

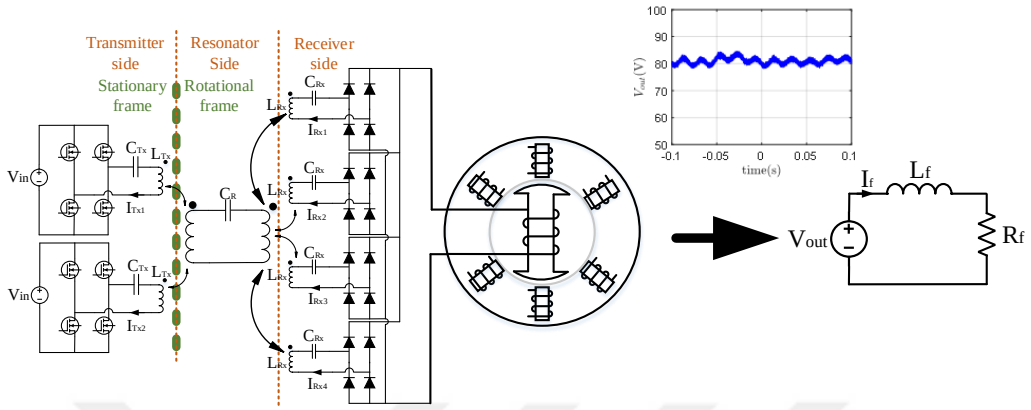


Figure 7.1: 2Tx-4Rx system with middle stage resonator connected to field winding of an wound rotor synchronous generator presented in [6].

7.6 Possible Improvements

With the increased interest in consumer friendly electronics and integration of EV systems to our daily lives, WPT will surely be a trending topic both in the industry and in the literature. Although in this thesis, special attention is given to current/power balancing and fault tolerance, there is still room for improvement on many different subjects.

7.6.1 Analytical Modeling

The design presented in Chapter 6 neglects the Tx-Rx magnetic coupling. In fact, the Tx-Rx magnetic coupling is eliminated in the system design using HFCI that couples the resonator system with the Rx coils. Confining the Rx coil into a much compact space and exterior ferrite shielding due to magnetic core eliminated the Tx-Rx coupling completely. However, a downside of such a system is the reduced inductance of the resonator IPT coil. The required mutual inductance between the Tx and resonator

coil is harder to achieve with large air gaps. This was also the main reason for the replacement of Tx IPT coil set for the rotational system. For the rotational system, the air gap is increased in the cost of increased intrinsic resistance, and hence a lower system efficiency is achieved. Hence, An analytical design model, including the addition of Tx-Rx couplings as in [50, 60, 61] is necessary to increase the air gap and the system efficiency.

7.6.2 Power Electronics Converter Improvements

In Chapter 4, the full-bridge converter design is presented. While special attention was given to minimize the gate loop inductance, no special optimization was performed.

In this thesis, no special attention was given to EMI/EMC compatibility. With proper EMC filter design, the system can be brought to IEC 61000 standards.

The design can further be reduced by using GaN switches where higher operation frequencies and lower conduction losses will result in a much smaller overall system [62]. Due to low semiconductor loss, the system can also be cooled with a smaller heatsink.

The full-bridge converter circuit requires a DC input. However, AC mains rectification using diode rectifiers increases the total harmonic disturbance of the system. Therefore, a power factor corrector(PFC) stage is required at the input. Another solution is to use AC-AC converters such as matrix converters [63, 64] that eliminates the need for a PFC stage. The power factor of the system is highly related to the operation frequency, and the power factor is equal to one if the switching frequency is equal to the resonant frequency. Moreover, the quality factor of the resonant tanks are relatively high, and hence no high-order harmonic will be drawn from the grid.

7.6.3 IPT Coil Intrinsic Quality Factor Improvements

In this thesis, special attention was given to modularity and fault tolerance. Although, for current balancing up-curvature of the end windings of the Rx coils is beneficial, no special finite element analysis was performed to increase the intrinsic quality factor of the coils. In an IPT system, the majority of the losses occur on the IPT coils in the form of heat. Therefore, IPT coils with lower resistance directly increases the overall DC-DC efficiency. Moreover, during ferrite spoke design was done using a few iterations. The overall IPT coil design can be performed with an optimization method.

7.6.4 Mechanical Improvements

The proposed system operates at 150 kHz and for any practical mechanical rotational speed, the electrical time constant is much higher. Therefore, the practical rotational speed limit is directly related to the overall mechanical stability of the system. With a deeper analysis and design of the mechanical structure will result in an increased rated speed. Also during mass production, the small differences in the couplings can be reduced. Therefore, less cross-coupling will be required for the 2Tx-4Rx system. Having less area of the upward curvature increases the intrinsic quality factor of the IPT coils and hence increases the system efficiency.

7.6.5 Closed-Loop Control Improvements

While the closed-loop control was achieved during initial testing, due to the speed of the Bluetooth communication, a control loop speed around 2 kHz was achieved. Moreover, since the data transfer was possible with only 8 bits(1 parity-7 data bit), the sensitivity of the control was not as well as desired. As an improvement, the control can be achieved using a much faster Wi-fi module.

The main benefit of having a higher bandwidth is the increase in the control loop speed. This allows faster response time to fault transients, a decrease in steady-state

time. Moreover, while an ADC of 12 bits was used, it was limited by 8 bits. With higher bandwidth, a much more sensitive output voltage control can be achieved.

Another method is to use a much higher frequency to send the data from the receiver to the transmitter as in [65, 66]. This way, the control loop speed can be increased and transmitted without any communication protocol. However, special modulation techniques should be used, and hence the overall system complexity will surely increase.

7.6.6 Reliability

The addition of middle stage resonator has increased the system reliability significantly. Fault tolerance to multiple open-circuited Rx faults and Tx faults is improved. However, depending on the operation frequency, the system is still prone to open or short circuited load conditions. Therefore, a short circuit protection has to be implemented on the Tx side IPT modules.

7.6.7 Different Topologies

In this thesis, series-series compensation method was used since the resonant frequency is independent of the loading and coupling variations. However, with the proposed coil geometry, the reflected impedance to the Tx modules are constant due to constant resultant coupling. Therefore, series-parallel compensation with parallel connected DC-bus topology can also be implemented. Although, not mentioned in this thesis in detail, higher order compensation methods like LCL-LCL [24] or LCC-LCC [67, 68] has in increased trend in the literature in the recent years. Especially LCC-LCC compensation is often used in wireless EV chargers.

7.6.8 System Sizing

System sizing is often directly related to the operation frequency and hence it is also related to the PCB design and semiconductor selection. If higher frequencies are

selected, the coil sizes and required series capacitors decreases significantly. With a smaller inductance, the IPT sizes can be reduced to smaller areas. Moreover, the DC-link capacitors can also be chosen smaller due to reduced AC current ripple.

REFERENCES

[1] Wikipedia, "Electric Machine." https://en.wikipedia.org/wiki/Electric_machine, 2021. [Online; accessed 16-May-2021].

[2] A. Fitzgerald, A. Fitzgerald, C. Kingsley, and S. Umans, *Electric Machinery*. McGraw-Hill International Edition, McGraw-Hill, 2003.

[3] Y. Chen and B. Zheng, "What happens after the rare earth crisis: A systematic literature review," *Sustainability (Switzerland)*, vol. 11, no. 5, pp. 1–26, 2019.

[4] M. Froese, "Copper or silver? How to choose reliable wind-turbine brushes." https://www.windpowerengineering.com/wp-content/uploads/2018/10/3.-An-example-of-a-brush-holder-BGB.jpg,", 2018. [Online; accessed 16-May-2021].

[5] P. Kjaer, T. Kjellqvist, and C. Delaloye, "Estimation of field current in vector-controlled synchronous machine variable-speed drives employing brushless asynchronous exciters," *IEEE Transactions on Industry Applications*, vol. 41, no. 3, pp. 834–840, 2005.

[6] J. Dai, S. Hagen, D. C. Ludois, and I. P. Brown, "Synchronous generator brushless field excitation and voltage regulation via capacitive coupling through journal bearings," *IEEE Transactions on Industry Applications*, vol. 53, no. 4, pp. 3317–3326, 2017.

[7] K. Song, B. Ma, G. Yang, J. Jiang, R. Wei, H. Zhang, and C. Zhu, "A rotation-lightweight wireless power transfer system for solar wing driving," *IEEE Transactions on Power Electronics*, vol. 34, no. 9, pp. 8816–8830, 2019.

[8] J. Kang, Y. Liu, and L. Sun, "A primary-side control method of wireless power transfer for motor electric excitation," in *2019 14th IEEE Conference on Industrial Electronics and Applications (ICIEA)*, pp. 2423–2428, 2019.

[9] M. Maier and N. Parspour, "Operation of an electrical excited synchronous machine by contactless energy transfer to the rotor," *IEEE Transactions on Industry Applications*, vol. 54, no. 4, pp. 3217–3225, 2018.

[10] "Tesla Historic Inductive Power transfer system." https://www.bibliotecapleyades.net/tesla/esp_tesla_10.htm, 2021. [Online; accessed 16-May-2021].

[11] C. Q. Choi, "Wireless Power Lights Bulb 7 Feet Away." https://www.livescience.com/1588-wireless-power-lights-bulb-7-feet.html, 2007. [Online; accessed 16-May-2021].

[12] D.-J. Kim, "Wireless Charging Electric Bus." https://kmatrix.kaist.ac.kr/wireless-charging-electric-bus, 2015. [Online; accessed 16-May-2021].

[13] SAMSUNG, "Charged Up: The Evolution of Samsung's Wireless Charging Technology." https://news.samsung.com/global/charged-up-the-evolution-of-samsungs-wireless-charging-technology, 2017. [Online; accessed 16-May-2021].

[14] T. News, "Nissan Leaf goes wireless: shows wireless charger in work." https://www.torquenews.com/1/nissan-leaf-going-wireless-2013-shows-how-wireless-charger-works, 2011. [Online; accessed 16-May-2021].

[15] B. Fahimi, P. T. Balsara, D. Patil, J. M. Miller, and M. K. McDonough, "Wireless Power Transfer for Vehicular Applications: Overview and Challenges," *IEEE Transactions on Transportation Electrification*, vol. 4, no. 1, pp. 3–37, 2017.

[16] J. M. Miller, O. C. Onar, and M. Chinthavali, "Primary-side power flow control of wireless power transfer for electric vehicle charging," *IEEE Journal of Emerging and Selected Topics in Power Electronics*, vol. 3, pp. 147–162, mar 2015.

[17] O. C. Onar, S. L. Campbell, L. E. Seiber, C. P. White, and M. Chinthavali, "A high-power wireless charging system development and integration for a Toyota

RAV4 electric vehicle," *2016 IEEE Transportation Electrification Conference and Expo, ITEC 2016*, 2016.

[18] WAVE, "Wireless Advanced Vehicle Electrification: Inductive Charging." https://waveipt.com/. [Online; accessed 16-May-2021].

[19] R. Tavakoli and Z. Pantic, "Analysis, Design, and Demonstration of a 25-kW Dynamic Wireless Charging System for Roadway Electric Vehicles," *IEEE Journal of Emerging and Selected Topics in Power Electronics*, vol. 6, no. 3, pp. 1379–1393, 2018.

[20] "Wireless Power Transfer." https://www.watelectronics.com/wireless-power-transfer, 2021. [Online; accessed 16-May-2021].

[21] Y. H. Sohn, B. H. Choi, E. S. Lee, G. C. Lim, G. H. Cho, and C. T. Rim, "General Unified Analyses of Two-Capacitor Inductive Power Transfer Systems: Equivalence of Current-Source SS and SP Compensations," *IEEE Transactions on Power Electronics*, vol. 30, no. 11, pp. 6030–6045, 2015.

[22] Z. Huang, S. C. Wong, and C. K. Tse, "Comparison of Basic Inductive Power Transfer Systems with Linear Control Achieving Optimized Efficiency," *IEEE Transactions on Power Electronics*, vol. 35, no. 3, pp. 3276–3286, 2020.

[23] S. Li, W. Li, J. Deng, T. D. Nguyen, and C. C. Mi, "A Double-Sided LCC Compensation Network and Its Tuning Method for Wireless Power Transfer," *IEEE Transactions on Vehicular Technology*, vol. 64, no. 6, pp. 2261–2273, 2015.

[24] B. Esteban, M. Sid-Ahmed, and N. C. Kar, "A Comparative Study of Power Supply Architectures in Wireless EV Charging Systems," *IEEE Transactions on Power Electronics*, vol. 30, no. 11, pp. 6408–6422, 2015.

[25] K. Lee and S. H. Chae, "Comparative analysis of frequency-selective wireless power transfer for multiple-rx systems," *IEEE Transactions on Power Electronics*, vol. 35, no. 5, pp. 5122–5131, 2020.

[26] R. Narayanamoorthi, A. V. Juliet, and B. Chokkalingam, "Frequency splitting-based wireless power transfer and simultaneous propulsion generation to multiple micro-robots," *IEEE Sensors Journal*, vol. 18, no. 13, pp. 5566–5575, 2018.

[27] Y.-J. Kim, D. Ha, W. J. Chappell, and P. P. Irazoqui, "Selective wireless power transfer for smart power distribution in a miniature-sized multiple-receiver system," *IEEE Transactions on Industrial Electronics*, vol. 63, no. 3, pp. 1853–1862, 2016.

[28] M. Bojarski, E. Asa, K. Colak, and D. Czarkowski, "Analysis and control of multiphase inductively coupled resonant converter for wireless electric vehicle charger applications," *IEEE Transactions on Transportation Electrification*, vol. 3, no. 2, pp. 312–320, 2017.

[29] J. Pries, V. P. N. Galigekere, O. C. Onar, and G.-J. Su, "A 50-kw three-phase wireless power transfer system using bipolar windings and series resonant networks for rotating magnetic fields," *IEEE Transactions on Power Electronics*, vol. 35, no. 5, pp. 4500–4517, 2020.

[30] G. Ke, Q. Chen, W. Gao, S.-C. Wong, C. K. Tse, and Z. Zhang, "Research on ipt resonant converters with high misalignment tolerance using multicoil receiver set," *IEEE Transactions on Power Electronics*, vol. 35, no. 4, pp. 3697–3712, 2020.

[31] Z. Yan, B. Song, Y. Zhang, K. Zhang, Z. Mao, and Y. Hu, "A Rotation-Free Wireless Power Transfer System with Stable Output Power and Efficiency for Autonomous Underwater Vehicles," *IEEE Transactions on Power Electronics*, vol. 34, pp. 4005–4008, may 2019.

[32] Y. Li, T. Lin, R. Mai, L. Huang, and Z. He, "Compact double-sided decoupled coils-based wpt systems for high-power applications: Analysis, design, and experimental verification," *IEEE Transactions on Transportation Electrification*, vol. 4, no. 1, pp. 64–75, 2018.

[33] S. Cui, Z. Wang, S. Han, C. Zhu, and C. C. Chan, "Analysis and design of multiphase receiver with reduction of output fluctuation for ev dynamic wireless charging system," *IEEE Transactions on Power Electronics*, vol. 34, no. 5, pp. 4112–4124, 2019.

[34] H. Liu, Q. Chen, G. Ke, X. Ren, and S.-C. Wong, "Research of the input-parallel output-series inductive power transfer system," in *2015 IEEE PELS Workshop on Emerging Technologies: Wireless Power (2015 WoW)*, pp. 1–7, 2015.

[35] H. Hao, G. A. Covic, and J. T. Boys, "A parallel topology for inductive power transfer power supplies," *IEEE Transactions on Power Electronics*, vol. 29, no. 3, pp. 1140–1151, 2014.

[36] Y. Li, R. Mai, T. Lin, H. Sun, and Z. He, "A novel wpt system based on dual transmitters and dual receivers for high power applications: Analysis, design and implementation," *Energies*, vol. 10, no. 2, 2017.

[37] R. Bosshard, S. Member, J. W. Kolar, J. Mühlethaler, S. Member, and B. Wunsch, "Power Transfer Coils for Electric Vehicles," *IEEE Journal of Emerging and Selected Topics in Power Electronics*, vol. 3, no. 1, pp. 50–64, 2015.

[38] M. Budhia, J. T. Boys, G. A. Covic, and C. Y. Huang, "Development of a single-sided flux magnetic coupler for electric vehicle IPT charging systems," *IEEE Transactions on Industrial Electronics*, vol. 60, no. 1, pp. 318–328, 2013.

[39] M. Budhia, G. A. Covic, and J. T. Boys, "Design and optimization of circular magnetic structures for lumped inductive power transfer systems," *IEEE Transactions on Power Electronics*, vol. 26, no. 11, pp. 3096–3108, 2011.

[40] A. Zaheer, G. A. Covic, and D. Kacprzak, "A bipolar pad in a 10-kHz 300-W distributed IPT system for AGV applications," *IEEE Transactions on Industrial Electronics*, vol. 61, no. 7, pp. 3288–3301, 2014.

[41] S. Kim, G. A. Covic, and J. T. Boys, "Tripolar pad for inductive power transfer systems for EV charging," *IEEE Transactions on Power Electronics*, vol. 32, no. 7, pp. 5045–5057, 2017.

[42] K. Aditya and S. S. Williamson, "Design guidelines to avoid bifurcation in a series-series compensated inductive power transfer system," *IEEE Transactions on Industrial Electronics*, vol. 66, no. 5, pp. 3973–3982, 2019.

[43] H. Feng, T. Cai, S. Duan, X. Zhang, H. Hu, and J. Niu, "A dual-side-detuned series–series compensated resonant converter for wide charging region in a

wireless power transfer system," *IEEE Transactions on Industrial Electronics*, vol. 65, no. 3, pp. 2177–2188, 2018.

[44] D. Patil, M. K. McDonough, J. M. Miller, B. Fahimi, and P. T. Balsara, "Wireless power transfer for vehicular applications: Overview and challenges," *IEEE Transactions on Transportation Electrification*, vol. 4, pp. 3–37, March 2018.

[45] Y. H. Sohn, B. H. Choi, E. S. Lee, G. C. Lim, G. Cho, and C. T. Rim, "General unified analyses of two-capacitor inductive power transfer systems: Equivalence of current-source ss and sp compensations," *IEEE Transactions on Power Electronics*, vol. 30, no. 11, pp. 6030–6045, 2015.

[46] W. Li, H. Zhao, J. Deng, S. Li, and C. C. Mi, "Comparison study on ss and double-sided lcc compensation topologies for ev/phev wireless chargers," *IEEE Transactions on Vehicular Technology*, vol. 65, no. 6, pp. 4429–4439, 2016.

[47] T. Instruments, "Isolated Gate Driver Turn Off with Negative Voltage." `https://training.ti.com/gate-driver-training-series-isolated-gate-driver-turn-negative-voltage`, 2017. [Online; accessed 16-May-2021].

[48] T. Instruments, "AN-2020 Thermal Design By Insight, Not Hindsight." `https://www.ti.com/lit/an/snva419c/snva419c.pdf?ts=1615474300189`, 2013. [Online; accessed 16-May-2021].

[49] H. Polat, E. Ayaz, O. Altun, and O. Keysan, "Balancing of common dc-bus parallel connected modular inductive power transfer systems," *IEEE Journal of Emerging and Selected Topics in Power Electronics*, pp. 1–1, 2021.

[50] C. K. Lee, W. X. Zhong, and S. Y. R. Hui, "Effects of magnetic coupling of nonadjacent resonators on wireless power domino-resonator systems," *IEEE Transactions on Power Electronics*, vol. 27, no. 4, pp. 1905–1916, 2012.

[51] D. Ahn and S. Hong, "A study on magnetic field repeater in wireless power transfer," *IEEE Transactions on Industrial Electronics*, vol. 60, no. 1, pp. 360–371, 2013.

[52] S. Moon, B. Kim, S. Cho, C. Ahn, and G. Moon, "Analysis and design of a wireless power transfer system with an intermediate coil for high efficiency,"

IEEE Transactions on Industrial Electronics, vol. 61, no. 11, pp. 5861–5870, 2014.

[53] Y. Fang, B. M. H. Pong, and R. S. Y. Hui, "An enhanced multiple harmonics analysis method for wireless power transfer systems," *IEEE Transactions on Power Electronics*, vol. 35, no. 2, pp. 1205–1216, 2020.

[54] X. Qu, Y. Jing, J. Lian, S. Wong, and C. K. Tse, "Design for continuous-current-mode operation of inductive-power-transfer converters with load-independent output," *IET Power Electronics*, vol. 12, no. 10, pp. 2458–2465, 2019.

[55] A. Safaee and K. Woronowicz, "Time-domain analysis of voltage-driven series–series compensated inductive power transfer topology," *IEEE Transactions on Power Electronics*, vol. 32, no. 7, pp. 4981–5003, 2017.

[56] J. P. W. Chow, N. Chen, H. S. H. Chung, and L. L. H. Chan, "An investigation into the use of orthogonal winding in loosely coupled link for improving power transfer efficiency under coil misalignment," *IEEE Transactions on Power Electronics*, vol. 30, no. 10, pp. 5632–5649, 2015.

[57] G. Ke, Q. Chen, W. Gao, S. Wong, C. K. Tse, and Z. Zhang, "Research on ipt resonant converters with high misalignment tolerance using multicoil receiver set," *IEEE Transactions on Power Electronics*, vol. 35, no. 4, pp. 3697–3712, 2020.

[58] PowerbyProxi, "PowerbyProxi achieves FCC compliance for high power industrial wireless connector." `https://www.prnewswire.com/news-releases/powerbyproxi-achieves-fcc-compliance-for-high-power-industrial-wireless-connector-300322661.html`, 2016. [Online; accessed 16-May-2021].

[59] TDK Electronics, "Magnetic Resonance Method of Wireless Power Transfer Technology for Industrial Equipment." `https://product.tdk.com/en/techlibrary/developing/wireless/index.html#contents10`. [Online; accessed 16-May-2021].

[60] J. Zhang, X. Yuan, C. Wang, and Y. He, "Comparative Analysis of Two-Coil and Three-Coil Structures for Wireless Power Transfer," *IEEE Transactions on Power Electronics*, vol. 32, no. 1, pp. 341–352, 2017.

[61] W. Zhong, C. K. Lee, and S. Y. R. Hui, "General analysis on the use of tesla's resonators in domino forms for wireless power transfer," *IEEE Transactions on Industrial Electronics*, vol. 60, no. 1, pp. 261–270, 2013.

[62] A. Q. Cai and L. Siek, "A 2-kw, 95using gallium nitride gate injection transistors," *IEEE Journal of Emerging and Selected Topics in Power Electronics*, vol. 5, no. 1, pp. 458–468, 2017.

[63] N. Xuan Bac, D. M. Vilathgamuwa, and U. K. Madawala, "A sic-based matrix converter topology for inductive power transfer system," *IEEE Transactions on Power Electronics*, vol. 29, no. 8, pp. 4029–4038, 2014.

[64] M. Moghaddami, A. Anzalchi, and A. I. Sarwat, "Single-stage three-phase ac–ac matrix converter for inductive power transfer systems," *IEEE Transactions on Industrial Electronics*, vol. 63, no. 10, pp. 6613–6622, 2016.

[65] Y. Fan, Y. Sun, X. Dai, Z. Zuo, and A. You, "Simultaneous wireless power transfer and full-duplex communication with a single coupling interface," *IEEE Transactions on Power Electronics*, vol. 36, no. 6, pp. 6313–6322, 2021.

[66] X. Li, J. Hu, Y. Li, H. Wang, M. Liu, and P. Deng, "A decoupled power and data-parallel transmission method with four-quadrant misalignment tolerance for wireless power transfer systems," *IEEE Transactions on Power Electronics*, vol. 34, no. 12, pp. 11531–11535, 2019.

[67] W. Li, H. Zhao, S. Li, J. Deng, T. Kan, and C. C. Mi, "Integrated LCC Compensation Topology for Wireless Charger in Electric and Plug-in Electric Vehicles," *IEEE Transactions on Industrial Electronics*, vol. 62, no. 7, pp. 4215–4225, 2015.

[68] X. Qu, H. Chu, S.-C. Wong, and C. K. Tse, "An ipt battery charger with near unity power factor and load-independent constant output combating design constraints of input voltage and transformer parameters," *IEEE Transactions on Power Electronics*, vol. 34, no. 8, pp. 7719–7727, 2019.